# Characterization and Control of a Robot for Wrist Rehabilitation

MASSACHUSETTS INSTITUTE OF TECHNOLOGY
JAN 19 2006
LIBRARIES

by

James R. Celestino

B.S.M.E., Rutgers University (2000)
B.S., Physics, Rutgers University (2000)

Submitted to the Department of Mechanical Engineering
in partial fulfillment of the requirements for the degree of

Master of Science

at the

MASSACHUSETTS INSTITUTE OF TECHNOLOGY

June 2003

© Massachusetts Institute of Technology 2003. All rights reserved.

Author .....
Department of Mechanical Engineering
May 17, 2003

Certified by .....
Neville Hogan
Professor, Mechanical Engineering
Professor, Brain and Cognitive Sciences
Thesis Supervisor

Accepted by .....
Ain A. Sonin
Chairman, Department Committee on Graduate Students

BARKER

# Characterization and Control of a Robot for Wrist Rehabilitation

by

James R. Celestino

Submitted to the Department of Mechanical Engineering
on May 17, 2003, in partial fulfillment of the
requirements for the degree of
Master of Science

## Abstract

Human motor control pathologies, such as those caused by stroke, can be treated through physical rehabilitation. The use of robots in therapy environments seems appropriate considering the possibilities they offer for quantification of performance as well as "quality control" between therapy sessions. The research presented in this thesis is part of the continuing development of robotic applications for physical therapy and neuro-rehabilitation at the Newman Laboratory for Biomechanics and Human Rehabilitation. MIT-MANUS, a robot for shoulder and elbow therapy developed in this lab, introduced this new brand of therapy, offering a highly backdrivable mechanism with a soft and stable feel for the user. The focus here is the development, characterization, and implementation of a robot for wrist rehabilitation, designed to provide three rotational degrees of freedom. The wrist motions of flexion/extension and abduction/adduction are governed by a differential gear mechanism, while pronation and supination of the forearm are actuated by a curved slider attached to the rest of the mechanism. Through the characterization, the device was found to exhibit some unwanted behavior, largely attributable to the nonlinearities inherent in the system. Efforts to suppress these effects through control are presented along with recommendations for addressing these problems at the design level. The alpha prototype has been set up for clinical trials by providing a functional control scheme along with "video game" patient interfaces; initial clinical trials will run in parallel with the development of the next version of the device. If improvements comparable to those seen with the use of MIT-MANUS are seen with the wrist robot, then rehabilitation therapists will have a new and useful tool at their disposal.

Thesis Supervisor: Neville Hogan
Title: Professor, Mechanical Engineering
Professor, Brain and Cognitive Sciences

# Acknowledgments

I could write dozens of nice things about dozens of people I've met during the time I've been here at MIT. To truly give everyone their due, I'd have to add another appendix to this thesis. Considering the extra research that would require and the fact that no one is ever going to read this, it just doesn't seem like it's worth it. Still, I think I can ramble for a few paragraphs ...

Professor Neville Hogan's grasp on the fundamentals of engineering and science and his ability to apply this knowledge quickly to a given situation is both impressive and inspiring. I'd like to think I've learned a lot here by observing his approach to problem solving. As my advisor, he has shown a great deal more patience with me than I deserve. Dr. Hermano Igo Krebs has always offered his suggestions and advice on anything I was working on.

Those people who have had to put up with me on a daily basis deserve special mention. They have enhanced my residence in the lab as I have been able to learn with them and from them and, regardless of what they may think of me, I consider them good friends. Whenever it would have been easier to give up, Jerry Palazzolo has always been there to tell me to shut the heck up and get back to work. Listening to Steve Buerger rant is often so funny that it's hard to tell if he's actually mad about something. Brandon Rohrer's keen analytical mind is augmented by his unique ability to put a positive spin on anything. Phil "I'm-not-an-engineer-but-I-play-one-on-TV" Tang and I have helped each other hone our troubleshooting skills [52], mostly because we've had so much trouble to shoot along the way. The rest of our research group: Belle, Sue, Laura, and, from last semester's lab population explosion, Mike, Chan, Miranda, Tom, Doug, and Jason, have all done their part in making the lab a bustling center of activity or something. Of course, I should also mention the lab alumni who helped ease my transition into graduate school: Kris and, especially, Dustin, for designing the wrist robot, giving me something to work on.

Working in Professor Hogan's research group and in the larger environment of the Newman Laboratory has been a rewarding experience. I am truly honored and humbled to be counted among this lab's ranks and cannot overstate how highly I regard those who work here. Thanks to everyone who has ever helped me solve some technical problem, lent me some equipment, passed on a hockey tip, or just brightened a day with a friendly word. I suppose I could list them all, but instead, I'll just thank the members of the Cinderella story that has been the Newman Lab Softball team. Any group that accepts me as their captain deserves some credit. Couple that with an impressive worst-to-first campaign last summer and you've got yourself the makings of a made-for-TV movie, or, at the very least, a MasterCard commercial: T-Shirts: $12, League entry fee: $120, dominating the MITCSS KF3 league: priceless...

I'd also like to thank all of the faculty and staff who make MIT work 24 hours a day, 7 days a week. Fred Cote of the Edgerton Machine Shop saved my life an average

of 1.34 times per week; without his help, the wrist robot would almost definitely be an expensive paperweight. Leslie Regan has also been a great resource for the entire department. Lori Humphrey, the first person I met upon arriving at MIT, was extremely helpful in getting me acclimated to the environment. I am grateful for the administrative support our lab has received over the past few years from Lori, Tatiana Koleva, Ilea Mathis, and Julie Bentley. Similar thanks go to those at my home away from my home away from my home away from home: Burke. I'd also like to thank the makers of the Dremel rotary tool; they say it has 1,001 uses, but I think they're just being modest.

Boston may not be the friendliest place in the world for a Yankee fan, but I've managed to stay out of trouble, meeting many people through the Tech Catholic Community, Tang Hall, IM softball, and the MIT orchestra and chamber music groups I've been in. I would like to thank Andy Stein, for one, though I remain unimpressed by his ability to bleed Red Sox red. It has been encouraging to meet so many people in my daily travels who are actively working towards a better tomorrow. My sincerest thanks go to them and to anyone who makes it a point to make the world a better, friendlier place. As in the prayer of St. Francis, I hope that I too may be "an instrument of the Lord's peace," and in some small way help those around me.

There are also plenty of people to thank in my hometown of Lakewood and across the rest of the great Garden State. Thanks to Professor Mavroidis, Chuck Pfeiffer, and everyone at the Robotics and Mechatronics Lab at Rutgers University. My four years at Rutgers seems like a blur now, but some things are harder to forget, especially Arek, Steve, Jey, Debjeet, Dave, and their stupid quote board. It's hard to believe that I roomed with Jey Won for over 6 years. I'm not sure if he followed me from Rutgers to MIT, or if I followed him; that's really a matter for the courts to decide. In any case, I'm glad it turned out that way and I wish him the best of luck out on the left coast.

Last but probably most of all, I'd like to thank my family. In many ways, one is defined by his family, and I am fortunate to be a part of a large and supportive one. So, I send my thanks to Grandma, my aunts, uncles, and cousins, all of whom I see too little of. My immediate family, Jessica, Matthew, and Michael, are more important to me than they realize, as are my brother-in-law Luigi and my newborn nephew Alexander. I would also like to thank my parents, as everything I have I owe to them. Mom and Dad routinely turn a blind eye to my faults and praise me for the most insignificant of accomplishments. I hope that I can some day live up to the standards they have set for me.

This research was funded in part by the National Science Foundation, the number 23, and viewers like you.

# Contents

# List of Figures

# List of Tables

# Chapter 1

# Introduction

Robots and automated machinery have found a number of uses in today's society. In general, industrial robots are designed to be stiff with respect to their environments, since an important measure of their performance is their ability to track a prescribed trajectory. Part of the research at the Newman Laboratory for Biomechanics and Human Rehabilitation has been to introduce robotic technology that interacts with human beings, mainly by designing and developing robots for physical therapy applications. Such robots should exhibit a softer feel, not only for safety, but because the emphasis is no longer on trajectory control; ideally, these robotic therapists would act as pure, controllable, effort sources, so that the targeted limb could be pushed around in response to its motion. The introduction of robots into the field of physical therapy opens the door to many research questions. The mere fact that data gathered from robots can be so repeatable promises orders of magnitude of improvement over the current methods of data collection in human motor control. Insights into human motor control, human learning, and the ability to provide customizable, adaptive, yet rigorously quantified therapy are all among the potential benefits. Reaching these goals depends on the design and development of appropriate hardware.

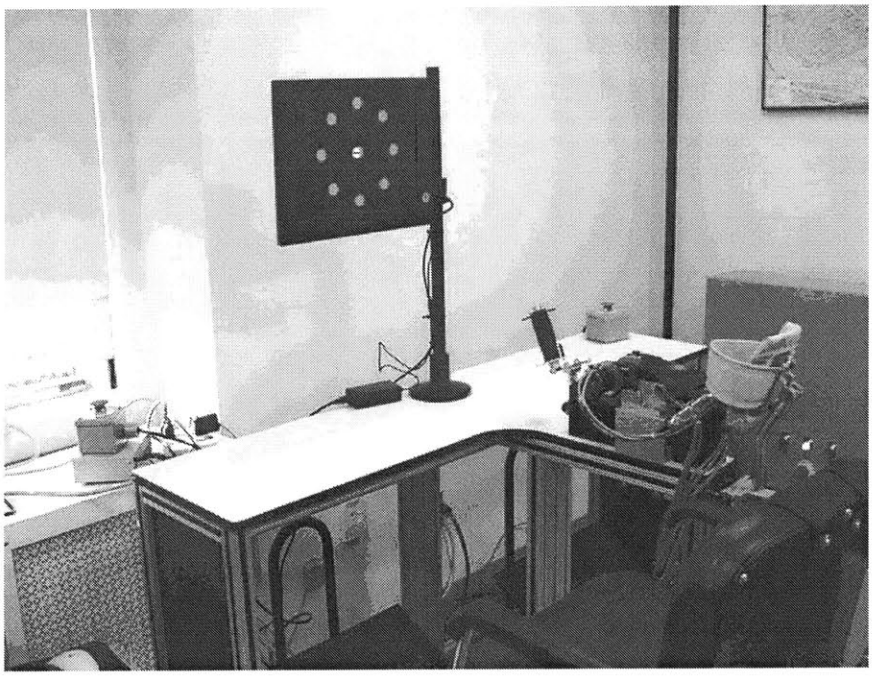

Figure 1-1: Photograph of the wrist robot, currently installed at the Burke Rehabilitation Hospital.

## 1.1 Objectives

The research presented in this document traces the continuing development of a robot designed for wrist rehabilitation, shown in Fig. 1-1. The overriding theme is to create a usable clinical device using the conceptual and detailed design provided in Ref. [54] as a foundation. This is accomplished by addressing the following goals:

- Assemble the wrist robot as described in the original design [54], modifying it as needed to ensure functionality.
- Analyze the design to determine the areas of focus for redesign.
- Properly identify the mechanisms involved in the operation of robot.
- Create a model of the system competent enough to predict experimentally determined behavior.
- Design a controller for the system capable of ensuring smooth, stable operation.

- Characterize the corresponding performance limits of the device.
- Create video games to be used by the robot for therapy.
- Lay out the areas that should be addressed in the future development of this project.

## 1.2 Motivation

Each year, about 700,000 Americans become victims of stroke [58] making it the third largest cause of death and the leading cause of disability in the country. The risk of stroke increases geometrically with age, so that an increase in the incidence of stroke among the population can be expected as the average lifespan increases. Depending on the severity of the stroke, survivors may lose their pre-stroke levels in abilities that rely on cognition and motor control. Research has shown that the brain's plasticity leaves open the possibility for motor recovery [10]. Plasticity refers to the brain's ability to reorganize itself, which can be stimulated through physical therapy. This physical therapy generally involves one-on-one attention from a therapist who assists and encourages the patient through a number of repetitive exercises. The repetitive nature of therapy makes it amenable to administration by properly designed robots. A robotic therapist can eliminate unnecessary exertion by the therapist, quantitatively monitor and adapt to patient progress, and ensure consistency in planning and executing a therapy program.

## 1.3 MIT MANUS

MIT-MANUS, shown in Fig. 1-2, is a planar, two degree of freedom robot providing exercise for the upper extremity as the patient completes a series of "video games" that involve positioning the robot end effector. The design of this robot, completed in 1991, is based on a five-bar, parallel drive Selective Compliance Assembly Robot Arm (SCARA). By minimizing the endpoint impedance of the robot and using impedance

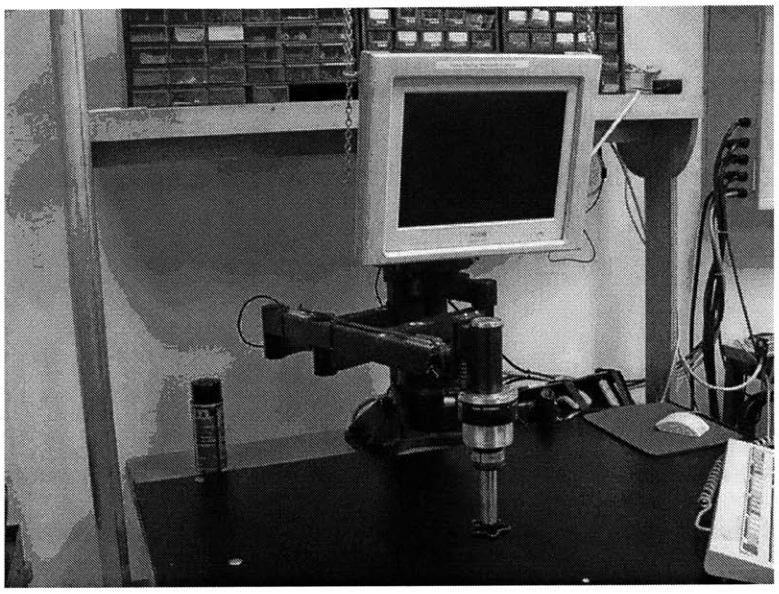

Figure 1-2: Photograph of MIT-MANUS I, currently in service at the Burke Rehabilitation Hospital.

control, it is able to interact with the patient safely and without excessively interfering with the patient's natural arm dynamics. The controller sets up a virtual spring and damper between the task-defined, time-dependent equilibrium point and the position of the end effector. Clinical trials involving MANUS and MANUS-II [56], the alpha and beta prototypes installed at two different rehabilitation hospitals, have shown that robot therapy has great potential. Even as more extensive studies are currently underway to provide additional insight into the usefulness of robot therapy, the success of MANUS has led to the design of more robots to allow for more functionally relevant therapy.

Task related training has proven to be an effective method of therapy in stroke rehabilitation. Improvements due to physical rehabilitation are localized to the targeted area so that, in order for a patient to relearn a given task, that task must be rehabilitated. In order to extend the impact of the robotic therapy techniques developed for MIT-MANUS, new modules targeting other limbs are in development. Designed as a three-dimensional extension to MANUS, the vertical module is currently installed at Burke as a stand-alone robot. Figures 1-3 show this robot before and after packaging,

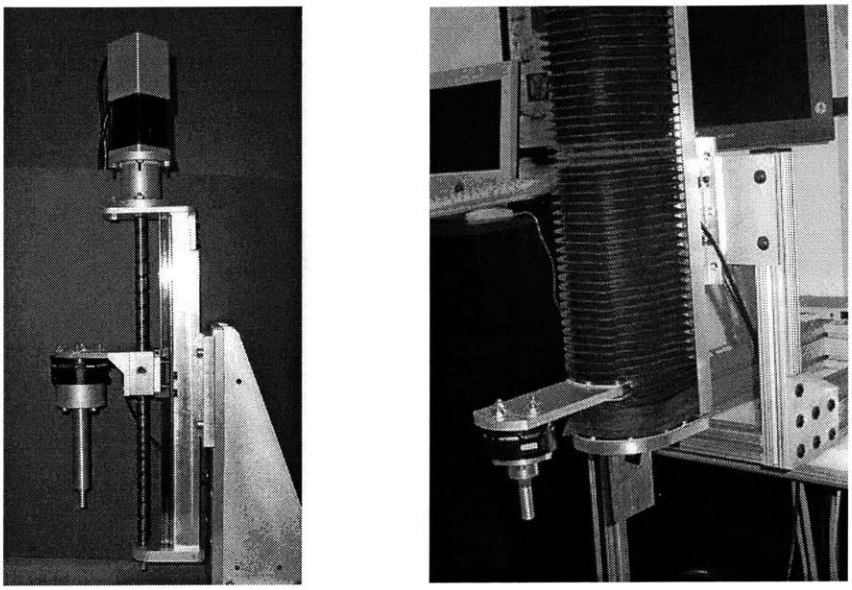

(a) Prototype ball-screw design.

(b) Covered with bellows.

Figure 1-3: A vertical extension for MANUS, currently installed at the Burke Rehabilitation Hospital.

with Fig. 1-3(a) revealing the ball-screw actuated design [8]. Projects in earlier stages of development include those for the fingers and for gait training. Stroke survivors commonly present with reduced fine motor control in their hand; intricate control over the action of the digits allows man to interact with his environment. Once completed, the finger robot will address this issue within the paradigm of providing low mechanical impedance hardware for therapy delivery [52]. Other stroke-induced impairments can directly and indirectly (through voluntary compensatory motions) affect an individual's ability to walk. Though often taken for granted, the ability to walk represents a certain level of independence for a person. The gait training robot will consist of a number of modules, eventually allowing for independent and cooperative assistance of those functions that are critical to human ambulation: weight shift and support, forward progression, ankle mobility, and foot placement.

The research presented here focuses on the effort to develop a robot for wrist rehabilitation. The mobility of the wrist and forearm enhances the value of finger articulations by allowing the hand to take up a wide variety of orientations with

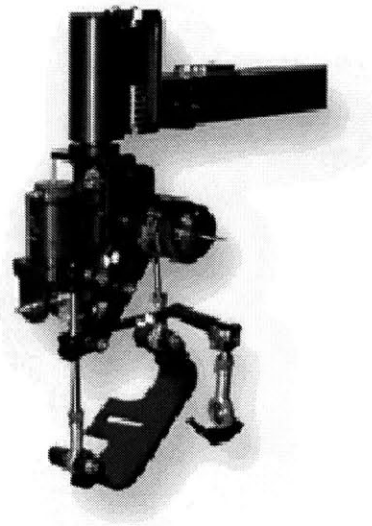

Figure 1-4: Photograph of MIT-MANUS I version of wrist design.

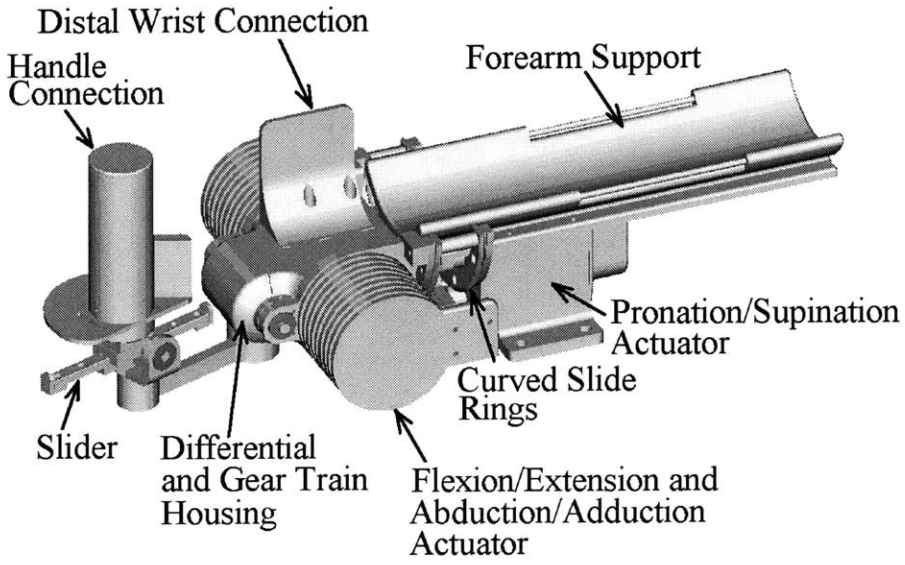


Figure 1-5: CAD solid model representation of the wrist robot [54].

respect to the upper arm. The original design for MIT-MANUS included an actuated handle attachment, shown in Fig. 1-4 to provide for wrist therapy. This design did not find its niche in practice, largely due to difficulties with patient access. Figure 1-5 shows the true starting point for this research, a CAD solid model of the wrist robot as designed by Williams [54]. The robot provides three actuated degrees of freedom: one for forearm articulation and two for wrist rotations. The design will be introduced in more detail in Chapter 3.

## 1.4 Outline of Chapters

The remainder of this thesis follows through on the aforementioned objectives as follows:

**Chapter 2:** This chapter elaborates on the motivation behind this work, providing information on the relevant biology and therapy practices.

**Chapter 3:** Important details from the design of the device are presented here. The steps taken to render the robot functional are also discussed. Finally, details relating to the overall system operation are presented.

**Chapter 4:** In this chapter, the characterization of the individual components used in the robot is discussed.

**Chapter 5:** Model reticulation and system identification for the assembled robot are found here.

**Chapter 6:** The investigation of the stability and control of the device are covered in this chapter.

**Chapter 7:** This chapter offers the context in which the robot will be used.

**Chapter 8:** The final chapter ties together the major conclusions, elaborates on the state of the project, and discusses the avenues of research with this device that have yet to be explored.

# Chapter 2

# Background

Before delving into the details of the design, it is useful to discuss some of the underlying biology. This information has not only helped direct the design of the robot, but has also clarified its purpose. This chapter is not meant to be an extensive study of these topics, but is merely meant to introduce them to the point of usefulness.

## 2.1 Anatomy and Anthropometry

The wrist robot targets three degrees of freedom: two degrees of wrist articulation and one degree of forearm rotation. This section reviews these motions, their basic mechanisms, and some of the anthropometric data characterizing them. Detailed presentation of the relevant dimensions and strength of the hand and wrist have been omitted in this discussion as they have been covered by Williams [54] during the design phase of this project. Parameters that are not discussed in this chapter but are relevant to the remainder of the thesis are summarized in Table 2.1. These parameters, tempered by knowledge of patient variability, especially due to edema or hypertonicity, provide guidelines for the mechanical design.

| | |
|---|---|
| Wrist Breadth | 2.7 in |
| Wrist Thickness | 1.7 in |
| Distal Wrist Crease to Handle Center | 3.0 in |
| Rotational Inertia about Flexion/Extension Axis | 10.2 lb·in$^2$ |
| Rotational Inertia about Abduction/Adduction | 14.4 lb·in$^2$ |
| Rotational Inertia About Pronation/Supination | 5.9 lb·in$^2$ |
| Hand Volar Flexion Strength | 1100 oz·in |
| Hand Dorsal Extension Strength | 1500 oz·in |
| Handle Pronation Strength | 2000 oz·in |
| Handle Supination Strength | 1700 oz·in |

Table 2.1: Summary of key anthropometric data for the male 50$^{th}$ percentile [54].

### 2.1.1 Wrist Articulation

The biomechanics of the wrist joint are more complex than the resulting motion of the wrist would suggest. The wrist motions of interest are depicted in Fig. 2-1 [31]. Rotations about axis **AA'** are described as flexion (arrow 1) and extension (arrow 2). Rotations about **BB'** are known as adduction (arrow 3) and abduction (arrow 4). The term adduction can be used interchangeably with the term ulnar deviation, as it describes wrist motions moving toward the ulna; similarly, abduction is also termed radial deviation. Figure 2-2 shows that a human is generally capable of 15 ° of active abduction and 30 ° of active adduction when ignoring finger adduction. Figure 2-3 shows the active range of motion of the wrist in flexion and extension both to be 85 °.

The overall motion of the wrist is a summation of the interactions of the individual carpal bones both amongst themselves and with the adjacent bones of the forearm and hand. The eight carpal bones of interest are generally divided into a proximal and distal row. Figure 2-4 shows the layout of the carpals and tendons of the wrist. The shape of each carpal bone defines its kinematic relationship to each neighboring bone, thereby contributing to the overall wrist mechanism [2]. Subtleties notwithstanding, it is appropriate to think of the wrist as a Cardan joint within the context of the two gross motion patterns discussed above, at least in a limited sense. Due to the nature of the articular complex, however, it is important to note that the motions

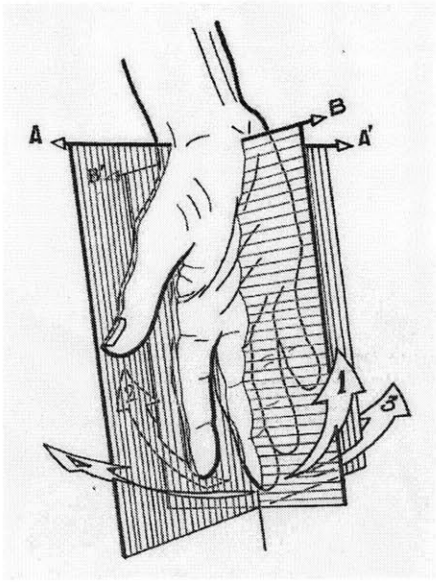


Figure 2-1: Drawing showing the axes of wrist rotation [31].

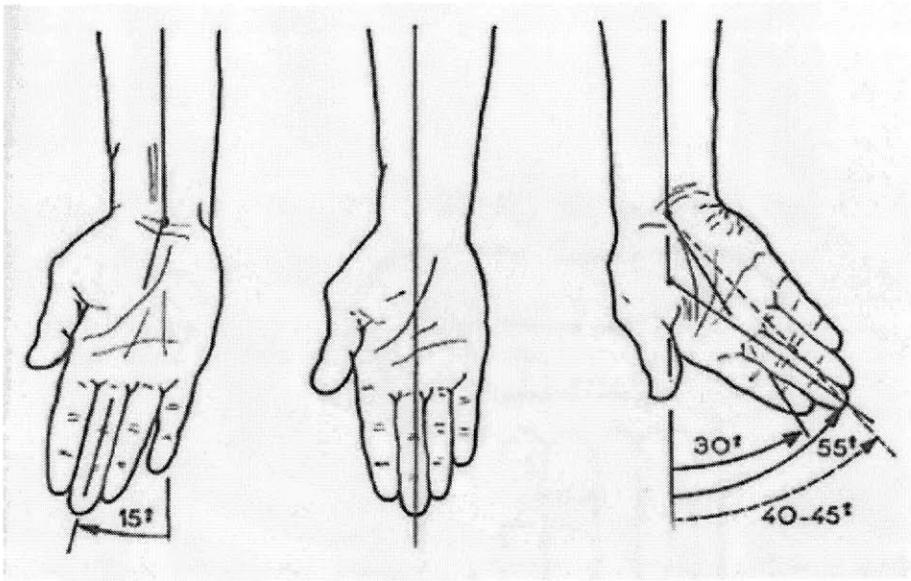


Figure 2-2: Drawings from left to right: available range of motion in wrist abduction (radial deviation), a neutral position, available range of motion in wrist adduction (ulnar deviation) [31].

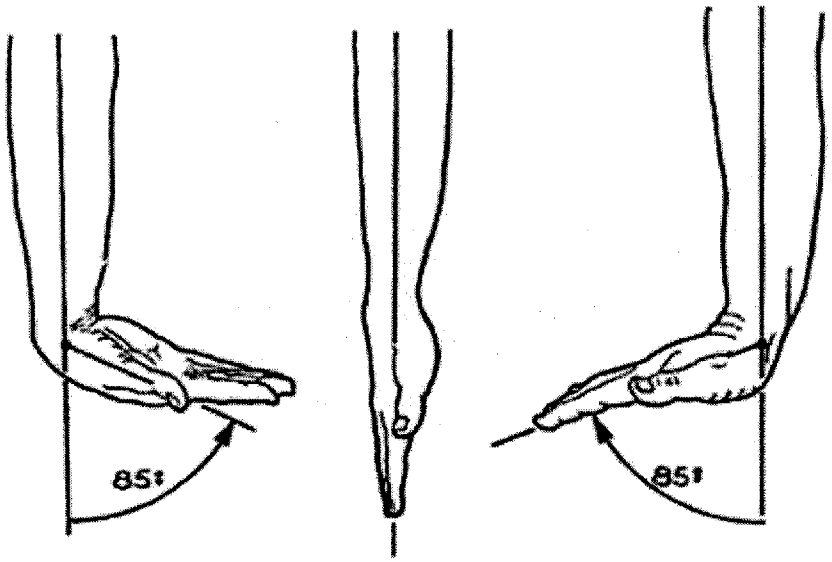


Figure 2-3: Drawings from left to right: available range of motion in wrist flexion, a neutral position, available range of motion in wrist extension [31].

of the wrist joint are coupled. The range of radial and ulnar deviation is minimal when the wrist is fully extended or flexed because of the tension developed in the carpal ligaments [31]. The degree of forearm articulation, the subject of the next section, also plays a role as the achievable ranges of flexion and extension are reduced when the wrist is pronated and abduction is greater in supination than in pronation. This idea is further exemplified in Figure 2-5, which shows the so-called "cone of circumduction." Movements of circumduction refer to the combination of movements of flexion, extension, adduction, and abduction. The coupling between the wrist rotations defines the shape of the cone.

### 2.1.2 Forearm Articulation

The third type of motion addressed by the wrist robot is the rotation of the forearm about its longitudinal axis, known as pronation and supination. Pronation refers to rotating the forearm in the direction that causes the palm to face down while supination refers to the opposite rotation, causing the palm to face up. This rotation is easiest to observe when the elbow is flexed, thus eliminating any confusion with

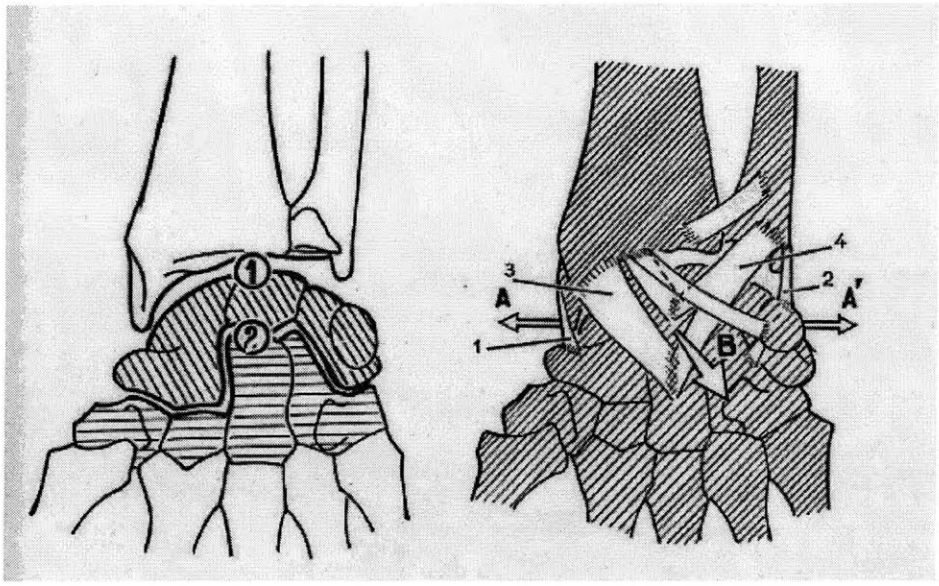


Figure 2-4: Drawings depicting the bone and ligament structure of the articular complex of the wrist [31].

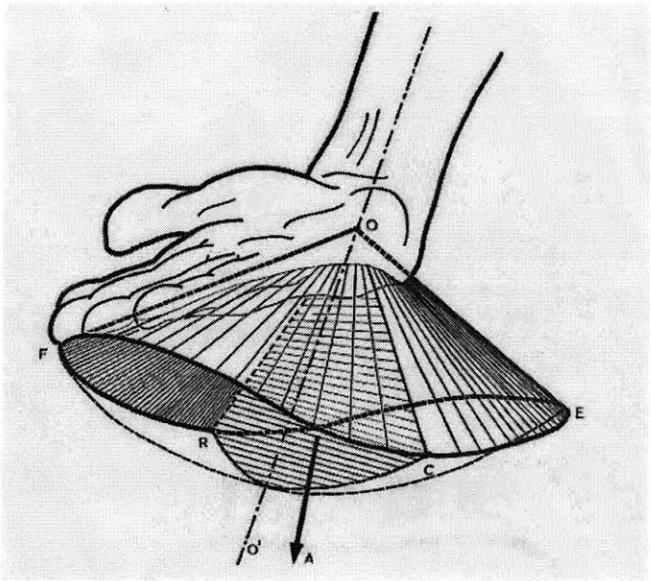


Figure 2-5: Drawing depicting the "cone of circumduction," the envelope of the locus of orientations the axis of the hand can make during normal wrist movements [31].

shoulder rotation. Figure 2-6 shows that the position of neutral rotation occurs when the open palm lies in the plane formed by the shoulder and elbow. In other words, the relationship between a lab frame and a frame of reference describing this rotation is determined by the degree of shoulder abduction. This fact becomes important when considering patient placement at the device. Figure 2-6 also shows that the effective range of motion in pronation and supination is nearly 180°.

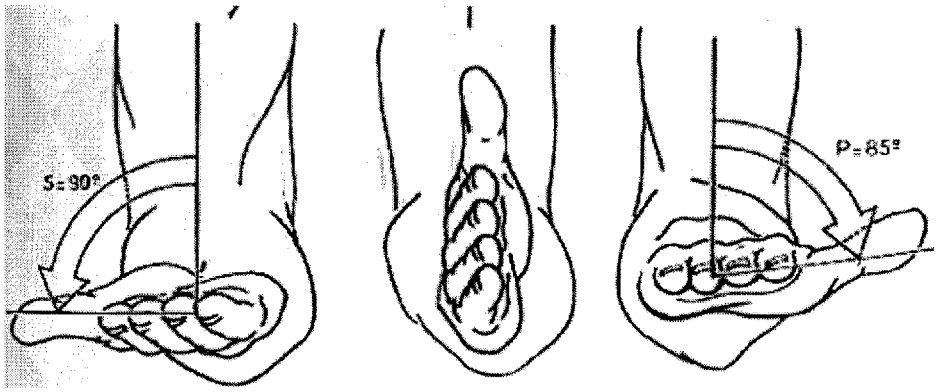


Figure 2-6: Forearm articulation. The center drawing represents the neutral position [31].

Forearm rotation is a result of the two long bones of the arm, the radius and the ulna, rotating over each other. Figure 2-7 shows that the axis for this motion is not constant throughout the range. In supination, the two long bones are parallel to each other. In pronation, however, the radius and ulna are crossed and the axis of rotation is no longer parallel to the radius of the ulna. For the purpose of the design presented here, the main interest is when the forearm lies on the table throughout the motion, *i.e.*, the ulna remains stationary and the radius rotates about it. For this situation, it is appropriate to approximate the location of the axis of rotation through the medial edge of the ulna [31] as shown in Fig. 2-8.

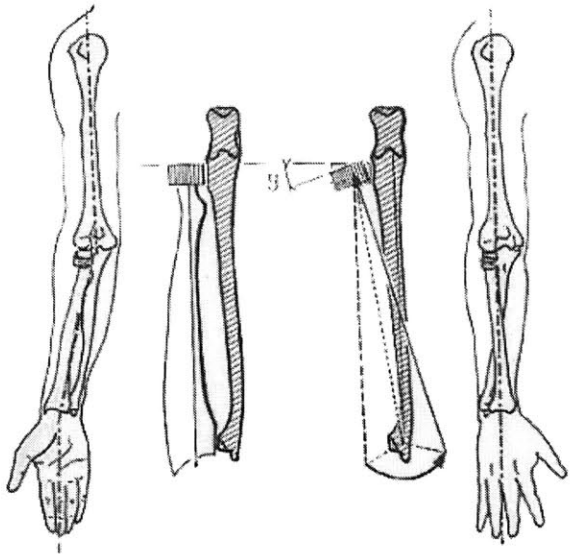

Figure 2-7: Schematic of forearm articulation locating the axis of rotation. The set of drawings on the left represent supination, while the two drawings to the right represent pronation [31].

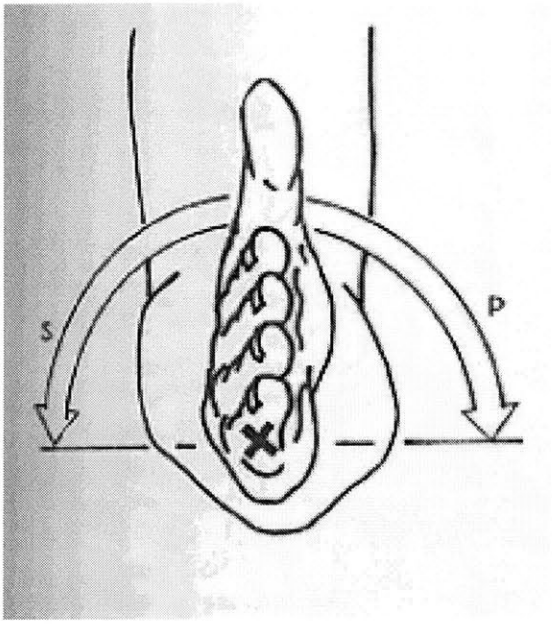


Figure 2-8: Front view of forearm articulation when the forearm is resting on a table throughout the rotation. Note that the axis of rotation is situated slightly above the table, coinciding with the medial edge of the ulna [31].

## 2.2 Perception

Combining information about the capabilities of the normal human wrist with how humans internally perceive actions on their limbs provides a useful backdrop for determining functional requirements. Sensors in the receptor system encode important information about sensation that is integrated at higher levels in the central nervous system. These sensors tend to be very specialized to cover the many quantities humans are able to sense. They can be loosely categorized as exteroceptors, which are responsible for conscious sensation, and proprioceptors, which are not responsible for conscious sensation [36]. Cutaneous reception and visual feedback are examples of important conscious sensations during motor control. Proprioception, namely the combination of limb-position sense and limb movement (kinesthesia) [29], is composed of signals from muscle spindle receptors, Golgi tendon organs, and receptors in the joint capsule [29]. A useful analogy found in Ref. [36] likens the muscle spindle receptors to strain gauges and the Golgi tendon organ to a force transducer.

Human perception is not a direct record of the environment, but rather a function of how the nervous system interprets the sensory information it receives. The goal in the field of psychophysics is to correlate the quantitative aspects of physical stimuli gathered by these sensors with the sensations they evoke [29]. Experimentation has yielded information on this interplay between cognition and sensation. The determination of the just noticeable difference (JND) is akin to the determination the resolution of the human system. This "resolution" must be taken in context, however, as the JND is generally found to be proportional to some reference level (Weber's Law). Table 2.2 summarizes the JNDs associated with wrist activity [51].

## 2.3 Human Motor Control

Between the decision to make a given movement and the execution of that movement by the body lies a complicated feedback control system. The basic unit of the nervous system is the neuron; afferent neurons convey information from tissues and organs

| Activity | JND |
|---|---|
| Wrist and Forearm Rotations | 2° |
| Velocity | 10% of the reference |
| Acceleration | 20% of the reference |
| Force | 7% of the reference |

Table 2.2: Haptic data showing the just noticeable difference (JND) for various activities associated with the wrist [51].

into the central nervous system (CNS), efferent neurons transmit signals from the CNS out to the effector cells (muscles and glands), and interneurons serve as connections between afferent and/or efferent neurons within the CNS. There are roughly 10 efferent and 20,000 interneurons for every afferent neuron [55], indicative of the fact that even the simplest sensation can give rise to multiple neural and, consequently, physical events. Current understanding offers a hierarchical picture of human motor control with five major subdivisions: the cerebral cortex, the basal ganglia, the cerebellum, portions of the brain stem, and the spinal cord. Each subdivision plays a role as processed information from the cerebral cortex, collected from the entire motor apparatus, is refined and modified for execution. All sensory stimulation must first be transformed into neural events, or, action potentials. Force is generated in the muscle when the electrical signal from the efferent neuron activates a series of contractile proteins in the muscle fiber that make up the muscle. The muscles are the actuators for the skeletal system, whose geometry defines the transmission of these forces. Neural circuits in spinal cord provide for reciprocal innervation of agonist and antagonist muscles, which can contribute to the stability of movements or modulate the limb impedance, among other things. Coordinated movement is characterized by appropriate timing and sequence of muscle activation which is, in large part, a learned capability, consisting of both feedback and feed-forward mechanisms [29].

While much of the circuitry necessary for movement is contained within the spinal cord, the organization of these movements apparently takes place at higher levels in the brain. One approach to gaining knowledge about motor control has been to make inferences from the observation and measurement of selected movements. Such

information can be useful in determining control schemes and desired trajectories for an interactive robot. Through dynamic optimization of data from point-to-point movements by primates, it has been shown that such movements are organized so that the trajectory in Cartesian space is smooth, *i.e.*, they follow a minimum-jerk trajectory [25]. A competing theory expounded by Uno [6] holds that movements are organized so as to minimize the integral of time derivative of joint torque, offering a dynamic rather than kinematic view of motor control.

## 2.4 Stroke

Also known as cerebrovascular accidents (CVAs), strokes are generally caused by a blockage in the arteries supplying the brain (ischemia) or by bleeding from burst blood vessels within the brain (hemorrhage), each of which interrupt the blood supply to the brain. Blood transports oxygen and nutrients to the brain while transporting carbon dioxide and other waste products from it. Three major vascular trees supply the arterial blood flow into brain: the right and left internal carotid arteries and the vertebral-basilar system. Any interruption in the flow of blood to and from the brain jeopardizes the survival of the affected tissue and its associated functions. Ischemic stroke, the most common type of stroke, is generally caused by a narrowing of the arteries of the head and neck, in turn commonly caused by atherosclerosis. Blood clots can form on the roughened arteriosclerotic blood vessel wall (thrombosis), or clots can form elsewhere, usually in heart, and break off and lodge at a distant site, occluding circulation at that point (embolus) [14]. The cells deprived of blood for too long will die (necrosis), leaving what is known as an infarction. Cerebral hemorrhages, much less common as a cause of stroke, involve the bursting of blood vessels in the brain either within the brain or at the surface in subarachnoid space. As the brain fills with blood, healthy brain cells are displaced and pressurized, resulting in lesions. The damage to the neurons and pathways in the central nervous system caused by a CVA can cause two types of impaired motor control to appear immediately, namely a loss of volitional movement on the affected side (hemiparesis) and inappropriately timed

or graded muscle activations. With time, other impairments will appear including hyperactive stretch reflexes, increased resistance to passive movement due to changes in the mechanical properties of muscle (spasticity), and hypo-extensibility of the muscle-tendon complex (contracture).

Spasticity is a relatively poorly defined term that has been used to refer to hyperactive stretch reflexes, increased resistance to passive movement, prominence of primitive synergies, and excessive co-contraction of antagonist muscles, among other things [14]. In each definition, the resulting impairment can be likened to some sort of hypertonicity. Functionally, spasticity can be viewed as an asset; spasticity can provide support for otherwise uncontrollable motions. In this sense, spasticity and abnormal reflexes can be viewed as safety features against more disabling impairments such as muscle weakness and loss of coordinated movement. Another pathological consequence of stroke is contracture, which is often a result of neglect of an affected joint. When a joint is neglected, its controlling muscles will atrophy and the collagen and other connective tissue will reorganize, even ossify, across the joint. While the difficulties associated with contracture can be similar to those associated with spasticity, muscle activity is not a factor in contracture; contracture may be a consequence of a neural injury, but it does not constitute a neural deficit. Finally, in discussing the various pathologies stemming from stroke, it is important to mention the cognitive and perceptual consequences. Sensation and perception, along with their importance in the motor control feedback loop, have already been discussed. Loss of proprioception may prompt disuse of a given muscle despite an otherwise intact efferent pathway. Since the effects of a stroke are so highly dependant on the specific nature of the injury, including the size and location of the resulting lesion, the prescribed therapy is highly individualized.

## 2.5 Human Motor Recovery

### 2.5.1 Brain Plasticity

The human brain is capable of extraordinary self-reorganization, making the actions of learning and remembering possible. This ability to dynamically modify neural pathways is known as plasticity. While the brain is hierarchical in nature, its parallel, possibly redundant, neural pathways may allow for this plasticity. Brain injury incurred early in life can be accommodated for, as alternate regions of the brain can be recruited to perform functions normally performed by the injured section. Later in life, the brain is considered less plastic; brain trauma at these stages results in less favorable prognoses for recovery. This could be the result of the brain attempting a reorganization within a more mature structure whose connections are not so easily reintegrated. In any case, there is a strong motivation to look for analogies between the processes of motor learning and motor recovery, offering a reason to expect that therapy would be useful. There is some poorly understood period of spontaneous recovery, usually within the first few months after the incident. After those neurons that have been reversibly injured recover, the stroke patient can be left with impairments as described in the previous section.

### 2.5.2 Physical Therapy

Stroke rehabilitation is a restorative process that seeks to hasten and manage recovery by treating the disability caused through prevention of secondary complications, remediation (treatment to reduce neurological deficits), compensation to offset and adapt to residual abilities, and maintenance of function [23]. A well-planned rehabilitation scheme employs a team of medical professionals [12] in order to deal with the many facets of disability and impairment. There are certainly alternatives and complements to physical rehabilitation including medical and surgical procedures and the use of orthotics, though the remainder of this discussion will focus on physical therapy. The main goal of physical rehabilitation is to maximize motor performance

and minimize functional deficits within the constraint of the neurological deficit [14]. Two of the key players involved in achieving this goal are the occupational therapist (OT) and the physical therapist (PT). The difference between the two types of therapists is found in the distinction between impairment and disability. PTs attempt to address functional restoration of impairment, *i.e.*, the rehabilitation of gross motor function. OTs, on the other hand, attempt to address disability by working on functional activities and teaching compensatory strategies that will allow the patient to operate successfully within his environment.

In motor learning, the practice of a specific skill will not affect performance in another skill [1]. The inability to generalize is addressed by working on exercise in the context of functional activities. Wrist and forearm articulation play an important role in enhancing the usefulness of the hand by allowing it to take up a variety of orientations with respect to the elbow. One can imagine that forearm articulation is prominent in turning tasks. Examples of tasks requiring wrist rotation include painting, waving, flipping a switch, and throwing a curve ball. Measures of the ranges of motion of functional wrist activities through the course of a day show that 50° of flexion and extension, 12° of radial deviation, and 40° of ulnar deviation are common. An immobile wrist can force a person to compensate with exaggerated upper arm movements that are not even entirely successful. It is, therefore, beneficial to focus on the restoration of wrist and forearm functionality.

Patient evaluation in rehabilitation is largely one of function. There are a number of clinical scales meant to indicate levels of disability or impairment, all with varying degrees of uncertainty and subjectivity. Some, like the Manual Muscle Test (MMT) and Fugl-Meyer, attempt to address impairment by assigning scores from an ordinal scale to specific motions as judged by the therapist. Others, like the Functional Independence Measure (FIM) and the Barthel Index focus on the patient's ability to execute common activities of daily living (ADL), with scoring based on the amount of assistance needed. Evaluation equipment is available for more objective measurements such as dynamometers or the goniometer shown in Fig. 2-9. In clinical practice, however, evaluation of quantities like tone, strength, and range of motion is often

qualitative.

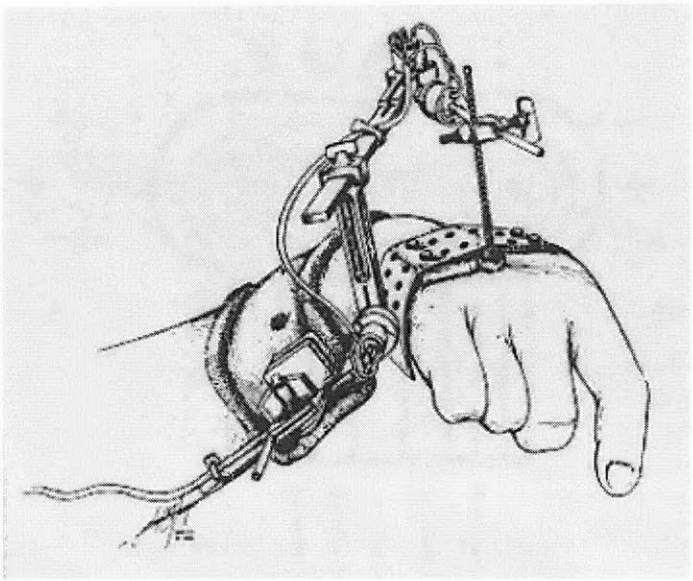

Figure 2-9: A multi-degree-of-freedom wrist goniometer [47].

This discussion will close with a review three of the major thrusts of wrist and forearm therapy. In order to combat contracture and otherwise stiff joints, therapists will employ what is known as continuous passive motion (CPM) exercises. In these exercises, the patient's joint is forced through its range of motion a number of times. Commercial devices exist to automatically administer this type of therapy, some examples of which are seen in Figs. 2-10. The other two important types of therapy require more patient involvement. With resistance and strengthening exercises, the patient is encouraged to withstand forces and move against forces, respectively. The Multiwrist, shown in Fig. 2-11, is advertised as a portable solution to wrist exercise and assessment needs. It is configurable to provide resistance to each of the motions targeted by the wrist robot, though it is only capable of one motion at a time. Resistance is achieved by stacking weights like many universal exercise machines and the device comes with optional digital angle measurement capabilities.

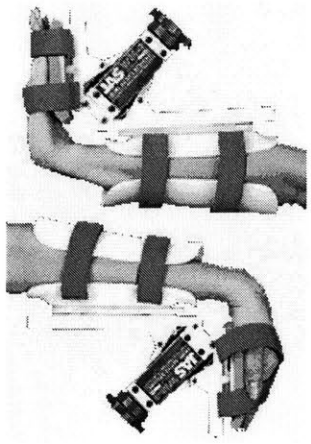

(a) Device for wrist rotations.

(b) Device for forearm rotations.

Figure 2-10: Some commercially available CPM devices by Joint Active Systems, Inc. [59].

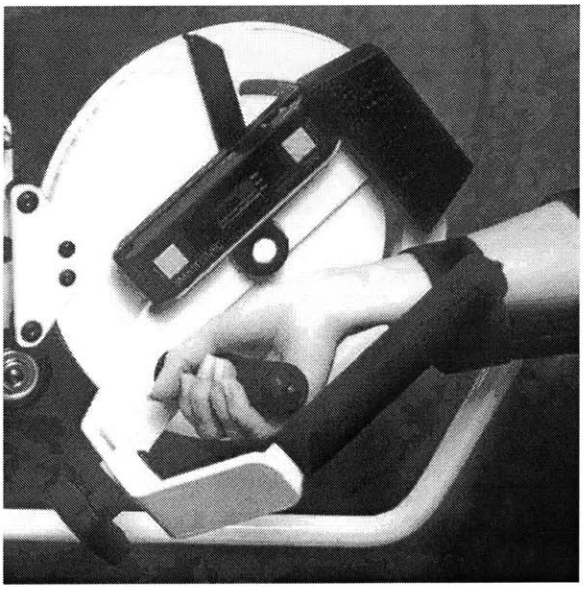

Figure 2-11: The Multiwrist [61], a commercially available device for wrist exercise.

## 2.6 Implications

This chapter has covered the basic biology necessary for understanding the motivation for and execution of this project. Each topic presented here is an active area of research in its own right. It is anticipated that the completed wrist robot will not merely take its place as an advanced rehabilitative tool, but also serve as a research tool in many of these fields. Summarizing the main points to take from this discussion:

- Discussion of anatomy and anthropometry helps define the proper mechanical design constraints.
- The articular complex of the wrist can be approximated by a two-degree-of-freedom joint whose axes are perpendicular, but whose ranges of motion are coupled.
- The axis of forearm rotation is not parallel to the long bones of the arm throughout the range of motion and is referenced to a plane defined by the arm.
- Knowledge of the limits of human perception should also be considered in determining functional requirements for the hardware.
- Stroke can adversely affect human ability in motor control, though the brain's resiliency allows for motor recovery.
- Currently, physical therapy techniques for the wrist involve continuous passive motion, strength training, and resistance exercises, occasionally using commercially available mechanisms.
- Properly implemented, the device described in this thesis could provide objective measurements that will benefit studies on the nature of human movement and motor recovery.

# Chapter 3

# System Overview

The current design of the wrist robot is the work of former Master of Science student Dustin Williams. The reader is referred to Dustin's thesis [54] as a source for understanding the thought that went into the design process. A great deal of perspective has been gained through the re-examination of that design and experience with its hardware. This chapter presents the features of the robot and points out some of the more important differences between the original design and the present implementation. A more complete listing of the necessary modifications is provided in Appendix C. Figure 3-1 shows the robot as ultimately deployed at the Burke Rehabilitation Hospital.

Note that throughout the remainder of this thesis, the following nomenclature will be used:

**PS:** The motor (or corresponding axis) controlling pronation and supination, located at the back of the assembly.

**ADL:** The left motor (from the point of view of the patient) controlling abduction and adduction as well as flexion and extension movements.

**ADR:** The right motor, complementary to ADL.

**DIFF:** The motors controlling the differential, *i.e.*, ADL and ADR together.

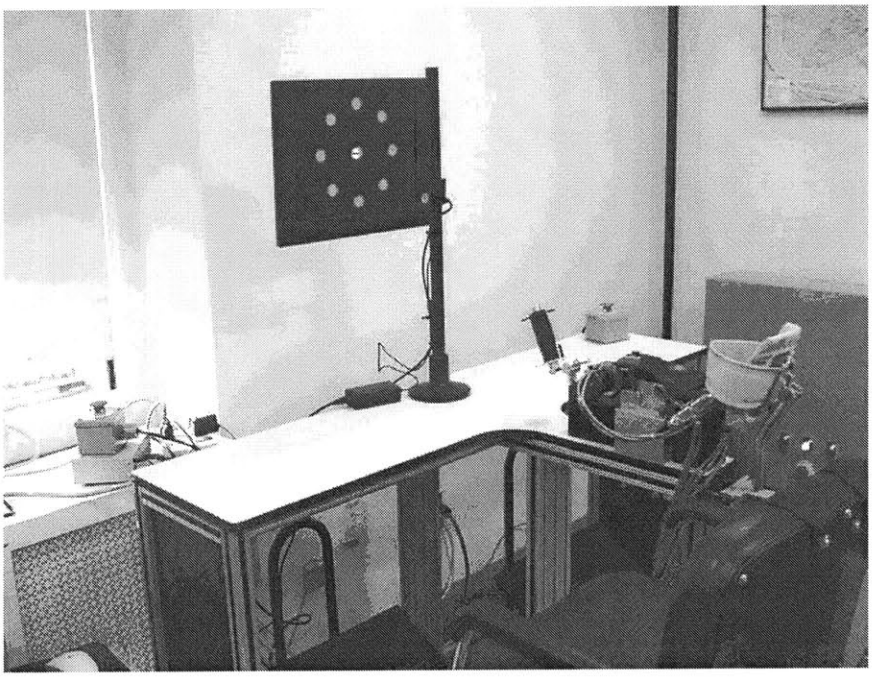

Figure 3-1: Photograph of the wrist robot, currently installed at the Burke Rehabilitation Hospital.

## 3.1 Functional Requirements

In laying out the framework for the design of the wrist robot, it is important to tie in the information presented in the preceding chapter. This section reviews the quantified functional requirements devised by Williams [54] and attempts to comment on their appropriateness within the context of the information presented in Chapter 2. Overall functional requirements filter down to define the specific requirements for each component of the design. The effects of these choices and the extent to which the overall requirements were met are subjects that are revisited throughout the remainder of this thesis.

### 3.1.1 Ranges of Motion

The most basic requirement for this device is that it provide for motion of the wrist and forearm. Table 3.1 summarizes the stated design requirements and chosen ranges [54] for each targeted motion. The discussion from Chapter 2 suggests that the

| Motion | Desired Range | Designed Range |
|---|---|---|
| Wrist Flexion | 70° | 60° |
| Wrist Extension | 65° | 60° |
| Wrist Abduction | 15° | 20° |
| Wrist Adduction | 30° | 30° |
| Forearm Pronation | 90° | 76° |
| Forearm Supination | 90° | 76° |

Table 3.1: Initial functional requirements for the robot's range of motion [54].

designed ranges would be appropriate for abduction, flexion, and extension, as they exceed the ranges expected during normal functional tasks. Wrist adduction could prove somewhat problematic, as its designed range of motion is 10° less than the maximum expected excursion in functional tasks[1]. The designed ranges for pronation and supination seem useful, but recall that this value is a measure of the handle orientation in a lab reference frame and is not a measure of the patient's own forearm articulation. This situation will be discussed more fully in section 3.5.

### 3.1.2 Required Output Torques

Experimentation prior to the design [54] estimated that useful therapy would require 170 oz·in from the differential axes and 240 oz·in from the PS axis. It is neither expected nor desired that the robot be capable of exerting forces comparable to the maximum strengths mentioned in section 2.1. The robotic therapist's goal is to assist in patient motion; patients exhibiting hypertonicity or otherwise stiff joints may require some type of CPM treatment before using this device. The effects of spastic reflexes is not entirely known. Determination of more appropriate strength levels will be borne out through pilot studies with stroke patients.

[1]Recall from section 2.5.2 that 40° of wrist adduction is common in everyday tasks.

### 3.1.3 Endpoint Impedance

One of the important features of MIT-MANUS is its backdrivability, a property that comes from its low mechanical impedance as seen from the endpoint. Closed-loop control for this robot is accomplished using position feedback, as will be seen in Chapter 6. There is no force-feedback nor any intention to use a twice-differentiated position signal for inertia compensation. This places the onus on the designer to prevent the mechanical impedance from being dominated by endpoint inertia. Endpoint friction, which presents its own set of control problems, should also be avoided. Inertia specifications were qualitatively determined at $10 - 15\,\text{lb}\cdot\text{in}^2$ for each of the three axes in question [54]. Frictional forces less than $30\,\text{oz}\cdot\text{in}$ were also deemed backdrivable [54].

Using an argument based on human perception, the most restrictive requirement on endpoint inertia occurs where the robot is acting in a "passive[2]" sense, so that the reference force is the inertial load felt by the patient. This translates to an inertia requirement for the robot of 7 % of the human limb inertia of each axis. Such an exceedingly restrictive design requirement is not merely unrealistic, it is unnecessary. While part of the goal is to introduce hardware that will interact transparently with the human dynamics, feeling some inertia from the device is not prohibitive. In truth, as long as the machine is backdrivable in passive operation, the endpoint inertia is adequate. This is due to the fact that, in general, the robot will be active and the accelerations will be low, meaning the inertial load will be small in comparison to the reference force. In robot-assist mode, the inertia will likely be more difficult to notice, since the reference forces will be dominated by the actuator effort and, presumably, lower than any encountered inertial load[3].

Choosing an appropriate limit for friction is an even more ambiguous task. To begin with, this depends on the nature of the friction considered. There are a number of different models that describe tribological phenomena. In this thesis, static, kinetic, and viscous friction will be discussed. Dry friction, encompassing static and kinetic

[2]When referring to robot operation, the term passive is meant to imply that the robot has no preferred position and, therefore, is not assisting the patient toward any equilibrium point.

[3]Realize that as a therapeutic device, the robot will be operate at low speed and potentially high torque. Actuator effort should influence patient motion much more than inertial loads.

friction, is often modeled as the meshing of asperities on the surfaces of two contacting bodies. The effective contact area is proportional to the normal load, as seen through Hertzian contact stress analysis, and not related to the geometric contact area. Static friction, or stiction, is generally higher than kinetic friction. This causes problems at low velocities, as the system is liable to exhibit stick-slip type behaviors. Velocity-dependent friction should be designed to be small compared to the desired environment damping added through control and the poorly defined damping that is naturally present in the human joints. Friction is notoriously difficult to characterize and is often highly position dependent, making many control strategies difficult to implement. Suffice it to say, it is in the best interest of the design to minimize frictional contributions. Should it become desirable to introduce damping effects, this can be done by controlling the actuators.

## 3.2 Actuation

The system uses three Kollmorgen brushless servomotors to generate motion. The ADR and ADL motors are both model RBE 711 motors, and the PS motor is an RBE 712, all of which have 6 magnetic poles (3 pole pairs) on the rotor. Brushless servomotors were chosen due to their potential for higher torques, lower speeds, and better heat dissipation [54]. Briefly, brushless motors replace mechanical commutators (brushes) with electrical commutation. Permanent magnets on the rotor are affected by the phase currents developed in the windings of the stator. Ideally, these actuators should produce a torque proportional to the input current. In reality, torque pulsations[4] cause the actual torque to depend on the electrical position of the rotor. For practical reasons, the windings are bunched together in slots, producing irregularities in the magnetic circuit and, consequently, preferred rotor positions known as cogs. These motors have skewed slots in order to alleviate cogging torques. The other form of torque pulsation worthy of note is torque ripple, a position-dependent variation

[4]Torque pulsation is a term that will be used to refer to any phenomenon that causes the actuator torque production to vary from the ideal. The main types of torque pulsation discussed in this thesis are cogging torque and torque ripple.

in the torque constant of the motor that results from the position-dependence of the mutual inductance between the rotor and windings.

Three phase current is supplied to each motor using SERVOSTAR CD model CE06 servo-amplifiers. These servo-amplifiers, essentially voltage-controlled current sources, provide for commutation of the motor using encoder feedback[5]. The currents sent to the motors are actually the outputs of an internal feedback loop that adaptively compensates for disturbances such as load irregularities using Kollmorgen algorithms and updating at 16 kHz. Current is generated using pulse width modulation (PWM), a method that encodes an analog signal as a digital one; the output of each phase of the servo-amplifier is a pulse train that switches at a frequency of 16 kHz, the duty cycle of which is modulated to correspond to given analog signal level[6].

The servo-amplifiers commutate the motors sinusoidally. This type of commutation requires a properly indexed, high resolution encoder signal. The servo-amplifier is capable of receiving encoder inputs up to 3 MHz. Sinusoidal commutation can help reduce torque ripple and increase efficiency when compared to simpler commutation schemes (*e.g.*, six-step/trapezpoidal). Among the options available with the Kollmorgen servo-amplifiers is a feature known as Angle Advance. In normal three phase current commutation, the phases are separated electrically by 120°. With Angle Advance, the electrical phase of each current is set some fixed amount ahead of the commutation table, creating a magnetic field that opposes the field from the permanent magnets. This field weakening is a method for developing torque at speed [13, 24]. For this application, the actuators are expected to produce high torque while operating at low speed, removing the advantages offered by field weakening. Accordingly, this feature was disabled.

[5]The servo-amplifiers also receive feedback from the Hall effect sensors embedded in the motor windings. The coarse position information provided by these sensors is only used on power-up until the encoder's index bit has been sensed.

[6]The signal is digital, but the high switching frequency renders it effectively analog.

| From | To | Change in Count |
|---|---|---|
| (1,0) | (1,1) | +1 |
| (1,1) | (0,1) | +1 |
| (0,1) | (0,0) | +1 |
| (0,0) | (1,0) | +1 |

Table 3.2: Encoder state transition table. States are given as ordered pairs (**A**,**B**). Changes in state are shown for forward travel. For reverse travel (transitions for which the change in count is -1), interchange the **To** and **From** columns.

## 3.3 Sensing

The sole source of feedback for the controller is provided by the incremental optical encoders mounted on each motor shaft. The three encoders used for the PS, ADR, and ADL motors are identical; they are all Gurley R119 encoders with 1024 lines per revolution and 10X onboard interpolation. After quadrature, this gives a resolution of 40960 counts per revolution. The encoders send differential signals as outputs, increasing signal stability, and include an index pulse to find absolute position. These encoders have a maximum output rate of 500 kHz, placing an upper limit on the speed that can be achieved without missing counts. The encoder signal is read by the counter card and the servo-amplifier[7]; missed counts by the counter card will disrupt the feedback to the controller while missed counts by the servo-amplifier will lead to improper commutation. In both cases, the resulting operation of the actuator becomes unpredictable. Figure 3-2 shows a typical position response to a smooth input[8]. Perfect encoder operation should provide a mirror of this input, which would appear linear in the range shown. The "wobble" seen is repeatable in position for different input torque rates and magnitudes.

Basic encoder operation involves light emitted and detected on opposite sides of a glass disk. The disk contains alternating opaque and transparent sections so

[7]The USDigital encoder card interprets the encoder signal differently from the Kollmorgen servo-amplifier. The **A** and $\overline{\mathbf{A}}$ signals from the encoder are reversed going into the amp or the counter card depending on the encoder mounting details.

[8]The input command is actually a slow sinusoid.

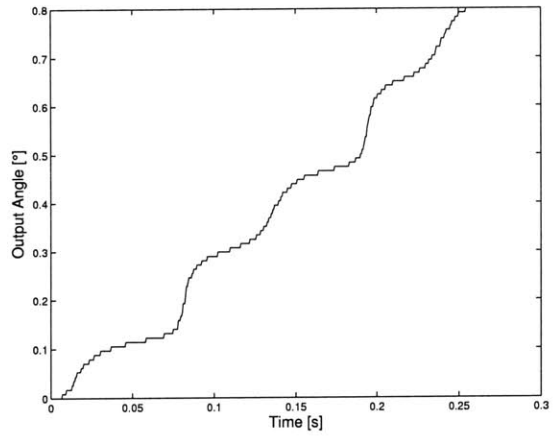


Figure 3-2: Encoder wobble: response of encoder to an open loop torque command during a quasi-locked rotor test. The input command is a slow sinusoid, which should be reflected by the rotor response.

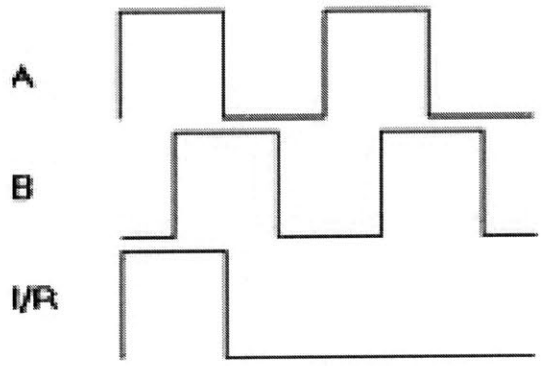


Figure 3-3: Encoder output signal: directional information is obtained by a quadrature decode of the pulse trains.

that a sensed channel will read either "on" or "off." As shown in Fig. 3-3, the two channels are separated electrically by 90° to make up the quadrature encoded signal. This allows for four possible encoder states; counts are added or subtracted depending on the order the states appear, as summarized in Table 3.2. In mounting the encoder to the actuator, there is inevitably some eccentricity between the motor shaft and the encoder shaft. Since the disk is attached to the shaft, any loading on the encoder housing while the shafts rotate will tilt the disk with respect to the internal electronics. One can imagine that this may distort the phase separation between the two channels or, perhaps more likely, distort the duty cycle of the pulse train; interferometric effects can broaden the light signal and cause a false reading of the sequence of transitions. Figures 3-4 represent two scenarios in which the nature of the quadrature signal is distorted. With no phase distortion, *i.e.*, **A** leads **B** by 90°, and a pulse train duty cycle of 50%, these curves would appear as straight lines with a slope of 1. The simulations presented are simple in that they introduce a constant phase distortion between the channels or a constant change in the duty cycle of the channels. Adjusting these values disrupts the accuracy of encoder reading and can, as in Fig. 3-4(b) lead to situations where the signal reverses direction. Considering the possibility of a position-dependent distortion creates even more potential distortion profiles. This provides a plausible explanation for the origin of the encoder wobble observed in Fig. 3-2.

Predictable actuator performance depends on the accuracy of the encoder reading sent to the amplifier. Over-constraining the encoders has caused inaccurate position readings in line with the above discussion, leading to actuator failure. In order to prevent cases like the one shown in Fig. 3-4(b) from occurring, it was necessary to adjust the encoder mounting. Figure 3-5 shows the location of ADR and ADL encoders, mounted on the inside of the transmission housing[9]. These encoders come with compliant, leaf spring mounts. Originally, these mounts were deformed to fit into the space allotted (see Fig. 3-6(a)). In this configuration, the effects noted in Figs. 3-4 precluded reliable operation of the actuators, as folding the edges of the leaf

[9]The details of the transmission housing will be covered in subsequent sections.

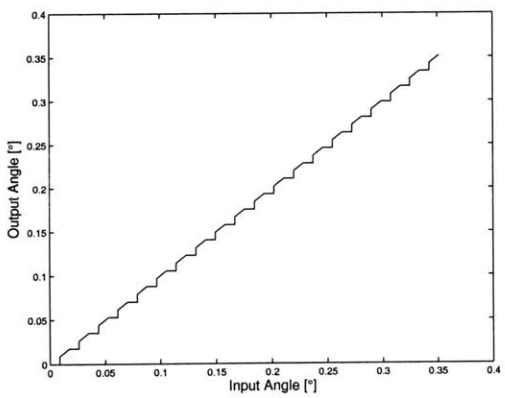


(a) Phase distorted so that **A** leads **B** by 140 °.

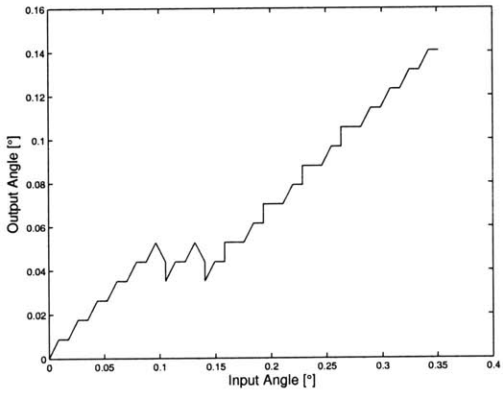


(b) Duty cycle distorted to 75%.

Figure 3-4: Simulation of corrupted quadrature decode.

mount made it stiff enough to introduce transverse loads on the encoder housing. A custom compliant mount, shown in Fig. 3-6(b), was fashioned out of spring steel and held in place by rubber stops. This mounting option allows the encoder to move in response to side loads (due to shaft eccentricity) while disallowing encoder rotation with respect to the motor[10]. The combination of using these mounts and removing enough material from the transmission housing for the encoder wires to fit through makes actuator operation possible.

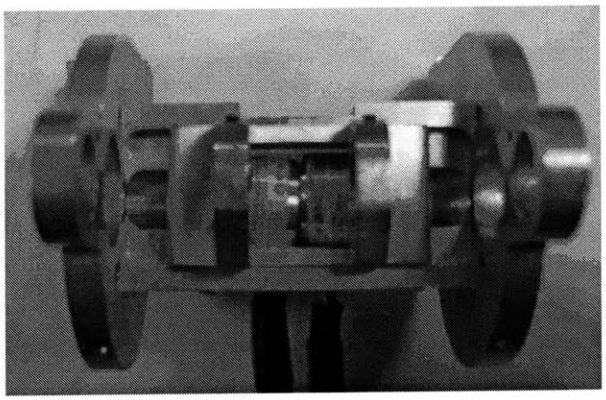

Figure 3-5: DIFF encoder placement within transmission housing.

[10]Clearly any rotation of the encoder with respect to the motor would render the encoder readings meaningless.

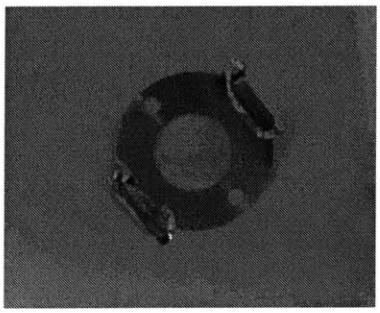

(a) Initial encoder mount.

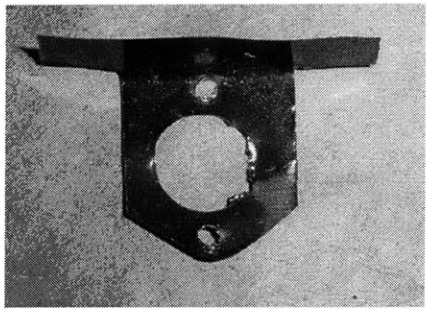

(b) Prototype custom compliant mount.

Figure 3-6: Mounting options for DIFF encoders.

## 3.4 Transmission

### 3.4.1 Gears

Gears are one of the oldest machine components, providing for the transmission of power between two shafts. Since gears play such a central role in the design of this hardware, it makes sense to cover some of the basic aspects of gearing and gearing practice. Obviously, not all aspects of this mature field will be addressed. The main concern here is general power transmission and interaction forces. Dynamics of individual tooth interactions will not be covered. The fundamental law of gearing states that the angular velocity ratio between two gears in contact is constant, as seen in Eq. 3.1,

$$m_V = \frac{\omega_g}{\omega_p} = \pm\frac{r_p}{r_g} = \pm\frac{N_p}{N_g} \tag{3.1}$$

where $m_V$ is the angular velocity ratio, $\omega$ is angular velocity, $r$ is the pitch radius, $N$ is the number of teeth, and the subscripts $p$ and $g$ stand for pinion and gear, respectively. Assuming lossless power transfer, this corresponds to a constant torque ratio,

$$m_T = \frac{1}{m_V} = \pm\frac{N_g}{N_p} \tag{3.2}$$

Mating teeth contact at a point known as the pitch point. The most common gear tooth profile is an involute curve, whose shape ensures a common tangent at

the point of contact. The transmission axis differs from the direction of travel of the pitch point by the pressure angle $\phi = 20\,^{\circ}$. The pitch circles of mating gears are meant to be tangent to each other. One consequence of using the involute profile is that changes in center-to-center distances will not affect the gear ratio. They will, however, affect the pressure angle. Power transmission is accomplished through a combination of rolling and sliding at the pitch point. Friction and wear are reduced in such situations by using lubrication. Open gearing systems, like the one used in the wrist robot, are limited to dry lubricants such as graphite.

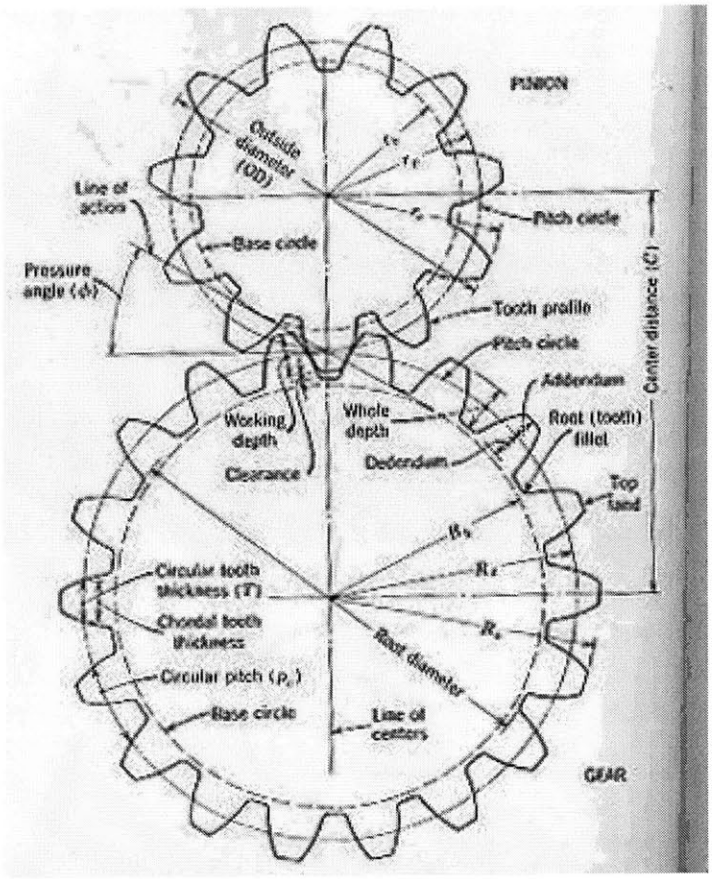


Figure 3-7: Basic gear nomenclature [37].

Figure 3-8 depicts the concept of backlash, the clearance between the mating teeth as measured along the pitch circle. The uncertainties inherent in the manufacture of gears, especially considering the quality of the gears used here, make the existence of backlash inevitable. Some backlash is generally necessary to allow for the flow of lu-

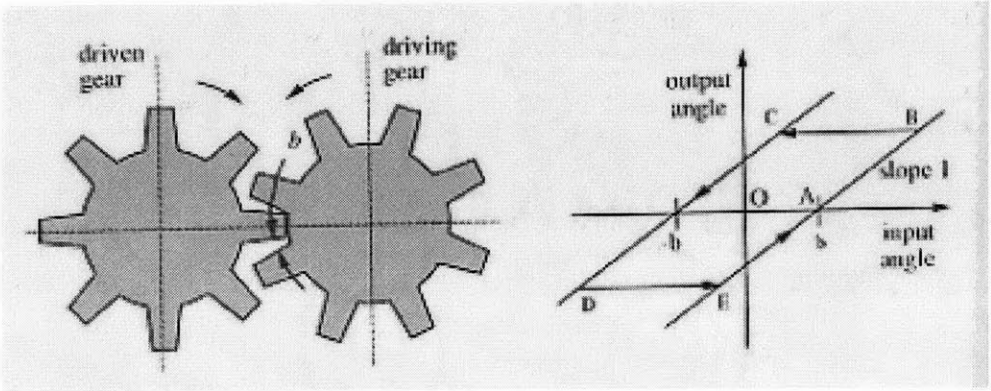


Figure 3-8: Gear backlash [49].

bricants. Backlash becomes problematic during torque reversals, making it a primary concern in this design. It creates noise during operation, adds to position uncertainty, and acts as a destabilizer, contradicting the design goal of smooth operation. There are a number of accepted ways to deal with backlash in the design phase [37] including the use of anti-backlash gears or auxiliary gear trains. One method that is built into this design is adjustable center-to-center distances. Along with tooth thinning, center-to-center distance tolerances are probably the most common introducers of backlash into a system. Equation 3.3 is an approximation of the angular backlash introduced as a function of the error in center distance, $\triangle C$, and the pitch diameter of the gear being measured, $d$.

$$\theta_B = \frac{4 \cdot \tan\phi}{d} \triangle C \tag{3.3}$$

Built-in adjustability places a strong emphasis on the assembly of the mechanism. Because both ends of the shaft are independently adjustable, it becomes difficult to ensure shaft parallelism [37]. This method is even more suspect when applied to multiple stage gear trains. The potential to build up error suggests that at most, only the final stage should have an adjustable position shaft axis.

The wrist robot includes spur gears and bevel gears. Spur gears are the most basic type of gears, while bevel gears allow for the transmission of power between

intersecting shafts. Bevel gears can be manufactured to account for any intersection angle, but are most commonly seen driving shafts at right angles, as is the case with the differential. The basic system consists of a differential gear mechanism that drives the axes of wrist rotation. Pronation and supination are accomplished through the actuation of a curved slider attached to the rest of the mechanism. The remainder of this section deals mainly with the transmission of power from the actuators to the robot handle.

### 3.4.2 PS Transmission

In analyzing the system, it is convenient to consider the PS transmission separately from from the differential transmission. The differential transmission housing and its two motors are carried by the PS motor through two Bishop Wisecarver 180° geared slide-rings. These ring gears sit in a bearing block as in Fig. 3-9. The gear ratio between the motor pinion and ring gear is 10.5. The two ring gears are coupled using the normal force generated by two bolts. The spacers around these bolts also serve as mechanical limits, restricting the range of motion to 76° in each direction. Positioning the PS motor with so that the pitch circle of its pinion is tangent to that of the ring gear is critical for the operation of the system. The PS motor mounts to the bearing block using four bolts into its face. The bearing block itself has thru-holes for these bolts, adding a degree of uncertainty to the ultimate motor location. To minimize, or at least standardize, this problem, the relative heights of the PS motor cover and the bearing block were set by bolting them both to mechanical ground with the motor[11] shimmed up to the appropriate height[12].

The original connection between the transmission housing and the ring gears was restricted to the bolts through the edges of the ring gears. Figure 3-10 shows the step taken to relieve the stress at this joint. Using two of the pre-existing holes in the ring gear, the back of the transmission housing was modified so that it could be bolted

[11]The actual motor height is still not certain, as the PS motor is not rigidly connected to the PS motor cover.

[12]The step in height is actually machined into the robot's table mounting block in place of trial-and-error shimming.

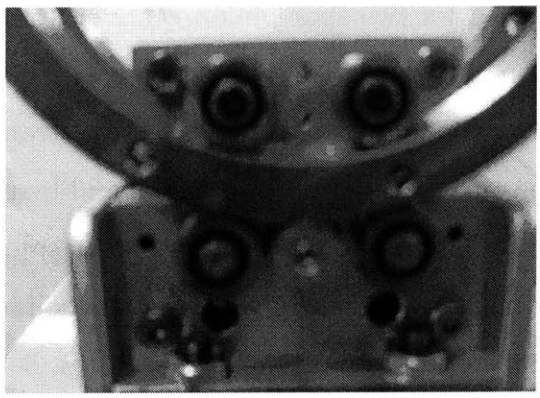

Figure 3-9: Ring gear in roller bearing block.

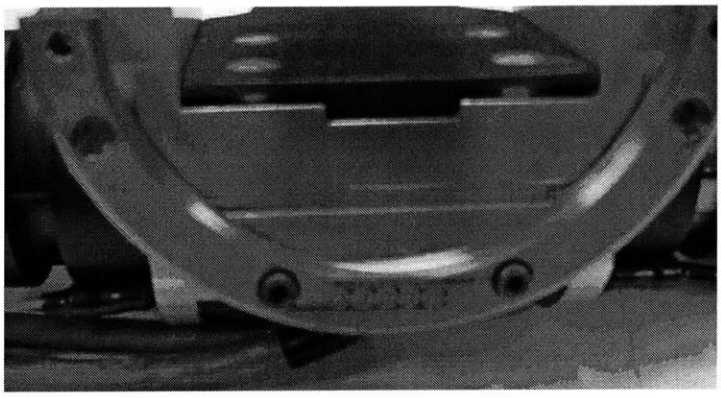

Figure 3-10: View of ring gear support.

in place. The transmission housing and the distal ring gear are now effectively one piece. Downward loads that would tend to bend the bolts are now transmitted to the ring gear's bearings.

The original design called for two spur pinion gears on the PS motor shaft, each meshing with one of the curved racks. The second, more distal, gear was pressed on in an attempted anti-backlash configuration. The load of the transmission housing was borne by one of the pinions in one direction of rotation and by the other pinion in the other direction of rotation. This made the system feel much smoother in passive robot operation. Testing with the system, however, showed a peculiar instability in the PS axis that was excitable using open loop commands (see Figs. 3-11). Constant torques were applied and equilibrated at the handle by hand. The system audibly vibrated at 193 Hz with low amplitude vibrations of the pinion on the order of 0.25°. The cause of the instability was determined to be vibration of the PS motor shaft. This shaft, supported by the motor bearings, is effectively cantilevered with two points of loading (one at each pinion). When the tooth interaction force is at the distal gear is great enough, the shaft will deflect and allow the proximal gear to come into contact with its ring gear. At this point, the load is taken up by the proximal gear and the shaft is able to spring back toward its equilibrium position. Once the distal gear re-establishes contact, the cycle repeats itself.

This hypothesis is validated by considering the vibration of continuous systems. For a beam undergoing transverse vibrations, the natural frequency, $\omega$, is given by

$$\omega = (\beta l)^2 \sqrt{\frac{EI}{\rho A l^4}} \tag{3.4}$$

where $E$ is the Young's modulus (200 MPa for steel), $I$ is the moment of inertia ($I = \frac{\pi d^4}{64}$ for a cylindrical beam), $\rho$ is the density (7800 $\frac{\text{kg}}{\text{m}^3}$ for steel), $A$ is the cross sectional area, $l$ is the length of the beam, and $\beta$ is a characteristic constant with $\beta l = 1.875$ for the first mode of a fixed-free beam. Calculating the natural frequency of the first mode of vibration using Eq. 3.4 gives a predicted natural frequency of 230 Hz. This does not take into account the extra mass provided by the brass gear

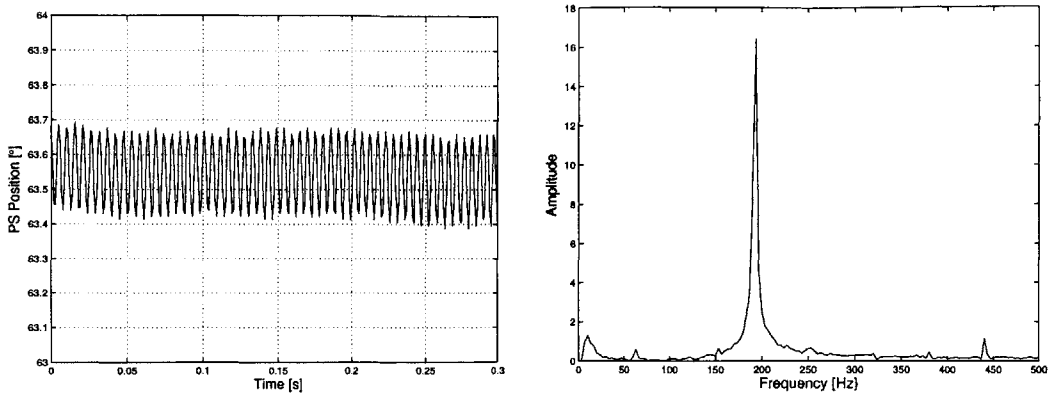


(a) Position response, amplitude around 0.25 °.

(b) Frequency response, peak around 193 Hz.

Figure 3-11: Structural instability in PS axis resulting from constant torque input, $\tau_p = 0.2\text{N} \cdot \text{m}$.

itself, which would tend to lower the estimate towards the observed frequency of 193 Hz. Further validating this hypothesis, the problem occurs in one direction only, presenting itself any time the torque exceeds roughly 30% of the maximum torque capability of this axis ($41.4 \cdot 10^{-3}$ Nm of motor torque). Since this instability proved so limiting to the production of force in this axis, the brass pinion was removed. The problem was indeed eliminated, but some of the backlash in the axis was re-introduced.

### 3.4.3 Differential Transmission

Wrist rotations are accommodated by a differential gear mechanism. The system, depicted in Figs. 3-12, is actuated by the ADL and ADR motors. The pinions on these motors, gears **A**, mesh with a compound intermediate gear stage, gears **B** and **C**. Gears **C** then mesh with gears **D**, the differential end gears, which are rotationally fixed to the differential end bevel gears controlling the spider gear. Table 3.3 summarizes the number of teeth on each gear, giving the overall gear ratio of each train as approximately 8.14. The mechanism is meant to provide a torque about any arbitrary axis that passes through the center of the differential gear through a combination of

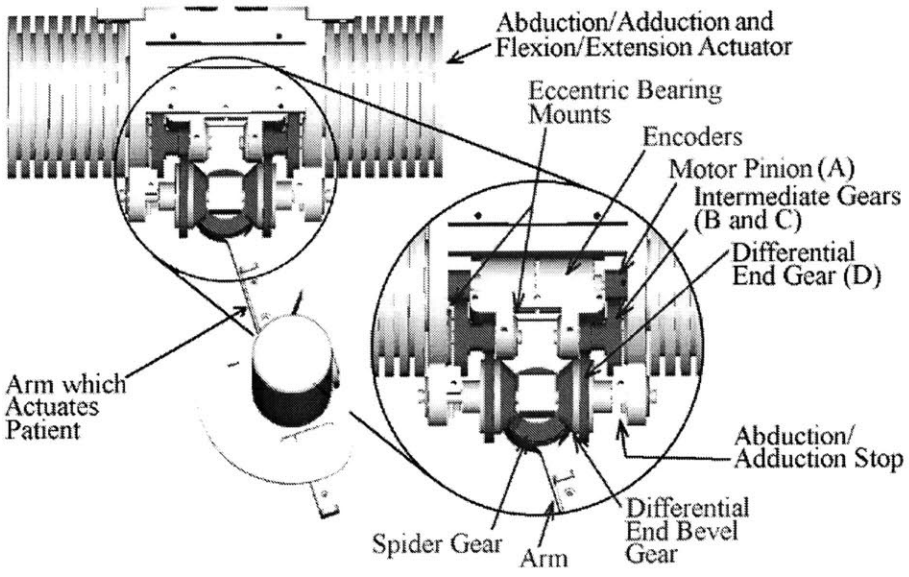


(a) CAD design with nomenclature [54].

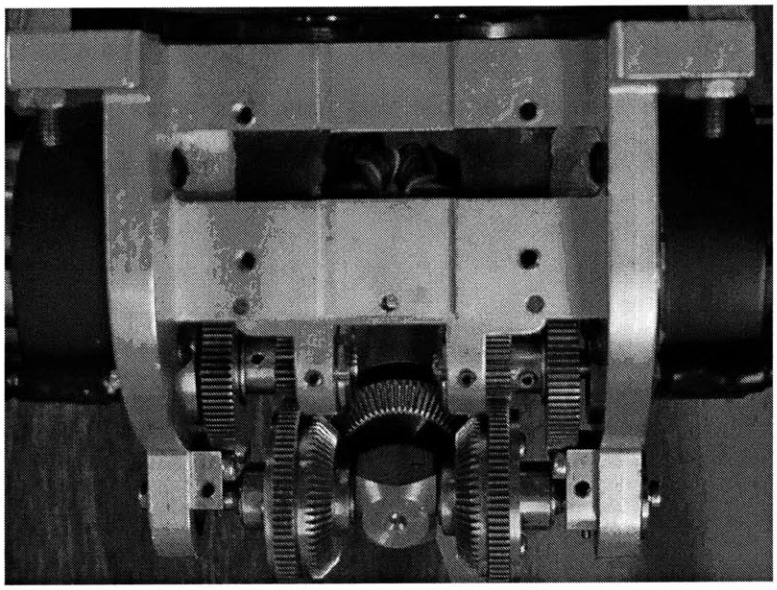

(b) Photograph of assembled transmission.

Figure 3-12: Differential transmission.

| Gear | Number of Teeth |
|---|---|
| A | 28 |
| B | 76 |
| C | 30 |
| D | 90 |

Table 3.3: Differential transmission gear teeth.

ADR and ADL torques. Each motor contributes equal components of vertical and horizontal motion when actuated (more specifically, each motor contributes equal components of adduction/abduction and flexion/extension torque). When ADR and ADL cooperate, the resulting motion is pure adduction/abduction; when these two motors are commanded to oppose each other, pure flexion/extension motion is produced. The following expressions summarize the differential gear basics:

$$\theta_{fl} = \frac{\theta_R + \theta_L}{2} \tag{3.5a}$$

$$\theta_{ad} = \frac{\theta_R - \theta_L}{2} \tag{3.5b}$$

$$\tau_{fl} = \tau_R + \tau_L \tag{3.6a}$$

$$\tau_{ad} = \tau_R - \tau_L \tag{3.6b}$$

where $\theta_R$ is the rotation of the right differential end gear (referenced to a neutral robot arm position), $\theta_L$ is the rotation of the left differential end gear, $\theta_{fl}$ is the flexion/extension angle of the robot arm, $\theta_{ad}$ is the abduction/adduction angle of the robot arm, and the corresponding torques are represented by the letter $\tau$. The sign convention used here is the same as that used by the encoders, *i.e.*, clockwise rotation of the motor corresponds to positive values. Also note that while the definition of a positive flexion angle depends on the handedness of the patient, a positive $\theta_{ad}$ always corresponds to abduction (radial deviation).

Motion is restricted by mechanical stops in the form of dowel pins in the shafts. These pins contact parts on the transmission housing to prevent excessive rotations.

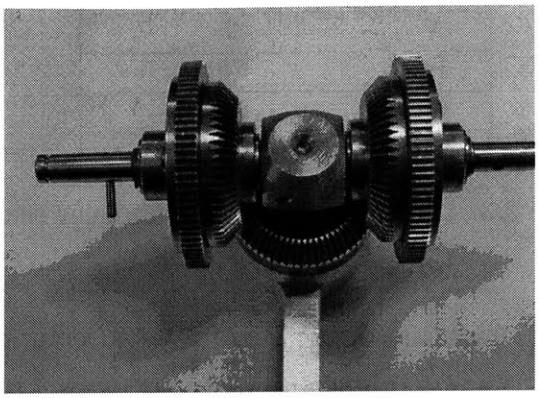

Figure 3-13: Differential gear with one of the abduction/adduction stops installed (left of figure).

The abduction/adduction stops are shown in Fig. 3-13 on the differential gear, while the flexion/extension stop, not shown, is a pin in the shaft of the spider gear. In what appears to be a manufacturing error, the hole in the spider gear shaft for the flexion/extension stop is tilted towards the right allowing more motion towards the ADR motor and opening the possibility for the robot to interfere with itself. Figure 3-14 displays the range of motion of the handle as expressed in robot joint coordinates.

Properties affecting the smoothness of operation of a gear set, such as friction, strongly depend on the quality of the gears used. Transmission errors, such as periodic fluctuation of the gear ratio, can result from imperfect tooth interactions. The ADR and ADL pinions are pinned onto their respective shafts with steel dowels[13] and, therefore, require holes. Figure 3-15 shows the effect of drilling holes into the finished gear. Tooth deformation is apparent near the area of material removal. In the assembly of the device, attempts were made to position the damaged sections of these gears away from the center of the workspace. The overall gear ratio tends to suppress the errors caused by these teeth, but future designs should incorporate more reasonable methods of gear attachment, such as using hubbed gears.

The intermediate gear stage is connected to the transmission housing with eccen-

[13]Ultimately, roll pins were used here. The roll pins were easier to insert into the assembly and offer a better opportunity for gear removal should that become an issue.

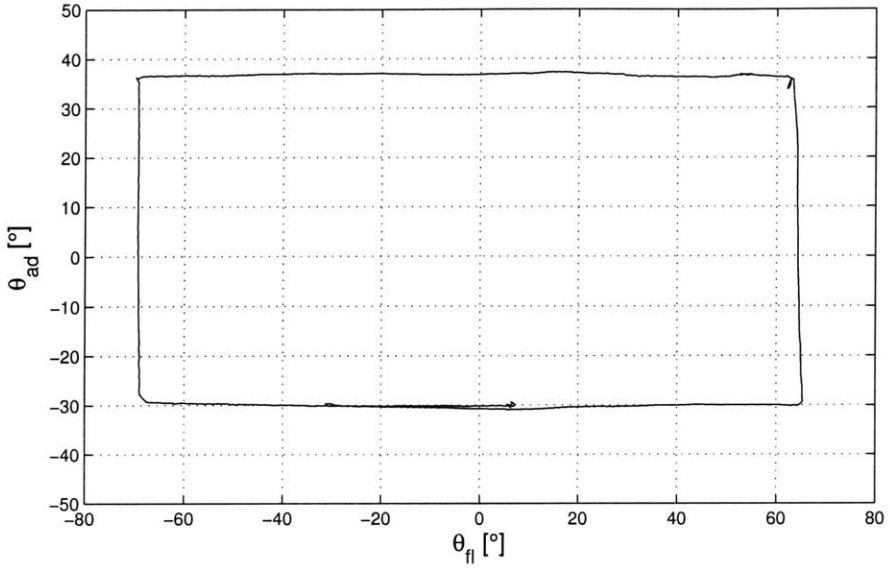


Figure 3-14: Recording of DIFF axes reachable workspace. Positive "flexion" angles correspond to rotation of the robot arm toward ADL. Notice that the robot arm can move further toward ADR due to manufacture of the stop.

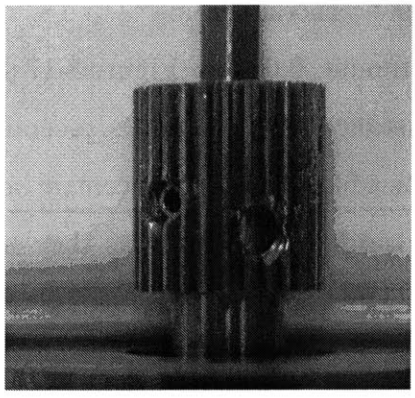

Figure 3-15: Motor pinion showing compromised gear quality as a result of machining.

tric bearings (noted in Fig. 3-12(a)). These bearings allow for some control over the distance between the axis of the differential end gears, the intermediate gear stage, and the motors. As mentioned earlier in this section, using adjustable gear centers as a means for backlash control is generally discouraged. The assembly problems introduced with such a method are only exacerbated by the fact that the actual position of the motor is poorly defined[14]. Assuming the motors could be aligned with their designed centers, the goal would be to position the intermediate gear stage so that the pitch circles for gear set **A** and **B** and the pitch circles for gear set **C** and **D** were tangent to each other. Unfortunately, the dimensions of the transmission housing do not allow both parts of this goal to be achieved simultaneously. The axis of the intermediate gear stage can exist at any point on a circle defined by the eccentric bearing[15]. The center-to-center distance for each gear set can be computed from the orientation of the eccentric bearing, $\theta$, from the law of cosines:

$$d_{\mathrm{AB}} = \sqrt{{d_{pg}}^2 + {e_c}^2 - 2 d_{pg} e_c \cos\left(\theta + \frac{\pi}{2}\right)} \tag{3.7a}$$

$$d_{\mathrm{CD}} = \sqrt{{d_{dg}}^2 + {e_c}^2 - 2 d_{dg} e_c \cos\left(\frac{\pi}{2} - \theta\right)} \tag{3.7b}$$

where $d_{pg}$ is the distance between the pinion axis and the eccentric bearing mount axis, $d_{dg}$ is the distance between the differential shaft axis and the eccentric bearing mount axis, $\theta$ is the orientation of the eccentric bearing[16], and $e_c$ is the offset of the eccentric bearing from the center of its mount, 0.008 in. Figure 3-17 plots the difference between the actual center-to-center distance and the center-to-center distance required by the pitch circles ($\Delta C$ in Eq. 3.3) as a function of the eccentric bearing orientation. Clearly, any negative values are not viable for assembly as they will result in inappropriate gear meshing. This leaves assembly options available for bearing orientations between

[14]Like the PS motor, the ADR and ADL motors are mounted using thru-holes in the transmission housing, allowing some play in the final motor positions.

[15]This is assuming the shaft axis is parallel to the other shaft axes. The independent adjustment of the two ends of this shaft increase the likelihood that the shaft axis will actually be skewed from the rest of the mechanism.

[16]This is a measure of the angle between the notches on the eccentric bearing and a convenient reference axis to give the stated equations.

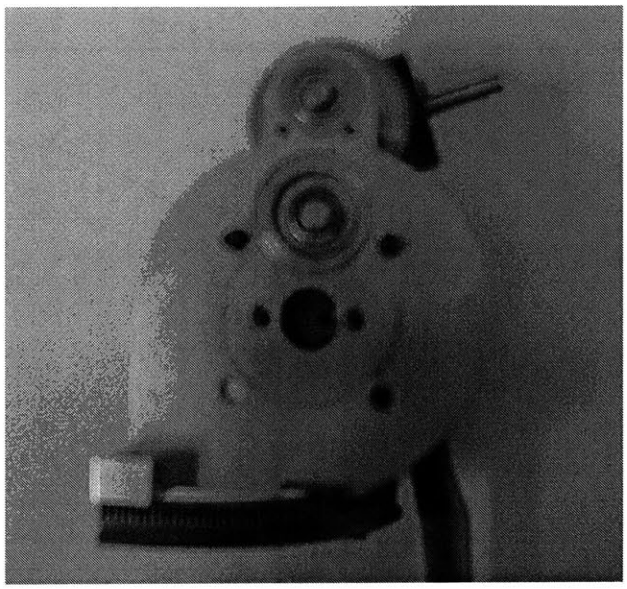

Figure 3-16: Side view of the differential transmission housing; notice the eccentric bearings.

$-3\,^\circ$ and $-19\,^\circ$. The stage was positioned to equalize the backlash present in the two gear sets, so that the intersection of the two curves of Fig. 3-17 was targeted. This was a rough guide for orienting the eccentric bearing, which ultimately had to be adjusted according to the feel of the device. This procedure would set the centers for each gear set slightly over 0.001 in. further apart than their pitch circles would require, which corresponds to angular backlash according to Eq. 3.3. In hindsight, it would have been more appropriate to eliminate the backlash between the pinion and gear **B**. In this scenario, the backlash would have been confined to only one gear set and there would be more inertia in the backlash region. Presumably, this would favorably modify the nature of the backlash instability discussed in Chapter 6.

The differential gear exhibits structural instabilities similar to those found with the PS axis, though much less perceptible. These instabilities are independent of feedback, appearing as sustained oscillations while a constant torque is applied to one or both of the DIFF actuators. The vibrations are perceptible in a tactile sense, but neither make excessive noise nor move the handle around. Figure 3-18 shows a manifestation of this instability, attributed to deflection of the differential shaft.

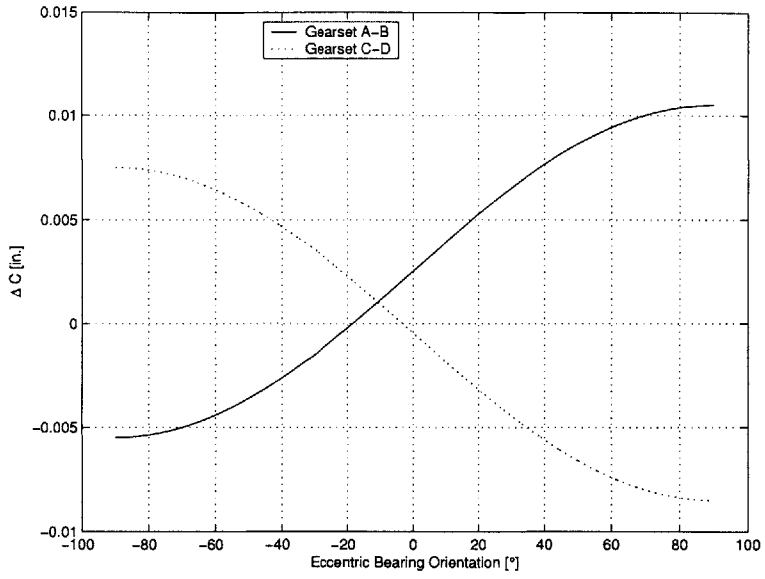


Figure 3-17: Results of eccentric bearing calculation. During assembly, the eccentric bearing was oriented near the intersection of the two curves in an attempt to minimize the backlash in each gear set.

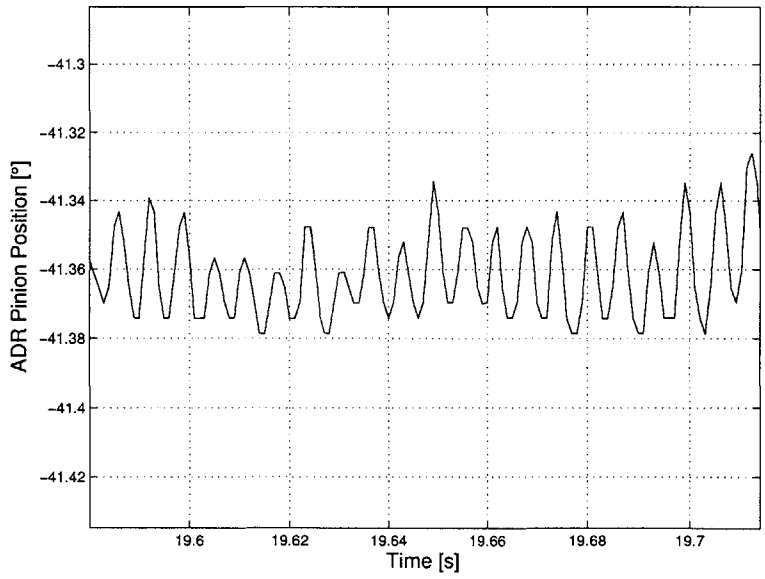


Figure 3-18: Typical structural instability in DIFF axis (ADR shown). Due to the fact that the handle is held in place (rather than fixtured), there is some movement of the mean position over time.

Shaft deflection is observable at significant loads, again due to gear teeth interactions. Oscillations arise from the shaft deflecting until it is no longer in contact with the loading gear. The shaft is then able to spring back towards its un-deformed state, at which time the cycle repeats. There is no immediate solution for this situation; the robot is capable of performing in spite of it. However, future versions of the design should carefully consider the stiffness of the differential shaft in response to the loads it will encounter.

## 3.5 Patient Attachment

Patient positioning at the device is critical for operation. The original kinematic analysis called for four degrees of freedom between the robot arm and the handle. This design, as sketched in Fig. 3-19, calls for three perpendicular revolute joints in addition to the slider at the robot-human interface. Gruebler's mobility criterion[17] suggests that this design would have three degrees of freedom. One statement of the mobility equation is

$$M = 6(n - j - 1) + \sum_{i=1}^{j} f_i \tag{3.8}$$

where $M$ is the mobility of the mechanism, $n$ is the number of links including ground, $j$ is the number of joints, and $f_i$ is the mobility provided by each joint $i$. Consider the closed chain mechanism formed by the robot and patient depicted in Fig. 3-19 with the human wrist approximated as a Cardan joint. This mechanism can be viewed as having nine links and nine single-degree-of-freedom joints, which according to Eq. 3.8 corresponds to three degrees of freedom. The initial design, however, only included two revolute joints at the handle. Constructing the device proposed in the sketch, in fact, would not allow for torque transmission in the PS axis. This situation was resolved, somewhat counter-intuitively, by removing another degree of freedom from

[17] Care must be taken in applying Gruebler's mobility criterion, as it does not consider mechanisms with unique geometric configurations. The E-quintet is a classic example of a paradox encountered in the use of this criterion [40]. This planar mechanism has one DOF when its links are parallel, though the Gruebler equation suggests it is a structure (DOF = 0).

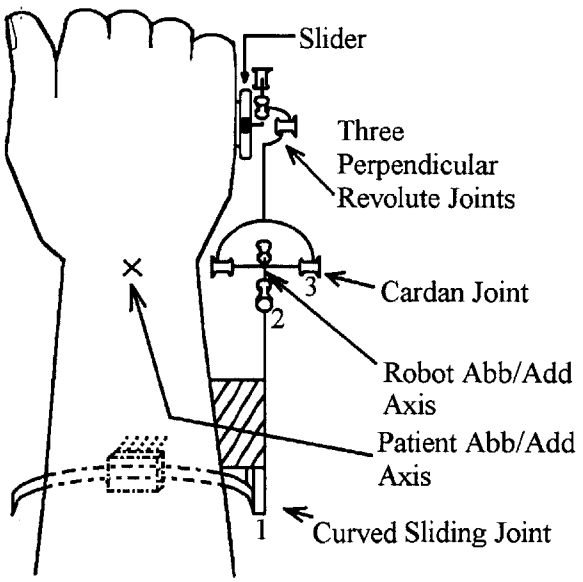


Figure 3-19: Original kinematic design [54].

the handle and adding a constraint to the patient positioning. By aligning the wrist flexion axis with the robot flexion axis, that mechanism appears as though it has one link. The modified abduction/adduction mechanism can now be viewed as a planar four bar linkage, so that the total mechanism is comprised of two orthogonal, planar, single-degree-of-freedom mechanisms. Figure 3-20 shows the underside of the modified handle connection; the handle was rendered immobile about its vertical axis by replacing by a bearing with a bushing and introducing a clamp that is bonded to the handle yoke using Liquid Steel® (a patch filler).

In order for this configuration to maintain its special geometry, the patient's flexion/extension must align with the robot. Joint compliance allows for some flexibility in this constraint, but modest excursions from this configuration will either bind the robot or prompt the patient to move his whole arm to continue motion. To assist the therapist in positioning the patient, a marker was placed where the wrist must go (Fig. 3-21). The analysis presented here depends on the accuracy of the model chosen for wrist kinematics, which are at best poorly quantified. Experience with the device shows that some abduction/adduction movements may be difficult when the wrist is flexed or extended, indicating that the model used in the analysis presented

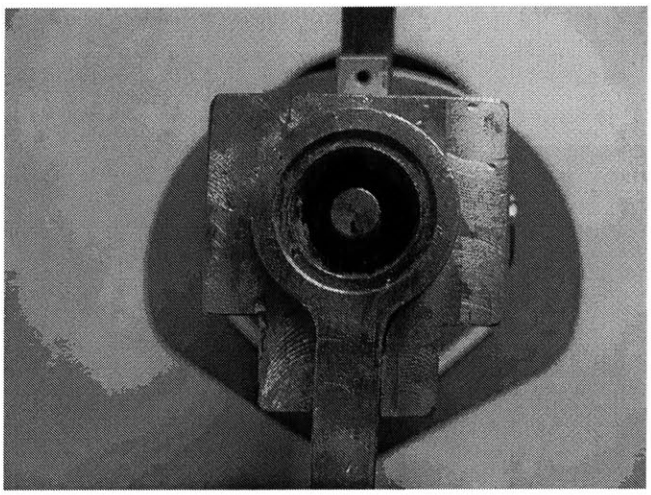

Figure 3-20: Modified handle connection including bushing and clamp.

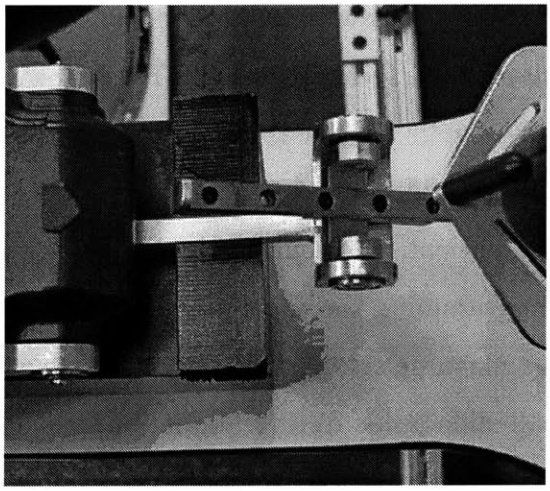

Figure 3-21: Robot reference points. The handle sits in the nest block. The marker on the transmission housing provides a guide for patient placement.

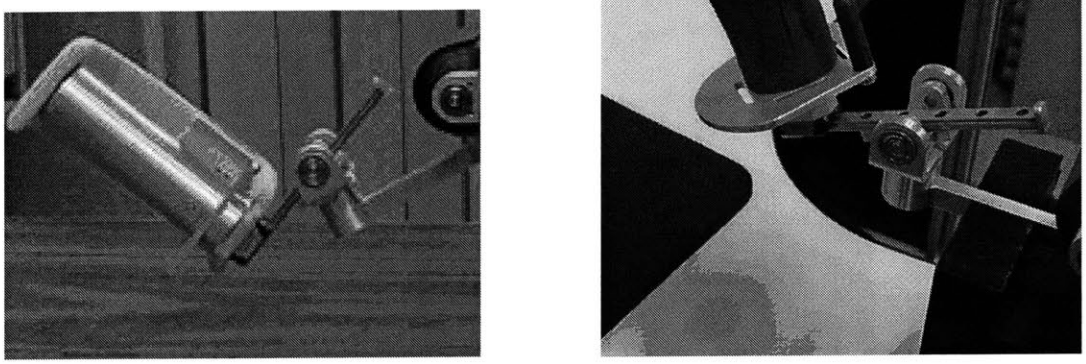

(a) Original handle.

(b) Modified handle by IMT.

Figure 3-22: Robot handle.

here may be inadequate. This issue warrants further study.

The initial handle included a cumbersome configuration procedure to adapt to the handedness of the patient. A new handle, specified at MIT, then designed and fabricated by Interactive Motion Technologies (IMT), is now in place on the robot, shown in Figs. 3-22. This handle weighs approximately three times as much as the original handle. Slots are provided at the top and bottom of the handle to allow the therapist to strap the patient in. Securing the hand of the patent to the handle is quite important, as programming the abduction/adduction axis to be stiffer than this connection would be meaningless. A loose grip will allow the handle to change its position along the ball slide guide during abduction/adduction movements. The method of attachment, shown in Fig. 3-23, ensures a good hand attachment when properly secured by the therapist, independent of the patient's own grip strength.

The original design called for an extra structural member on the transmission housing to secure the patient's forearm. This part not only contributed to the assembly required to change the machine from left to right handed, but tended to constrict

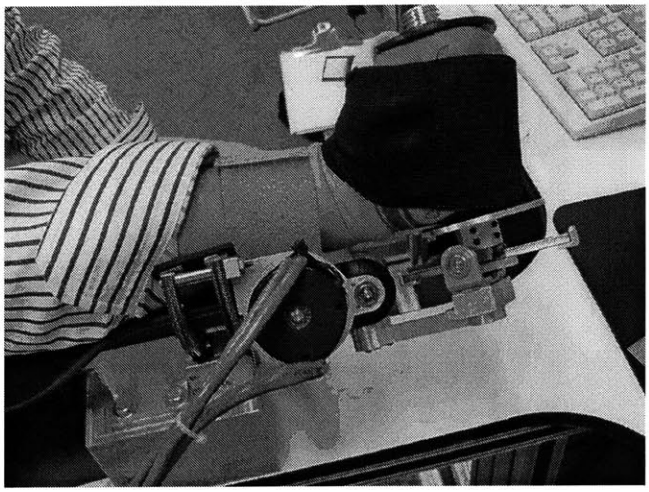

Figure 3-23: Hand attachment: The patient is secured to the robot by the therapist as shown, using straps at the wrist and hand. The wrist strap, seen above the ADR motor, is bolted to the transmission housing.

patient mobility. Because the patient PS axis and robot PS axis are separated and, likely, somewhat skewed, this protrusion will encourage wrist extension during supination[18]. To address this issue, the method of attachment for the distal forearm was changed to a Velcro® strap, also seen in Fig. 3-23, that is bolted to the transmission housing. This serves to isolate the wrist from the forearm during therapy; if the patient raises his forearm off of the robot[19], the robot can not administer therapy for radial and ulnar deviation[20].

The sizing of the ring gear for the PS axis was based on anthropometric data on the human wrist. The fact that the PS axes for the human and robot are displaced, however, was not considered. As a result, most patients[21] will not be able to take advantage of the robot's complete range of motion due to interference with the ring gears. This hardware constraint must be addressed in the redesign; the size of the ring gear must be chosen to accommodate the place on the forearm where the second

[18]Note that in a "neutral" position, the wrist is already slightly extended.

[19]Such a scenario is likely with stroke patients attempting to compensate for their disability.

[20]Again, the abduction/adduction mechanism relies on the flexion axis of the wrist coinciding with the flexion axis of the robot and the abduction axis of the wrist remaining a fixed distance from the differential axis.

[21]The degree of interference experienced by a patient will depend on his size.

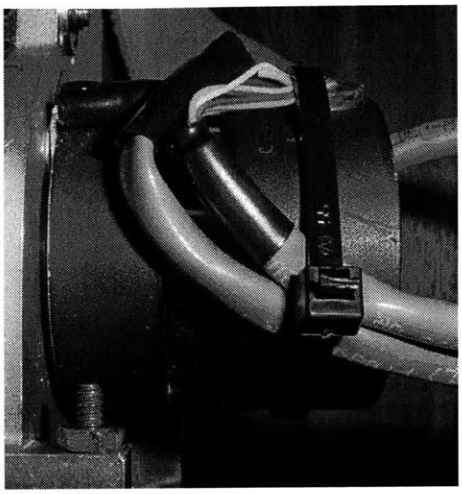

Figure 3-24: Strain relief on ADR and ADL motors.

ring gear will contact the patient. Rubber stops have been placed on the corners to prevent injury. Partially related to this sizing issue, the forearm support could not accommodate the entire patient population. This part was redesigned to flare out on the proximal side, yet still fit into the existing hardware, thus alleviating the discomfort of larger patients.

Another aspect affecting PS mobility is the cable routing from the actuators and sensors out to the electrical panel. The importance of preventing the encoders from being loaded has already been discussed. The encoder cables are strain-relieved on the actuators themselves to accomplish this task, as shown in Fig. 3-24. The bulky cables that connect the ADR and ADL components to the electrical panel, provided by Baker Electronics, restrict PS mobility. No method existed for routing the cables considering the fact that the ADR and ADL actuators are carried by the PS axis. The best solution found involved looping the cables around the back of the device, as seen in Fig. 3-25. This issue can be resolved in future designs by considering potential cable routing issues earlier in the design process.

Through specifications provided by a team of therapists at Burke (and coordinated here at the Newman Lab), a patient workstation was designed and fabricated (also by IMT). This workstation, currently installed at Burke, has the robot mounted in

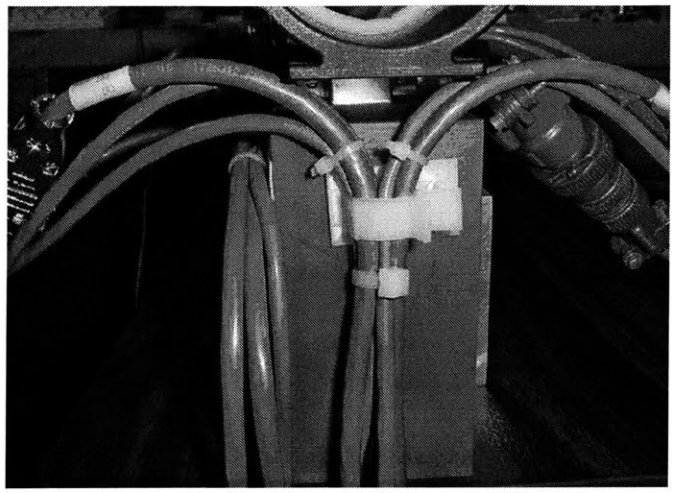

Figure 3-25: Cable routing to allow for PS mobility.

the center with and adjustable chair capable of being positioned on either side. A flat-panel LCD display, the source of visual feedback, can be adjusted in the patient's line of sight. Recall that PS motion is referenced to the plane of the arm, so that positioning the patient with 20° of shoulder abduction will change the meaning of robot data[22]. In the future, programs for pronation and supination will have to be tailored to for right-handed and left-handed patients to avoid over-rotating the forearm. The patient is seated at the device and secured at the hand and wrist, as mentioned, as well as at the bicep. The bicep attachment pivots to adjust for patient size and to accommodate shoulder abduction.

## 3.6 Computer Control

The servo-amplifiers are configured in `Analog Torque` mode so that voltages can be sent directly from the computer with a one-to-one correspondence to the desired torque levels. The computer is a Pentium III machine with a 1 GHz processor. The motherboard includes one ISA slot, necessary for the USDigital PC7266 encoder card. The counter card reads the already interpolated quadrature encoded encoder

[22]The encoder information recorded during therapy references the PS angle to the lab frame and includes no information regarding the orientation of the patient at the device.

signal, capable of input frequencies up to 1.75 MHz. This information is used by the controller software. The robot is provided with a nest block as seen in Fig. 3-21. This piece of Delrin® was machined as a stand to rest the robot on when not in use and as an aid for indexing the robot. In order for the encoders to be properly read by the computer software, they must be indexed. The nest block offers a convenient, repeatable reference position to move to for this purpose. The computer is running QNX version 4.24, a real-time operating system based on UNIX. Software, written in C++, oversees the robot operation, sending the desired actuator voltage to the UEI PD2-AO-8/16 digital-to-analog card. This card has 16-bit resolution over its range of $-10\,\mathrm{V}$ to $+10\,\mathrm{V}$.

Typical system operation occurs at sampling frequencies of 1 kHz[23]. During each sample period, the sensors are read, followed by calculation of the output vector based on these readings. A write function is then performed and its values are held until the next write occurs. Software timing studies on a similar system show the delay between "read" and "write" functions to be on the order of tens of microseconds [8]. All of the software is designed within an object-oriented library structure, internally known as the robot libraries, allowing for the integration of software and hardware. The wrist robot physical system consists of nine "states[24]": three angles, three velocities[25], and three commands. The libraries also allow access to monitor functions, providing for the development of video games for therapy. The video games for the wrist robot are presented in Chapter 7.

Figures 3-26 show the final packaged electrical panel that houses the majority of the electronics. Cables from the actuators and sensors run through this panel to an intermediate breakout box, then to the computer. The panel includes such features as isolation transformers and emergency stop buttons. It also includes a Programmable Logic Controller (PLC) that continuously monitors the functionality of the servo-amplifiers. Should one of the servo-amplifiers fail in a detectable manner, the other

[23]Some experiments, identified when relevant, were sampled at 2 kHz.

[24]These are not necessarily system states, but any variable recorded by the computer during an experiment. Henceforth, these will be referred to as robot states.

[25]A filtered back difference of the position signal. See Appendix B for more detail.

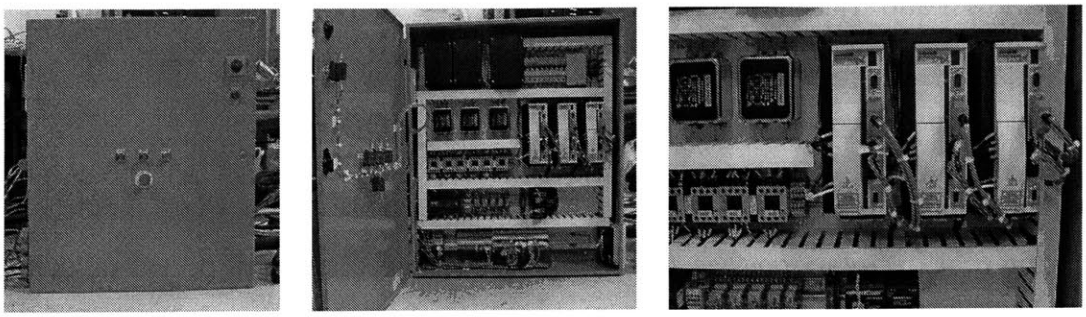

(a) Panel exterior (b) Panel interior (c) Servo-amplifiers

Figure 3-26: Wrist robot electrical panel manufactured by Baker Electronics.

two servo-amplifiers will be shut down automatically.

## 3.7 Conclusions

An overview of the wrist robot hardware, both as designed and as modified, has been presented here. The design choices made naturally affect the performance of the robot. For the remainder of this thesis, the hardware will be analyzed "as-is." Modifications were made within the structure of the initial design. The remaining issues should be solved in the next version of the device by adjusting the earlier design choices based on how the current choices have propagated to performance and functionality. The task now is to quantify the performance capabilities of the device and prepare it for clinical use. The key points from this chapter are summarized as follows:

- During redesign, anthropometric data must be applied to resolve conflicts with sizing and mobility.
- The motor-encoder components chosen for this design do not provide a robust actuating system; future designs should consider an integral motor-encoder package.
- Motor locating problems, caused by the use of thru-holes, adversely affect the entire transmission.

- Backlash and friction-like phenomena are the main obstacles to smooth, stable operation[26]. These issues can be addressed at the design level through careful gear train configuration and the use of quality components.

- It is important to consider shaft stiffness in response to the loads incurred by gear tooth interactions, as (unwanted) shaft deflections are prevalent in this design.

- Further study is required to resolve the inconsistencies between the expected and actual behavior of the handle kinematics.

- Securing the patient at the wrist, hand, and upper-arm is critical for patient mobility and robot effectiveness.

- Patient posture affects patient mobility as viewed by the robot.

- Cable routing must be revised to prevent some of the problems seen with this device.

[26]This will become more clear throughout the characterization of the device.

# Chapter 4

# Component Characterization

The purpose of the following exercises is to identify the underlying physical phenomena that affect the overall system behavior. A schematic of the system operation is presented in Fig. 4-1 along with the thesis sections in which some of the subsystems are addressed. System operation, as discussed in Chapter 3, relies on encoder feedback as a controller input. The patient interacts with the hardware (denoted by the double arrow) while receiving visual feedback. Examining the operation of the subsystems will aid in the development of an overall system model.

## 4.1 Amplifier Characterization

The torque produced by a given actuator is proportional to the magnitude of the current through its windings. With three phase current generation, conveniently represented in the phasor diagram of Fig. 4-2, current is distributed to the windings as a function of electrical position. Equations 4.1 show the relationship between the currents in each phase.

$$I_A = I\cos\alpha \tag{4.1a}$$

$$I_B = I\cos\left(\alpha + \frac{2}{3}\pi\right) \tag{4.1b}$$

$$I_C = I\cos\left(\alpha + \frac{4}{3}\pi\right) \tag{4.1c}$$

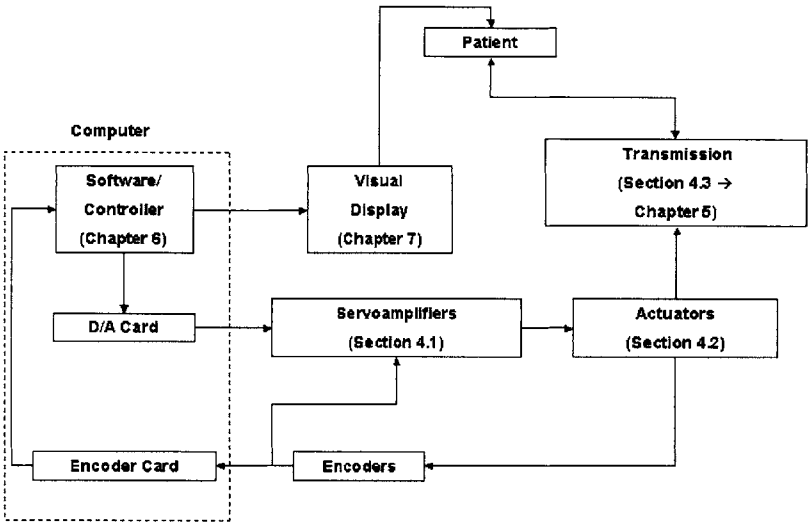


Figure 4-1: System block diagram. The patient interacts with the physical system while receiving visual feedback.

where $I$ is the command current magnitude, $\alpha$ is the electrical position of the rotor which is shown graphically as the angle between the real axis and phase A, and $I_A$, $I_B$, and $I_C$ are the currents in each of the phases. Because these motors have three pole pairs, each mechanical revolution corresponds to three electrical revolutions. For a given position, such as the one shown in Fig. 4-2, changing the command will result in a scaling of the diagram; the command current is represented by the radius of the circle and the current in any one phase for a position $\alpha$ is given by the projection of the corresponding phasor onto the real axis. By measuring any two of the three phases, the system of equations 4.1 can be solved for the command current as in Eqs. 4.2. A custom three-phase current sensor, detailed in Appendix A, was built for this purpose, allowing characterization of the amplifiers. It consists of three identical circuits, with each circuit consisting of a two-pole Butterworth filter with a cutoff frequency of 928.2 Hz. Each phase current is read by measuring the voltage across a $0.1\,\Omega$ resistor. The third current is a redundant measurement, but could be used as a parity check, as the three currents should always sum to zero. Characterizing

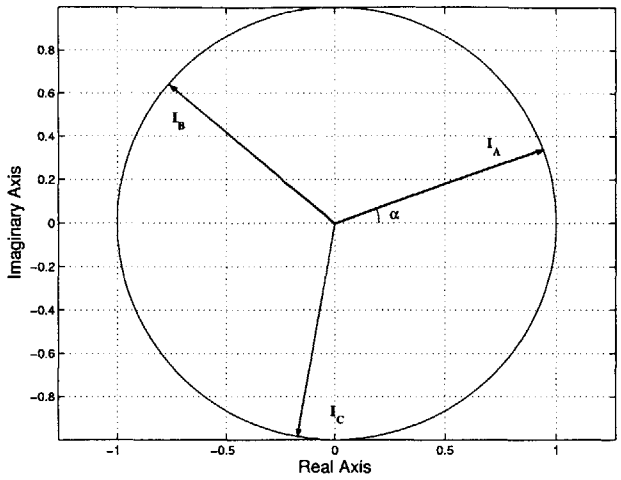


Figure 4-2: Phasor representation of three phase current. The magnitude of the current is $I$, the radius of the circle. At this instant, $\alpha = 20\,°$, so that the current in each phase is given by the real component of its corresponding phasor.

the current sensor in both discrete and continuous time[1] allowed determination of the gains for each stage, given in Table 4.1, and showed that the sensor effectively exhibits no dynamics in the frequency range of interest for characterization of the amplifiers.

$$\alpha = \arctan \frac{I_A \cos\left(\frac{4}{3}\pi\right) - I_C}{I_A \sin\left(\frac{4}{3}\pi\right)} \tag{4.2a}$$

$$I = \frac{I_A}{\cos \alpha} \tag{4.2b}$$

| Phase | Sensor Gain $[\frac{V}{A}]$ |
|---|---|
| A | 0.461 |
| B | 0.438 |
| C | 0.433 |

Table 4.1: Current sensor gains.

Kollmorgen amplifier configuration programs include an option for setting the

[1]Testing through the real-time operating system is in discrete time. Tests in this chapter were sampled at 2 kHz. It is also digital in nature due to the use of the D/A and A/D on the UEI multifunction data acquisition board. Approximations of continuous time measurements were obtained using a LeCroy oscilloscope with bandwidth of 200 MHz.

scaling factor between input voltage and output current magnitude. The Kollmorgen variable, ISCALE is set to 180 for the PS motor and to 240 for the ADR and ADL motors. The relationship between the input voltage and the output current is

$$\frac{I}{V_{com}} = \frac{\text{ISCALE}}{1000} \frac{18\,\text{Arms}}{10\,\text{V}} \tag{4.3}$$

where $V_{com}$ is the command voltage sent from the D/A board to the servo-amplifier. The listed values for ISCALE were chosen in part as a safety feature against exceeding the continuous current limit for the motors in question, since the D/A has a maximum output of 10 V. The usefulness of Eq. 4.3 can be verified by examining the amplifier response to different voltages.

Figure 4-3 shows the test setup for locked rotor testing of the PS actuator. In this setup, the motor shaft is coupled directly to the +z-axis of an ATI 16-bit, 6-axis force transducer[2] through an Oldham coupling and custom force transducer adapter. The tests should be considered quasi-locked rotor, as encoder measurements show up to 2 ° of movement during each test. Testing with the ADR and ADL motors proved more difficult. The front-mounted encoders obscured the shaft end, requiring a more indirect calibration method, as seen in the photographs of the test setup in Figs. 4-4. The encoder was held in place using a spring steel compliant mount similar to the ones introduced in section 3.3. Torque was transmitted from the motor to the force transducer using the same gearset from the actual robot transmission. The rotor is only quasi-locked in these tests as well, stemming partially from the deformation of the transducer gear shaft, but mostly from the backlash between the gears.

Quasi-static tests were conducted using the setups described above by inputting a low frequency sinusoidal voltage to the amplifier (using the computer). Figures 4-5 show the response of the amplifiers to a sine wave swept at 0.05 Hz along with the linear expected responses. The plot of the PS amplifier response shows good

[2]Note that all tests involving the force transducer were performed on a computer with an 800 MHz Pentium III processor rather than the computer described in section 3.6. This motherboard had two ISA slots and was therefore capable of supporting both the ATI force transducer and the USDigital encoder card.

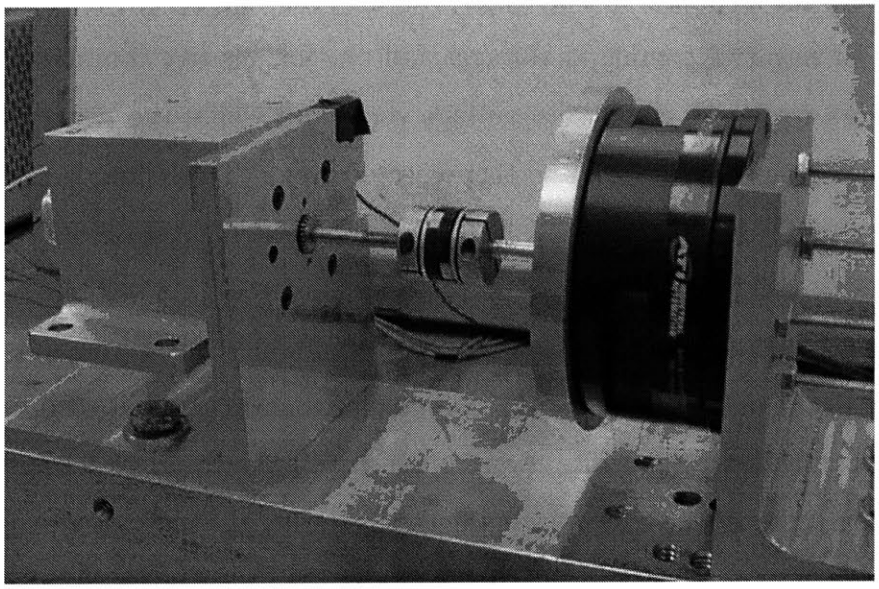

Figure 4-3: Test setup for PS motor calibration.

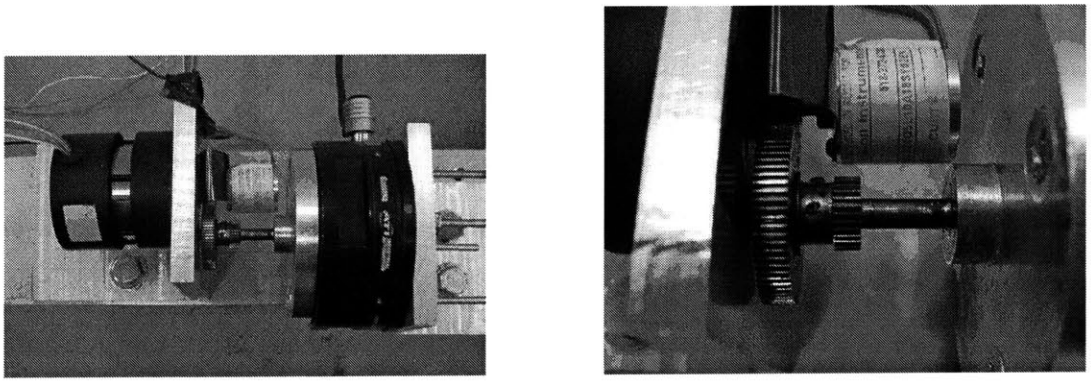

(a) Overview.

(b) Close-up of test setup.

Figure 4-4: Test setup for ADL/ADR motor calibration.

agreement within the capabilities of the current sensor. The ADR/ADL amplifiers also show large scale agreement with the expected trend, though there are some irregularities in the response; in Fig. 4-5(b), the response appears to have two distinct slopes (one for negative command voltages and one for positive command voltages). There is also a region in about zero voltage command where the response switches back and forth from zero amperes to the expected value. This effect is attributed to poor encoder performance during the test. Approximate measurements of the rotor speed for constant voltages (using the amplifier's onboard digital tachometer) showed as much as a 30% difference in velocities for positive and negative commands when the encoder was not secured properly. The compliant mounting described in section 3.3 was designed to address this concern and qualitatively appeared to behave properly. However, it easily could have been jarred between testing the mounting and installing the force transducer into the setup. The results of Fig. 4-5(b), therefore, should not be attributed to amplifier performance, but to encoder malfunction.

Frequency response testing of the amplifier allows determination of the influence of amplifier dynamics on the overall system. A "brute force" approach was taken in obtaining this information, as each frequency was tested separately. Forty frequencies, equally spaced on a logarithmic scale, were input to the amplifier. The response for each test was measured and fit to a function of the form

$$I(t) = I\,sin(\omega\,t + \phi) \tag{4.4}$$

where $I$ is the amplitude and $\phi$ is the phase of the output. Figure 4-6 shows the resulting Bode plot with amplitudes normalized to the DC gain found in the static testing. This data was taken with the LeCroy oscilloscope and the input was generated by a function generator, so it is considered effectively continuous. The model, after subtracting the effects of the currents sensor, shows that the amplifier behaves like a first order filter. Although these tests are to characterize the amplifier response, the amplifier is still loaded by the motor. Since the amplifier is not expected to have such a low bandwidth, it is likely that this first-order behavior is a result of the motor time

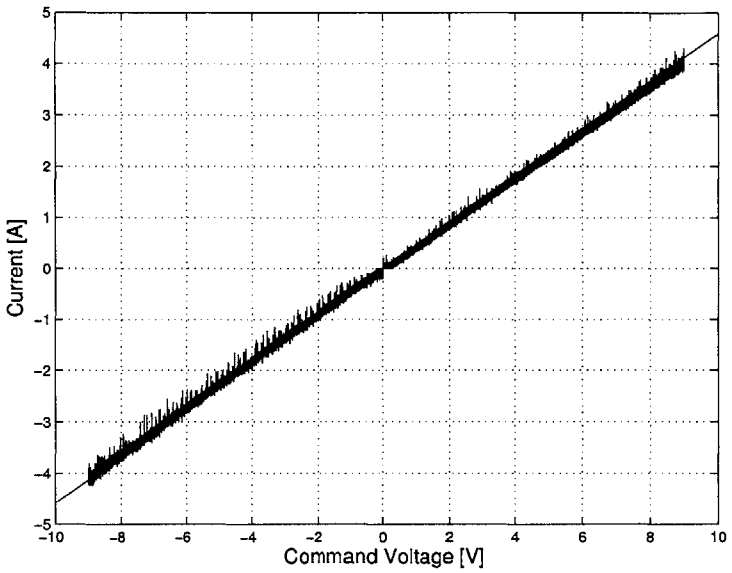


(a) PS amplifier response, ISCALE = 180.

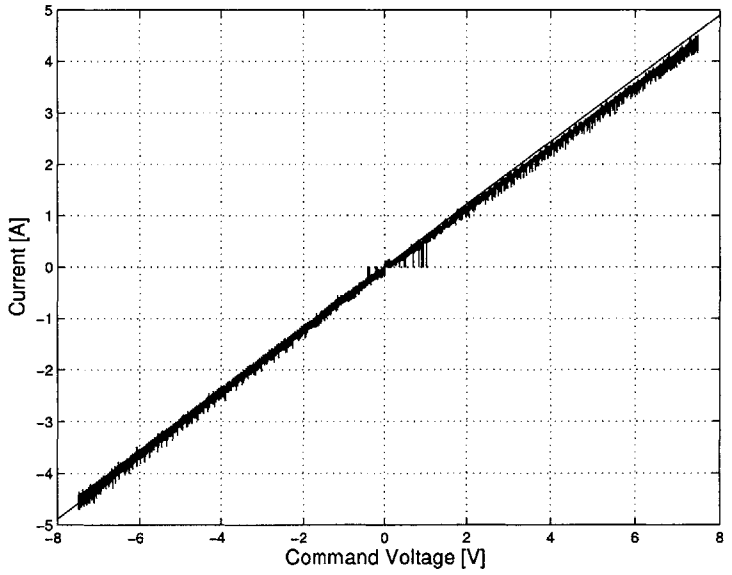


(b) ADR/ADL amplifier response, ISCALE = 240. Irregularity in response attributable to the effects of the test setup on encoder operation.

Figure 4-5: Servo-amplifier response to slow sinusoidal input (0.05 Hz) with expected (linear) response.

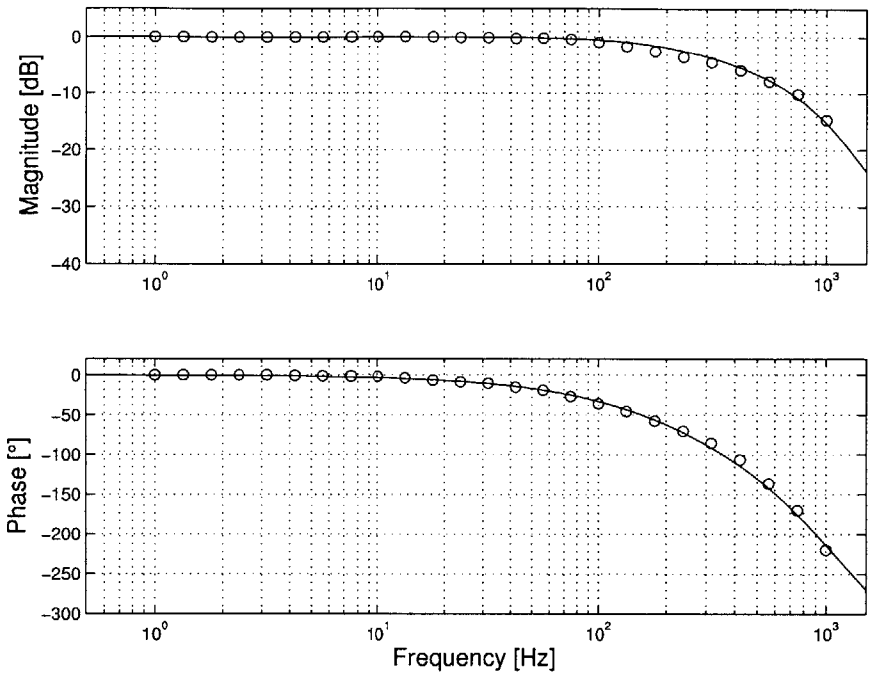


Figure 4-6: Amplifier frequency response in continuous time with fitted model. Magnitude plot shows measured current over 0 Hz current.

constant, $\tau$, given by

$$\tau = L/R \tag{4.5}$$

where $L$ is the inductance of the windings (0.54 mH for the PS motor) and $R$ is the resistance of the windings (0.933 $\Omega$ for the PS motor). The published values for these motor parameters place the cutoff frequency at 275 Hz. The data of Fig. 4-6 is plotted with a fitted model using a corner frequency of 275 Hz plus 120 $\mu$s of pure time delay. A pure delay will not affect the magnitude of the response, but will affect the phase lag according to Eq. 4.6:

$$\phi = T\,\omega \tag{4.6}$$

where $\phi$ is the phase lag, $T$ is the time delay, and $\omega$ is the frequency.

Tests were also conducted in discrete time using input and output from the computer. Figure 4-7 shows this data, sampled at 2 kHz, along with the discretized version of the model from Fig. 4-6. Notice the increase in magnitude roll-off as

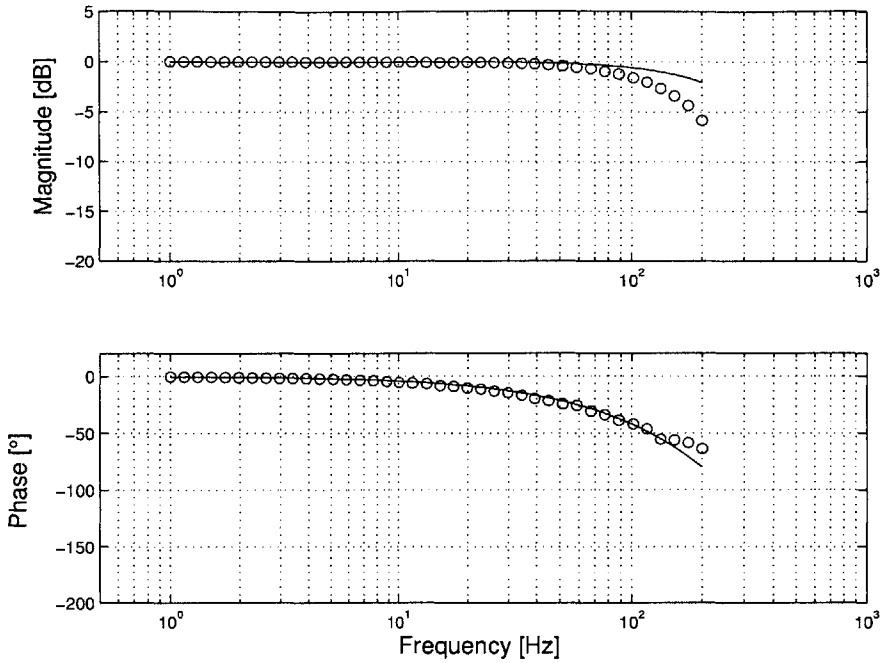


Figure 4-7: Amplifier frequency response in discrete time with fitted model. Magnitude plot shows measured current over 0 Hz current.

compared to what is predicted by the model. This is a direct result of the fitting method, MATLAB's `fminsearch`, which is attempting to minimize a cost function related to the sum-of-squares error. Higher frequency testing shows nonlinearities in the amplifier response, especially where the current switches signs. As these nonlinearities become more prevalent, they drag the amplitude of the fit down. This effect is shown in the progression of plots in Figs. 4-8. As the input frequency increases, the ratio of the magnitude of the fit to the peak response of the current[3] during the test decreases. The degradation of amplifier response at modest frequencies is a cause for concern, but the performance in the frequency range of interest for this application is acceptable.

[3]The peak response of the current was recorded as the magnitude of the response during continuous-time testing with the oscilloscope.

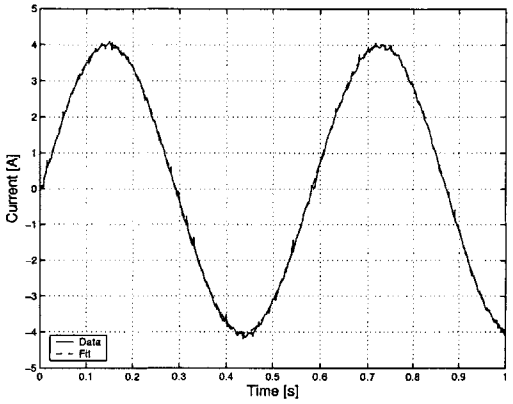


(a) Input frequency = 1.72 Hz.

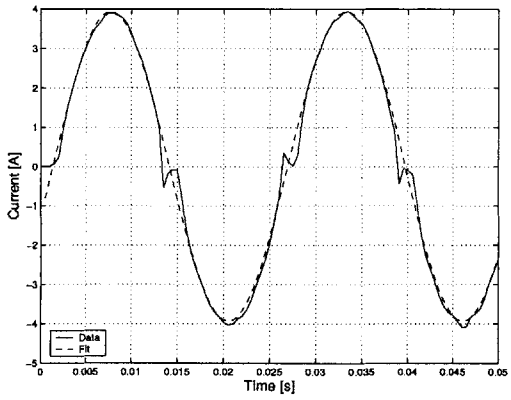


(b) Input frequency = 39.2 Hz.

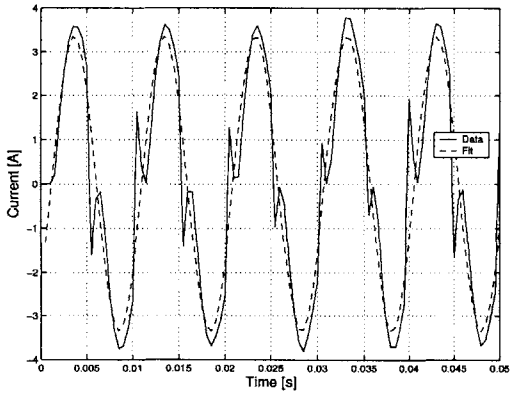


(c) Input frequency = 101.4 Hz

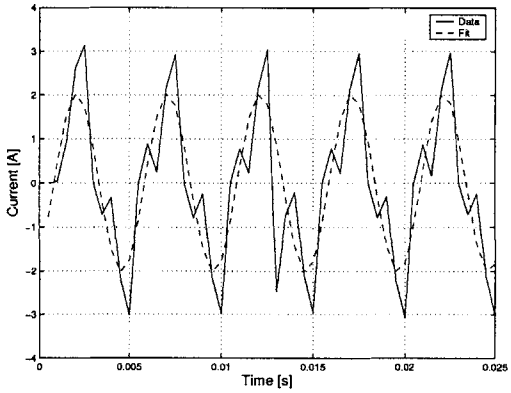


(d) Input frequency = 200 Hz.

Figure 4-8: Progression of amplifier frequency response fits. Each plot shows the response as measured by the current sensor at a given input frequency along with the fitted response calculated by `fminsearch`. Notice that the ratio of the fit magnitude to the measured peak current decreases with increasing frequency.

## 4.2 Motor Characterization

With the amplifiers characteristics modeled, the actuators can be characterized. The parameters of interest here include the torque constant of the motors, the extent to which torque pulsation affects the performance of the motors, and the actuator bandwidth. Locked-rotor actuator testing is executed with the same setups described in the previous section. For the purposes of data analysis, the compliance of the overall coupling between the actuator and sensor is not considered and the force transducer is known to have a first order roll-off at 235 Hz. This allows a model of the amplifier-actuator package to be developed, providing a transfer function from input command voltage to developed actuator torque. Free-rotor actuator behavior is also briefly investigated to determine some friction characteristics.

### 4.2.1 Static Motor Testing

Brushless servomotors, much like DC torquers, produce torque through the interaction between permanent magnetic fields and current-induced magnetic fields. These generally follow the equation

$$\tau = K_t I \tag{4.7}$$

where $\tau$ is the torque developed in the actuator and $K_t$ is the torque constant of the motor. This value was determined by inputting a slow (0.05 Hz) sinusoidal voltage to the amplifier in order to get a quasi-static response. The resulting torque versus current curve for the PS motor, shown in Fig. 4-9, has a slope of $0.0311 \frac{\text{Nm}}{\text{A}}$. Compare this with the published value of $0.0367 \frac{\text{Nm}}{\text{A}}$, also represented in the figure. Similarly, the ADL and ADR motors have a measured torque constant of $0.0169 \frac{\text{Nm}}{\text{A}}$ compared with the published value of $0.0254 \frac{\text{Nm}}{\text{A}}$. Note that since the current is directly proportional to voltage, these values can be recast: the torque constant for the PS motor is $0.0143 \frac{\text{Nm}}{\text{V}}$ and the torque constant for the ADR and ADL motors is $0.0103 \frac{\text{Nm}}{\text{V}}$.

Referring to this value as the torque "constant" of the motor is a bit of a misnomer. The characteristics of the interaction between the magnetic fields of the rotor and windings in the stator depends on the orientation of the rotor with respect to the

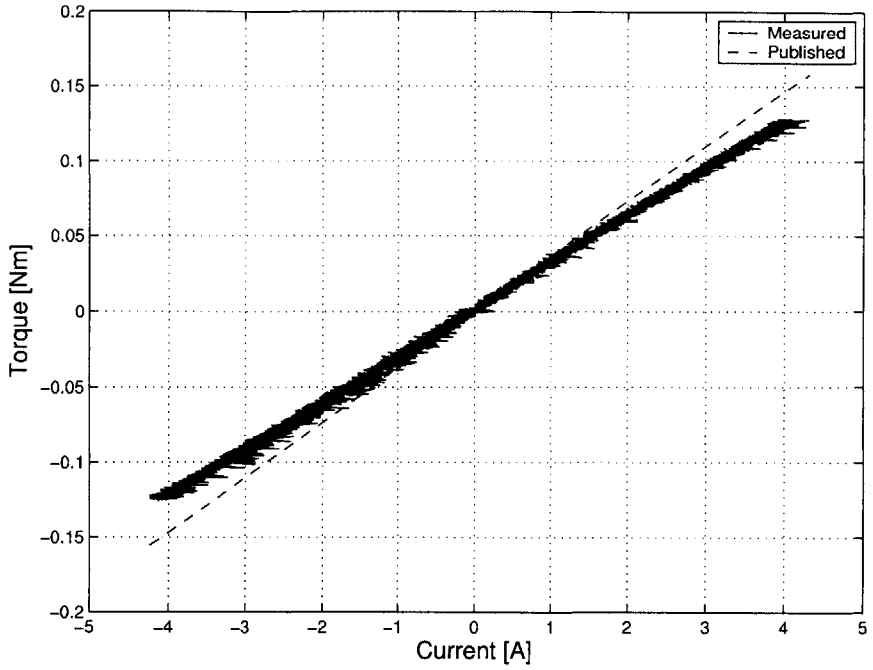


Figure 4-9: PS static torque taken at rotor position of 0 ° plotted with expected data.

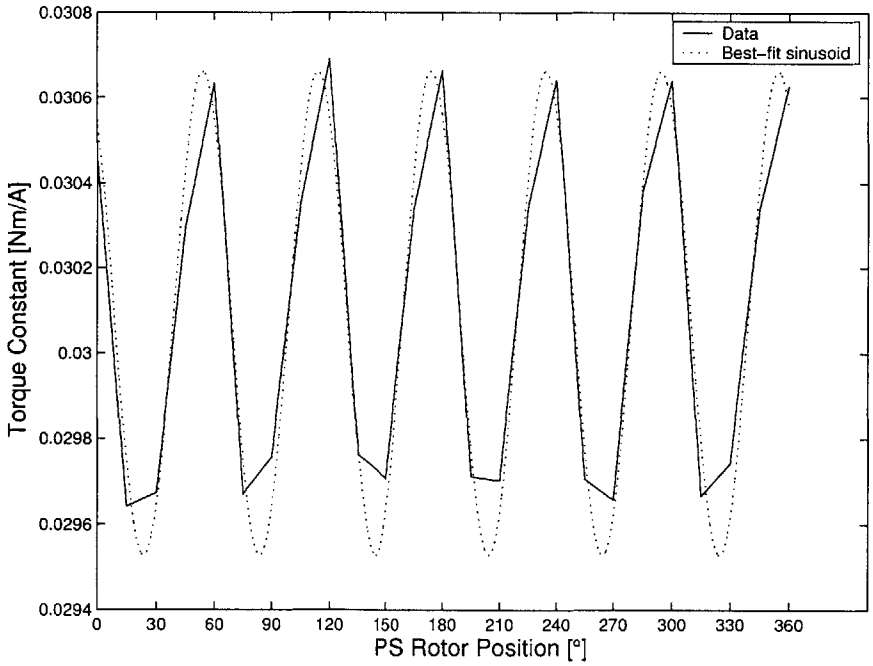


Figure 4-10: PS Torque ripple. Torque constants are calculated by fitting a line to the measured torque versus measured current profiles at each position shown.

stator. This fact results in a torque pulsation phenomenon known as torque ripple, introduced in section 3.2, in which the value of the torque constant is a strong function of the position of the rotor. The test to determine the motor constant described above was repeated at 15 ° intervals rotor positions indicated by the encoder. The resulting torque constant from each test is plotted in Fig. 4-10 along with the best fit sinusoid to the data. The 6-pole motor shows 6 periods per revolution, with the torque constant of the motor remaining within $\pm 2\%$ of its average value of 0.0301 $\frac{\text{Nm}}{A}$.

### 4.2.2 Motor Friction and Cogging

Besides torque ripple, the other component of torque pulsation that is of interest here is cogging, a current independent phenomenon in which the rotor seeks certain preferred positions (see section 3.2). Cogging is easily observed by rotating the rotor by hand, feeling each preferred position. In order to determine the magnitude of the cogging, an open loop voltage command was sent to each actuator while the rotor was allowed to spin freely. Once at steady state, a braking torque was applied to the rotor by hand. When the actuator came to rest, the rotor was released. If the command torque was greater than the cogging torque plus static friction, it would begin to move again[4]. This procedure was repeated for different input command voltages to find the maximum voltage at which the rotor, after being stopped by hand, would not start moving again. Table 4.2 is a report of these results, scaling the voltage command according to the identification of the motor constants in section 4.2.1. These tests, along with the remaining tests in this chapter, provide only indirect evidence of cogging. The motor cogging could have been easily characterized by coupling a torque transducer to the motor and rotating it by hand. This would provide an accurate map of the effects of motor cogging and friction as a function of position without resorting to scaling motor commands. Such a methodology could be explored in the future with actuators that have not yet been mounted into their intended assemblies.

Friction, of course, takes many forms, as mentioned in Chapter 3. Figure 4-11

[4]This test is not able to distinguish between the effects of cogging and static friction.

| Motor | Static Friction Plus Cogging Torque [Nm] | |
|---|---|---|
| | Positive | Negative |
| ADR | $2.9 \cdot 10^{-3}$ | $2.5 \cdot 10^{-3}$ |
| ADL | $2.9 \cdot 10^{-3}$ | $2.8 \cdot 10^{-3}$ |
| PS | $5.4 \cdot 10^{-3}$ | $3.9 \cdot 10^{-3}$ |

Table 4.2: Motor starting torques. These values represent the scaled command voltages necessary to start the freely rotating actuator from rest.

shows a general interaction between contacting bodies, known as a Stribeck curve. It is shown in terms of forces, but is applicable to frictional torques as well. There are four basic regions of the curve. The region labelled "sticking" on the graph, also known as stiction or pre-sliding, is the region where the friction force is able to prevent any motion. Once the maximum static friction is broken, there is typically some velocity-independent friction region resulting from solid-on-solid contact. Higher speeds at the interface can allow lubrication to flow between the contacting surfaces, leading to a viscous friction model. To get an idea of the dynamic friction present in the motors themselves, some simple tests were conducted. In these tests, a constant velocity was requested of each motor at a number of different speeds. The actual velocity, of course, was not constant due to the torque pulsation phenomena present in the actuation system. PD control cannot adequately compensate for such effects, evident in Figs. 4-12. For the purpose of analyzing the data, average values of the command torque[5] and velocity, assumed to be operating at steady state, are plotted, showing the general trend. The results, shown in Figs. 4-13, indicate that the motor friction has some Coulomb component as well as some viscous component. Notice that the static friction levels given in Table 4.2 are higher than the friction torque axis intercepts in each scenario. Boundary lubrication regimes are difficult to characterize. Still, the idea that the static friction is higher than the kinetic friction is consistent with qualitative tribology.

[5]A scaled version of the command voltage.

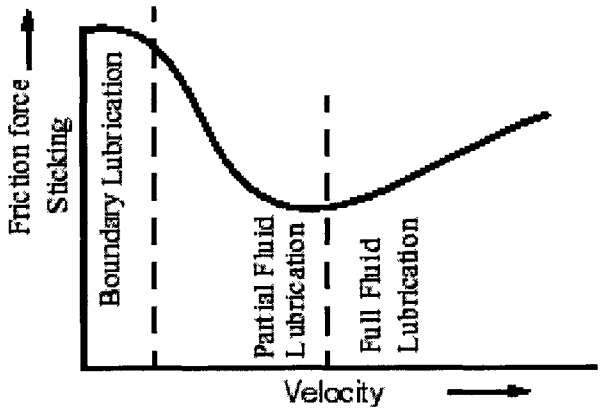


Figure 4-11: General friction versus velocity characteristics [34].

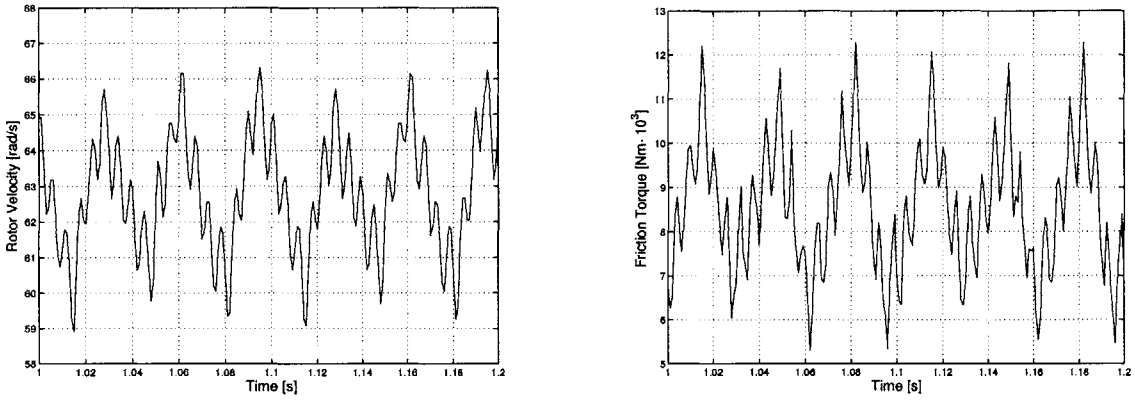


(a) Velocity response

(b) Command torque

Figure 4-12: PS motor response in typical dynamic friction test. In order to highlight the response, the axes are not zeroed.

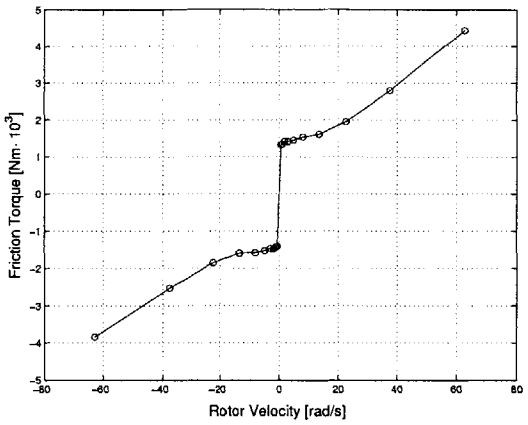


(a) ADR

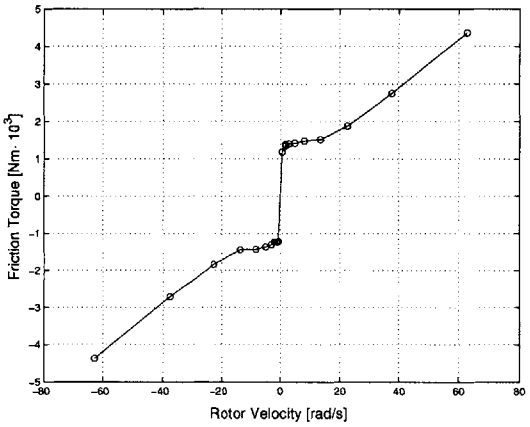


(b) ADL

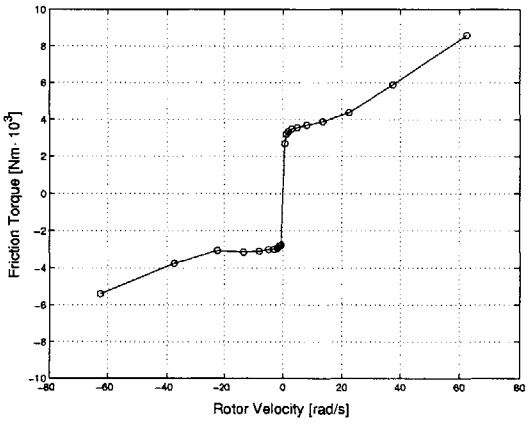


(c) PS

Figure 4-13: Dynamic friction testing for each motor.

### 4.2.3 Frequency Response

Motor frequency response data is taken for reasons similar to those given for the amplifier characterization. The procedure is also quite similar, though the results presented here are only for discrete time. Using the previously developed amplifier model, Fig. 4-14 shows that an additional delay of 30 $\mu$s fits the data well. To recap, the model includes a first-order behavior with a cutoff frequency at 275 Hz attributed to the motor, first-order behavior with a cutoff frequency at 235 Hz from the force transducer, the two-pole Butterworth filter behavior of the current sensor, and a total of 150 $\mu$s of pure time delay. The bulk of the time delay is attributed to the amplifier with the additional 30 $\mu$s due to software computation delays[6]. The testing here is inconclusive as to the origin of the delays or even of the first-order behavior. Still the knowledge of the characteristics of the amplifier-actuator package is useful. Data from the ADL and ADR motors are much more difficult to interpret. The test setup, introduced in Figs. 4-4, is prone to backlash. In addition, the interaction of gear teeth produces forces that tend to separate the gears. These produce nonlinearities in the response which are not amenable to the linear analysis techniques used in finding the PS frequency response. Despite this difficulty to attach meaning to the actuator performance at high frequencies, the data does suggest that the actuator performs well in the desired frequency range. This assumption is further strengthened by the fact that the PS motor behaved as a pure delay with no additional dynamics for the locked-rotor test. The first-order filter behavior has been attributed to the servo-amplifier; all of the actuators are commutated by identical servo-amplifiers.

## 4.3 Transmission Elements

Limited testing with the first gear stage verified that the rotors could spin freely. Step tests for a single gain and for two different amplitudes of pinion rotation were conducted with each motor. The PS motor was tested with gain $k = 0.020 \frac{\text{Nm}}{\text{rad}}$, while

[6]Recall that the 120 $\mu$s of delay found in section 4.1 was from tests with the function generator and oscilloscope.

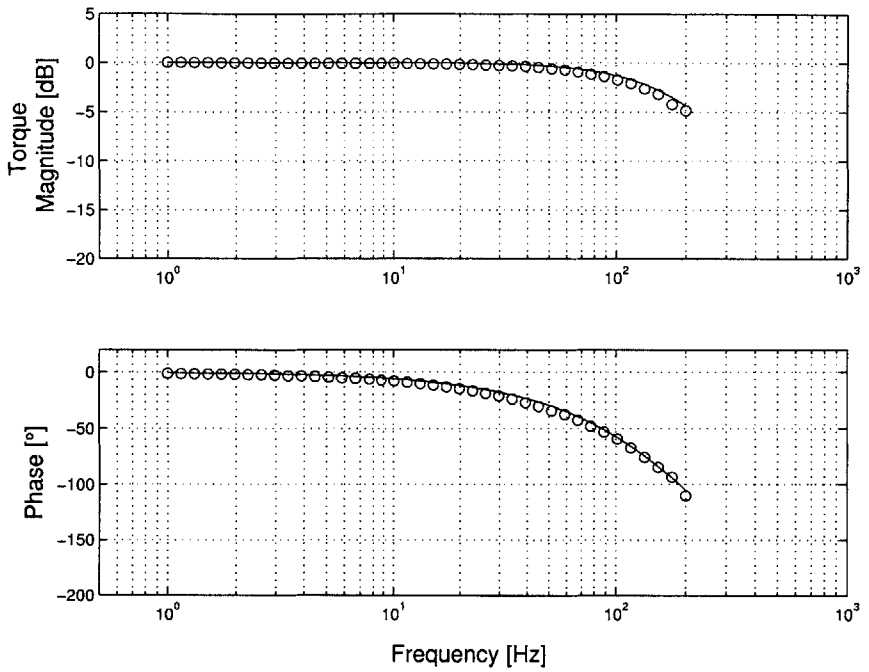


Figure 4-14: PS actuator frequency response with fitted model.

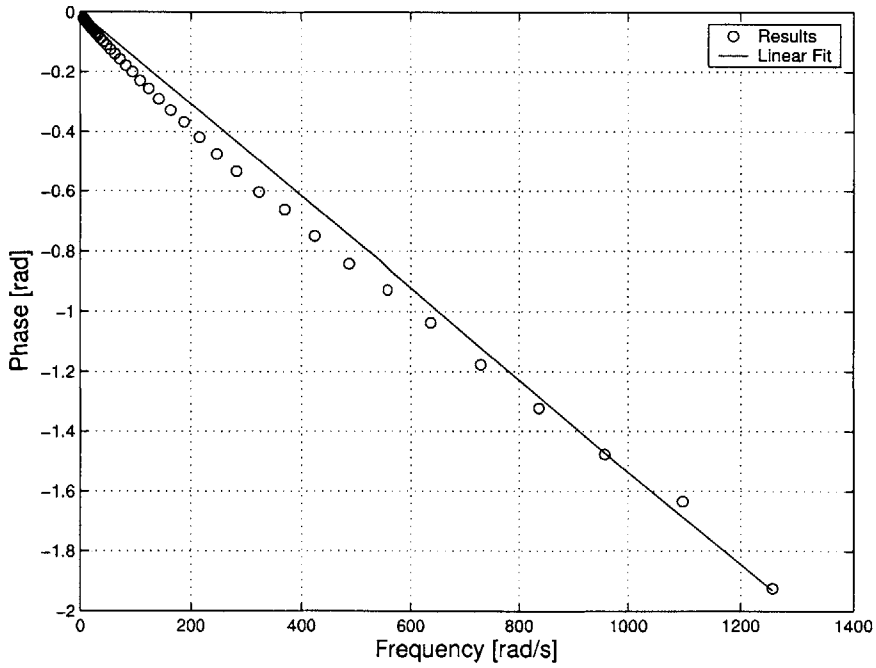


Figure 4-15: PS actuator frequency response, phase versus frequency.

the ADR and ADL motors, attached to their respective first gear stages, were tested with a gain of $k = 0.015 \frac{\text{Nm}}{\text{rad}}$. The desired position was stepped from $0\,^\circ$ up to the desired value (either $50\,^\circ$ or $100\,^\circ$ of pinion rotation, depending on the test), back to $0\,^\circ$, down to the negative of the desired value, and then back to $0\,^\circ$ to end the test. Each test was repeated five times. The typical response, as seen in Fig. 4-16, is an oscillation about the equilibrium point. Some steady state error is inevitable due to the presence of static friction. Table 4.3 summarizes the torque values when the rotor has stopped. These values, as expected, are lower than those listed in Table 4.2, since they are not measures of the maximum static friction.

| **Element** | **Average Static Friction [Nm]** |
|---|---|
| ADR + Intermediate Gear Stage | $0.6 \cdot 10^{-3}$ |
| ADL + Intermediate Gear Stage | $0.7 \cdot 10^{-3}$ |
| PS | $0.7 \cdot 10^{-3}$ |

Table 4.3: Steady state error from first stage step response tests.

The step response also provides a measure of the rotary inertia, as determined by the measured frequency of oscillations, and the relative contributions of Coulomb and viscous friction, evidenced by the nature of the decay envelope. These components are identified using a method developed by Liang and Feeny [35] that computes the decrement. Note that the frequency content of the response is unaffected by Coulomb damping, while viscously damped vibrations undergo oscillations at some damped frequency, $\omega_d$, given by

$$\omega_d = \omega_n \sqrt{1 - \zeta^2} \tag{4.8}$$

where $\omega_n$ is the natural frequency of the system and $\zeta$ is the damping ratio: the ratio of the damping constant to the critical damping constant. In the response, the nonlinear Coulomb friction will cause a linear decay envelope, while the viscous friction will cause an exponentially decaying envelope. The method is based on a recursive relation for the peaks and valleys of the oscillations:

$$\Theta_i = -e^{-\beta\pi}\Theta_{i-1} + (-1)^{i-1}(e^{-\beta\pi} + 1)\theta_k \quad , \quad i = 1, 2, \ldots, n \tag{4.9}$$

where $\Theta_i$ is the magnitude of the response at peak (or valley) $i$, $\beta = \zeta/\sqrt{1-\zeta^2}$, and $\theta_k = \tau_k/k$ with $\tau_k$ as the Coulomb friction torque level and $k$ as the programmed stiffness of the actuator. This comes from the differential equation of motion for free vibrations of this system,

$$\ddot{\theta}(t) + 2\zeta\,\omega_n\,\dot{\theta}(t) + \omega_n^2\,\theta(t) = \begin{cases} -\omega_n^2\theta_k, & \dot{\theta}(t) > 0 \\ \omega_n^2\theta_k, & \dot{\theta}(t) < 0 \end{cases} \tag{4.10}$$

A logarithmic decrement can be defined to isolate the viscous effects as follows

$$\ln\left(-\frac{\Theta_i + \Theta_{i+1}}{\Theta_{i-1} + \Theta_i}\right) = -\beta\pi \tag{4.11}$$

The frequency, $\omega_n$, then relates to the rotary inertia as seen at the motor by Eq. 4.12. The results of this analysis are summarized in Tables 4.4 and 4.5.

$$J = \frac{k}{{\omega_n}^2} \tag{4.12}$$

| **Element** | $\omega_d$ $[\frac{\text{rad}}{\text{s}}]$ | $\beta$ | $\zeta$ | $\theta_k$ [rad] | $\omega_n$ $[\frac{\text{rad}}{\text{s}}]$ |
|---|---|---|---|---|---|
| ADR + IGS | 96.7 | 0.163 | 0.161 | 0.15 | 98.0 |
| ADL + IGS | 95.2 | 0.111 | 0.111 | 0.06 | 95.8 |
| PS | 96.7 | 0.181 | 0.178 | 0.21 | 98.3 |

Table 4.4: Step response characteristics.

| **Element** | **Inertia** $[\text{kg} \cdot \text{m}^2]$ | **Viscous Friction Coefficient** $[\frac{\text{Nm s}}{\text{rad}}]$ | **Kinetic Friction** [Nm] |
|---|---|---|---|
| ADR + IGS | $1.54 \cdot 10^{-6}$ | $50.7 \cdot 10^{-6}$ | $0.225 \cdot 10^{-3}$ |
| ADL + IGS | $1.61 \cdot 10^{-6}$ | $35.3 \cdot 10^{-6}$ | $0.9 \cdot 10^{-3}$ |
| PS | $2.05 \cdot 10^{-6}$ | $74.8 \cdot 10^{-6}$ | $4.2 \cdot 10^{-3}$ |

Table 4.5: Step response analysis results.

This method can only identify the (symmetric) Coulomb and viscous components of friction. In cases where only these components exist (along with static friction)

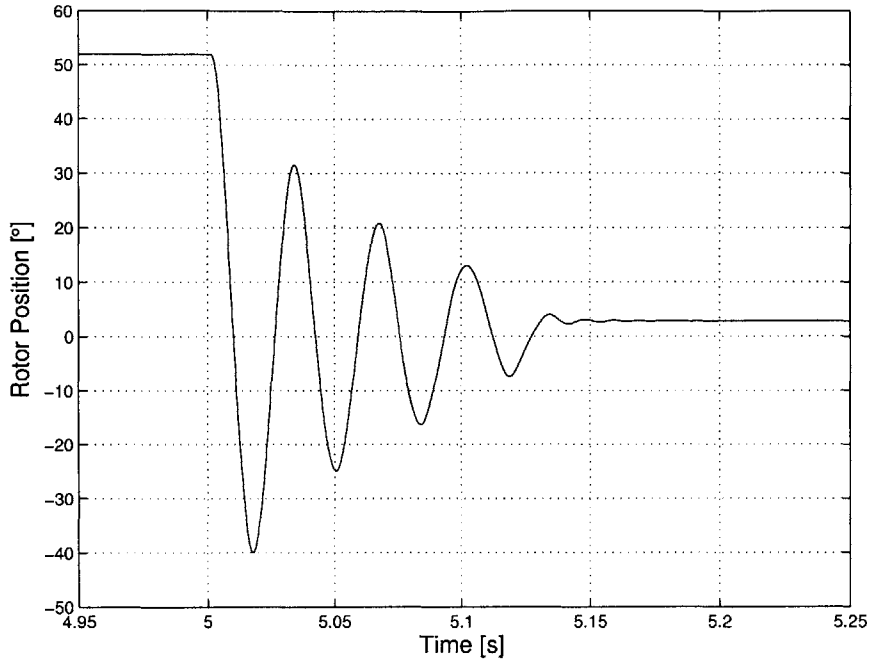


Figure 4-16: Typical step response for ADR motor connected to its first gear stage; step size = 50 °, $k = 0.015\,\frac{\text{Nm}}{\text{rad}}$.

the parameters $\beta$ and $\theta_k$ obtained from each set of peaks and valleys should be independent of the index $i$. This is not consistently the case through these trials; variability in these derived parameters from test to test shows that they can only be relied upon as rough estimates. Other characteristics that are not accounted for, including other forms of friction, may explain the deviations from the expected response. The most likely cause of such problems is cogging in the motor. Notice the residual oscillations in Fig. 4-17. The controller used is a simple proportional controller and this effect can appear in all three axes. This implies that they are not backlash induced, since at this point in the testing, the PS axis has no backlash[7]. These oscillations could be caused by cogging. Figure 4-18 shows the motor torque as a function of rotor position for a constant controller gain ($0.015\frac{\text{Nm}}{\text{rad}}$). This controller clearly has a single, stable equilibrium point at the origin. The actuators are known to have 18 cogs per revolution. The cogging map, assumed to be sinusoidal in form

[7]A single gear, by definition, can exhibit no backlash.

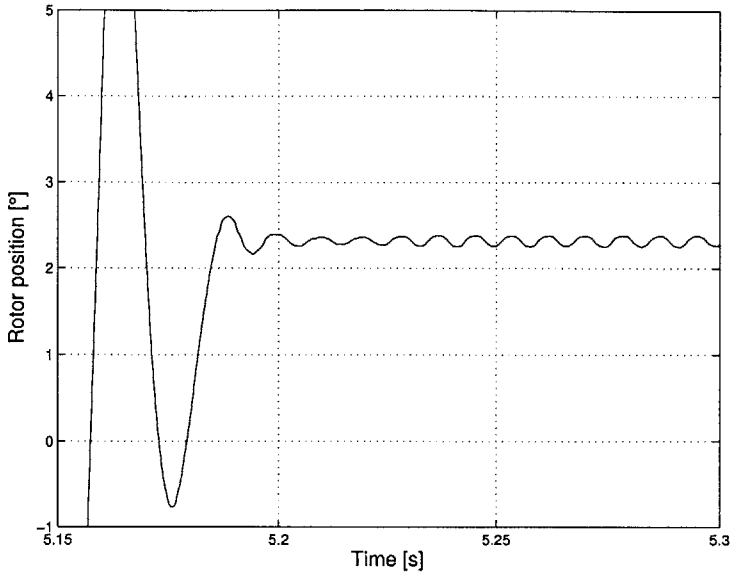


Figure 4-17: Oscillation in first stage of ADR during a step response test. A simple proportional controller is being applied.

with an amplitude equal to the magnitude found in Table 4.2, can be superimposed onto the control law, as plotted in Fig. 4-18. For this simulation, there are now three equilibria, of which only two are stable. The location and nature of the resulting of the equilibria in this simulation depends on the location of the cogging map with respect to the controller equilibrium point. This effect is presented here mainly as data; its implications will be investigated in Chapter 6.

## 4.4 Conclusions

The major components have been reviewed and tested. Amplifier and actuator dynamics have been identified and do not appear to be significant for the range of expected operating frequencies for the device. There is a first order filter behavior with a corner frequency of 275 Hz that is attributed to the actuator electrodynamics. The existence of pure time delays in the amplifier/actuator dynamics along with the effects of sampling at 1 kHz are also modeled and may prove significant in the analysis of stability.

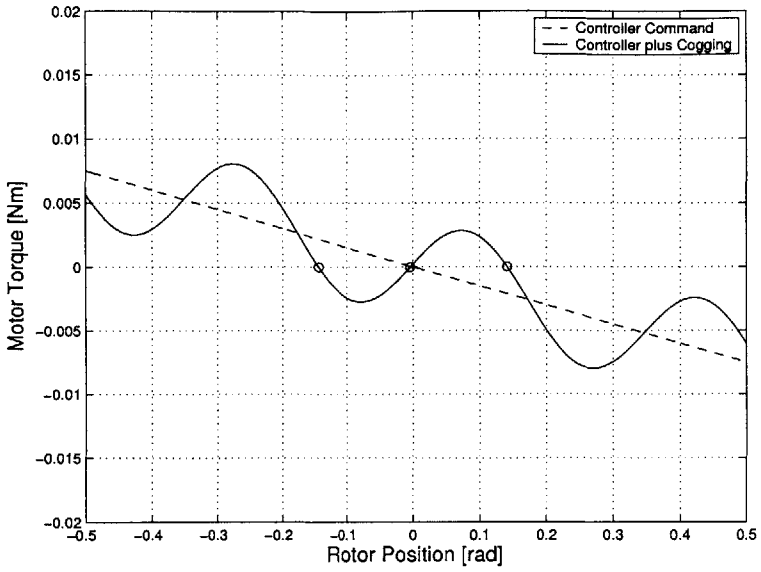


Figure 4-18: Cogging instability simulation. The controller, in P control, has a stable equilibrium point at the origin. Superimposing the cogging map results in three equilibria, with the center one unstable.

Static testing with the amplifiers and actuators show linear responses with the constants of interest determined. The motors exhibit both torque ripple and cogging. An introduction to the basic friction models used in this thesis along with the identification of this friction in the transmission elements has been presented. The identification method used with the step response tests will be repeated in the next chapter, noting its inability to account for the effects of cogging. Investigation of the performance of individual components used for the robot provides some much-needed insight into the its overall operation. The system identification work that remains will use these results in an attempt to describe the operation of the assembled robot.

# Chapter 5

# System Characterization

The main features of the robot, introduced in Chapter 3, are now translated into a model capable of describing the system behavior. In order to guarantee patient safety while interacting with the device, one must have the capability of predicting its response in a given environment. Models are useful in the development of controllers, as they allow for simulation. They also indicate the relative contributions of design parameters to observed behavior and, therefore, aid in the redesign process. In this chapter, some overall characteristics of the machine are examined. Parameters are then identified by examining the system response to simple inputs, namely step and ramp inputs.

## 5.1 Position Calibration

Encoder operation has been verified using Kollmorgen software that checks the resolution and accuracy of the position feedback with the actuator. Since the encoders are located on the actuators, however, they do not completely define the orientation of the robot end effector. Further, the handle orientation does not completely define the patient posture, a topic that will be revisited in section 5.4. Recall Eqs. 3.5 relating the motor angles to the angles describing the orientation of the robot arm. The reference position for these angles involves the handle being upright and centered so

that, when the patient is secured in this position, his wrist rotations are neutral[1]. A brief series of tests were conducted to verify the orientation of the handle with regard to sensor readings[2]. The handle, seated in the nest block described in section 3.5, is positioned in a horizontal plane using precision angle blocks, generally used for orienting work in a mill for machining. Moving the robot through its flexion/extension range involves rotations of both the ADL and ADR motors, giving a satisfactory representation of the posture of the DIFF axes. The PS position, monitored through the tests, stayed within $\pm 2\,^\circ$ of its nominal rest position. Figure 5-1 shows the results of the tests, taking into account the gear ratio of $\sim 8.14$. The reference and measured positions are all within $\pm 1.5\,^\circ$ of each other, with an RMS error of $0.45\,^\circ$.

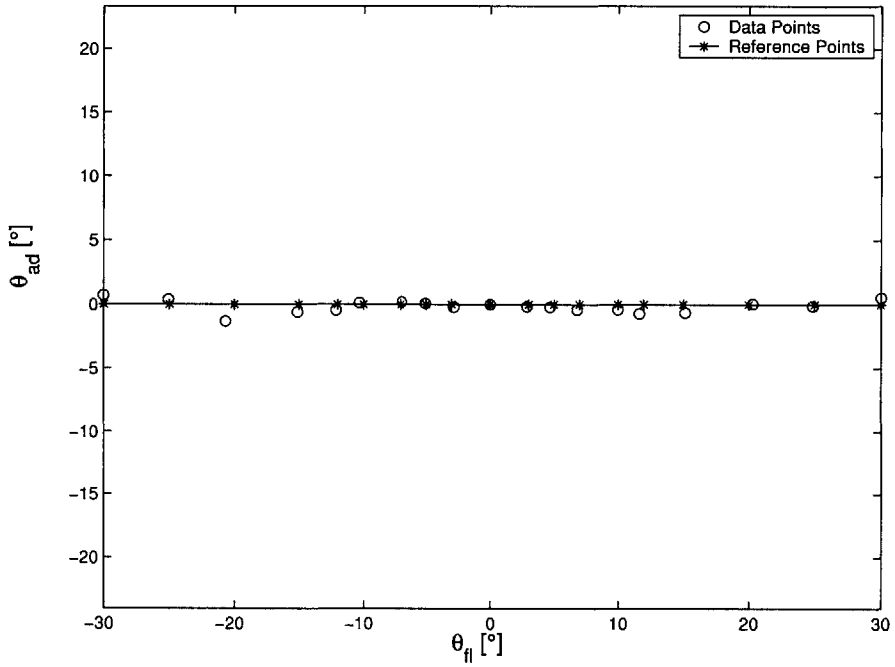


Figure 5-1: DIFF Position calibration results. Measured points are represented in joint space by circles, while the solid line shows the reference points used.

For the PS axis, the orientation of a chord parallel to the diameter of one of the ring gears was measured using a grounded protractor. The protractor measurements

[1]The wrist extension necessary to grasp the handle is ignored here.

[2]No further attempts have been made to characterize the "wobble" noted in section 3.3 since the encoders currently function with the servo-amplifiers.

match up well with the encoder readings, as seen in Fig. 5-2. Data points were taken at 5 ° intervals throughout the range of motion. The device was designed to have a range of 76 ° in each direction. Cable interference with the table, however, limits this range below 60 °. Recall that the gear ratio for the PS axis is nominally 10.5. Here, the data points are all within ±0.53 ° of each other, with an RMS error of 0.26 °.

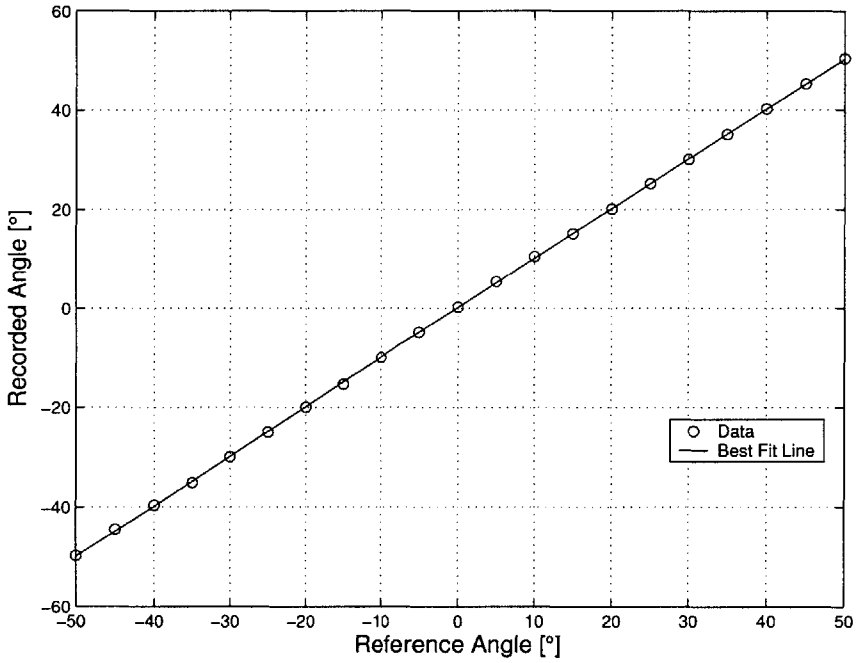


Figure 5-2: PS position calibration results. Reference points occur at 5 ° intervals.

### 5.1.1 Backlash Levels

The endpoint position of the robot cannot be known with any greater accuracy than the backlash levels present in the device. Chapter 3 covered some of the sources of backlash in this mechanism. Data from the position response to any locked-rotor endpoint test can provide a measure of the magnitude of the play in the system. Figure 5-3 shows such a setup, also used for the force production calibration described in the next section. In general, the backlash will vary as a function of the position due to, for example, the variation in tooth thickness on a single gear. Exhaustive characterization of the total composite error (TCE) of the transmission as a function

of orientation was not carried out here. Instead, backlash levels are estimated by measuring the discontinuities in the position response during torque reversals in the locked-endpoint configuration of Fig. 5-3. Table 5.1 summarizes the backlash levels as measured by the encoders at each pinion and the corresponding effects on endpoint position.

| **Motor** | **Backlash at Pinion [°]** | **Backlash at Output [°]** |
|---|---|---|
| ADR | 5 | 0.61 |
| ADL | 4 | 0.49 |
| PS | 5 | 0.48 |

Table 5.1: Measured backlash levels.

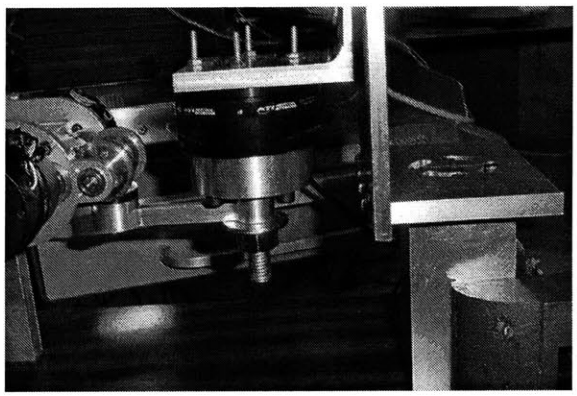

Figure 5-3: Endpoint force calibration setup. The robot arm can be positioned and secured within the workspace.

## 5.2 Endpoint Force Calibration

The setup of Fig. 5-3 was positioned throughout the robot workspace in an attempt to verify the robot's force producing capabilities. The position calibration results suggest that the force production will be predictable through the fundamental law of gearing, *i.e.*, the torque measured at the differential gear should equal the motor torques scaled by the corresponding gear ratio. The robot was indexed prior to

the trials so that the encoder readouts would accurately represent the orientation of the arm. The information from a six-axis ATI Gamma force transducer with 12-bit resolution was used in conjunction with position and orientation information from the setup to compare the measurements with the expected values during open loop tests. Five tests were conducted at each of eleven positions: each actuator was tested, as were flexion/extension and abduction/adduction movements. For nominally static test results, a slow (0.1 Hz) open loop voltage command was sent to the desired actuator, with tests conducted at 40% and 90% of the maximum actuator output. Frequency response tests were also conducted for a rough estimate of the bandwidth of the system by commanding a 3-V sinusoid to each axis over a range of frequencies. As in the testing in section 4.2.3, the presence of backlash complicates the analysis of these test results. Despite the difficulty in obtaining a frequency response for the device, no new bandwidth-limiting effects were found.

The static testing revealed some of the problems due to shaft bending discussed in Chapter 3. With both the robot arm and the base of the robot grounded to the same frame, one would expect the recorded motions to be insignificant. This, however, was not the case, as seen in Figs. 5-4. The shafts, most noticeably the differential shaft, are not stiff enough to counteract the forces developed between mating teeth, therefore allowing the pinion to move considerably. The structural instability addressed in section 3.4.2 is also noticeable in Fig. 5-4(b).

Forces and torques measured at the force transducer are reflected back to the differential axis for comparison with the commanded values. A number of factors hamper the force sensing capabilities of this setup including the aforementioned motion during testing and friction effects that may contribute to hysteretic torque responses[3]. Still, the recorded data proved to be clean and self-consistent and, therefore, useful in characterizing the system. Figures 5-5 and 5-6 show some of the data collected during the force calibration. Figure 5-5 shows that the data for the PS axis agrees with the expected slope from the motor calibration of Chapter 4. The DIFF axes

[3]One other possible cause for the hysteretic torque responses shown is hysteretic damping in the structure. It has already been established that the steel shafts deflect during operation.

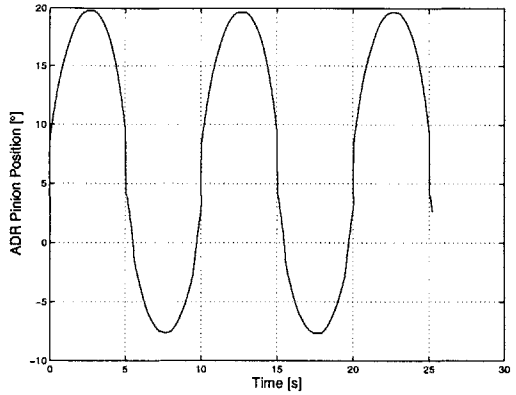


(a) ADR actuator response to ADR command.

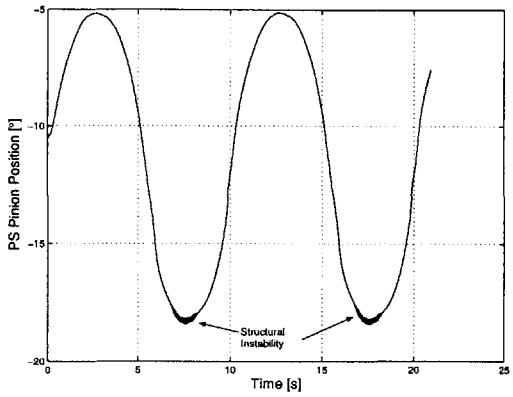


(b) PS actuator response to PS command. Note the presence of (structural) instability.

Figure 5-4: Typical position responses during "locked" endpoint testing. Motor commands are swept up to 90% of saturation at 0.1 Hz.

results, as seen in Figs. 5-6, show reasonably linear behavior (especially during the flexion/extension test shown). The ADR and ADL torque responses are readily obtained from this information using Eqs. 3.6. These measurements matched up well with data from tests in which commands were sent to only one of the motors. The apparent motor torque constants found through the force calibration differ from those found in Chapter 4 by nearly 30%. Recall that the ADR and ADL motor calibration of Chapter 4 was complicated by the front-mounted encoder assembly. Considering the fact that the setup for the force calibration tests required the actuators to be seated in their final positions and functioning properly, the results of these tests are likely more significant. Using the gear ratio, verified through the position calibration, the motor constants can be calculated for each actuator. These values, presented in Table 5.2, are used for the remainder of this thesis.

## 5.3 System Identification

There are a number of quantities that are of immediate interest in determining the system response. Among these are the inertia and friction characteristics of the

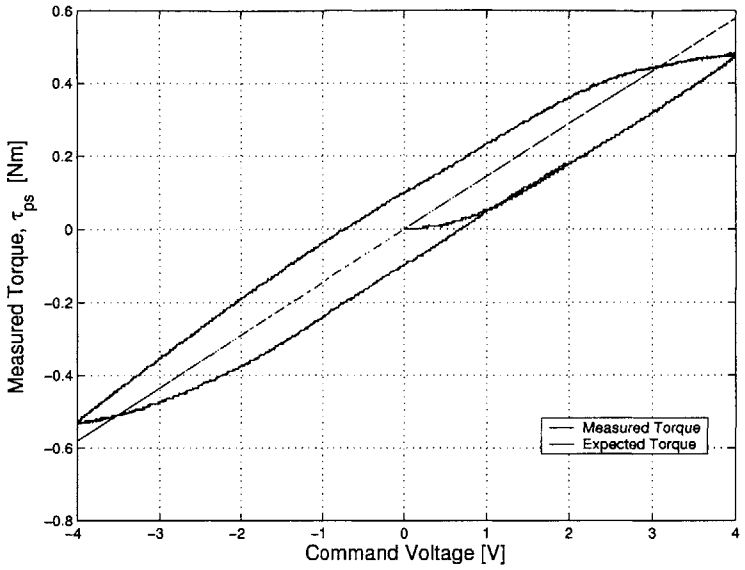


Figure 5-5: Typical PS force calibration results. The measured data is shown with a line representing the expected PS torque.

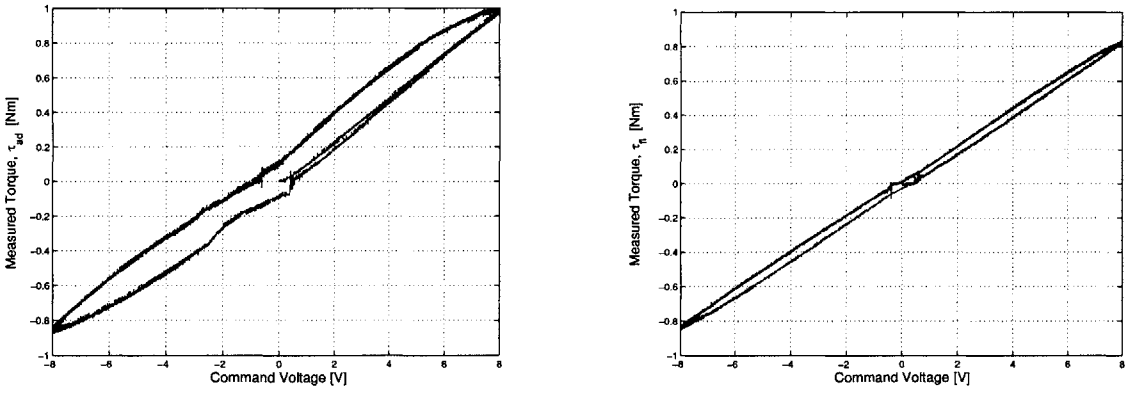


(a) Abduction/adduction test.

(b) Flexion/extension test.

Figure 5-6: Typical torque responses during "locked" endpoint testing.

| Motor | Torque Constant $[\frac{Nm}{V}]$ |
|---|---|
| ADR | 0.0139 |
| ADL | 0.0133 |
| PS | 0.0138 |

Table 5.2: Endpoint force calibration results.

robot endpoint. A model-based estimation of these parameters is carried out in this section. As an initial simplification, each axis will be considered separately and the consequences of such simplifications will be noted. In each of the tests, the handle is immobilized along the linear ball slide guide and the axes not being tested are held with some nominal stiffness. Ramp responses allow for the identification of gravity terms and static friction contributions while step responses allow for the identification of inertia and dynamic friction terms. The techniques used for the extraction of the parameters of interest from this data are also discussed, save the analysis for step responses introduced in section 4.3.

### 5.3.1 PS Transmission

The PS actuator carries the entire DIFF transmission housing and its actuators through the ring gear, contributing to the inertial and gravitational loads on the system. The act of carrying the motors contributes an estimated $7.4\,\text{lb}\cdot\text{in}^2$ to the endpoint inertia of this axis (compare this to the inertia specification offered in section 3.1 of $10-15\,\text{lb}\cdot\text{in}^2$). The location of the center of gravity for this subsystem lies below the PS axis of rotation, accounting for the presence of significant gravitational loading on the system. The basic model for this axis involves actuation through a gear with lumped friction properties and a position-dependent gravity load. The actuators are modeled as ideal effort sources based on their performance in the static and dynamic responses from Chapter 4. For the tests in this chapter, position feedback from the incremental encoders is used to program the actuator to behave as a spring (with a programmable, time-varying equilibrium point). Stiction, Coulomb friction, and viscous friction are all expected to be present in this axis. Motor cogging turns out to

be an important contributor to the overall system behavior as well. Cogging results in a periodic potential as a function of rotor position so that, in the neighborhood of a cog, there is a spring-like behavior. Actuator effort is transmitted to the handle through the ring gear/motor pinion pair, whose gear ratio is 10.5 (as verified during the torque calibration above). The backlash in this gear train must be modeled to reflect the position response during torque reversals and plays an important role in limiting stability. The bulk of the inertia is located downstream of the gear reduction. The position-dependent gravity load behaves as a nonlinear spring when viewed from the actuator.

### Ramp Input Results

Figure 5-7 shows a typical test result for inputting a ramp position command to the PS axis. The controller is a simple proportional feedback with test conditions given in Table 5.3. Each ramp test consists of holding the axis at neutral for five seconds, ramping up for five seconds, holding for five seconds, ramping down for ten seconds, holding for five seconds, and finally ramping back up to the neutral position where it is held until the experiment is terminated. Two immediately noticeable effects are the plateaus in position and the steady state error. The steady state error is mostly accounted for by $\tau_g$, the gravitational load on the system[4],

$$\tau_g = mgh \sin\theta_{ps} \tag{5.1}$$

where $mg$ is the weight of the transmission housing, $h$ is the distance between the PS axis and its center of gravity, and $\theta_{ps}$ is the endpoint PS orientation (the angle the DIFF axis makes with the horizon). The stepping characteristic of the position response, more readily seen in the zoomed-in view of Figure 5-8, is caused by a combination of static friction (stiction) and cogging phenomena.

The ramp tests are analyzed by examining points at which the system is at rest.

[4]The static friction also contributes to the steady state error, but does not have the strong position dependence exhibited by the gravitational load.

| Controller Gain $[\frac{\text{Nm}}{\text{rad}}]$ | Pinion Ramp Rate $[\frac{\text{°}}{\text{s}}]$ | Number of Tests |
|---|---|---|
| $39.5 \cdot 10^{-3}$ | 50 | 4 |
| $39.5 \cdot 10^{-3}$ | 100 | 4 |
| $79.1 \cdot 10^{-3}$ | 50 | 4 |
| $79.1 \cdot 10^{-3}$ | 100 | 4 |

Table 5.3: PS ramp test conditions.

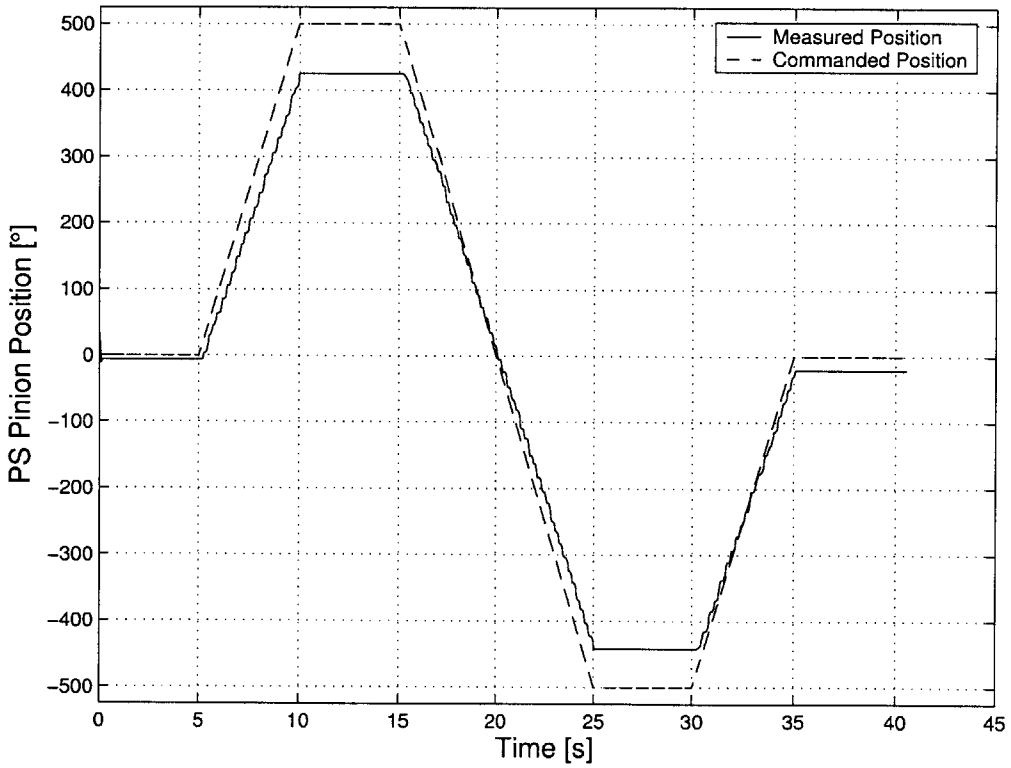


Figure 5-7: Typical PS ramp result; $k = 39.5 \cdot 10^{-3}\ \frac{\text{Nm}}{\text{rad}}$.

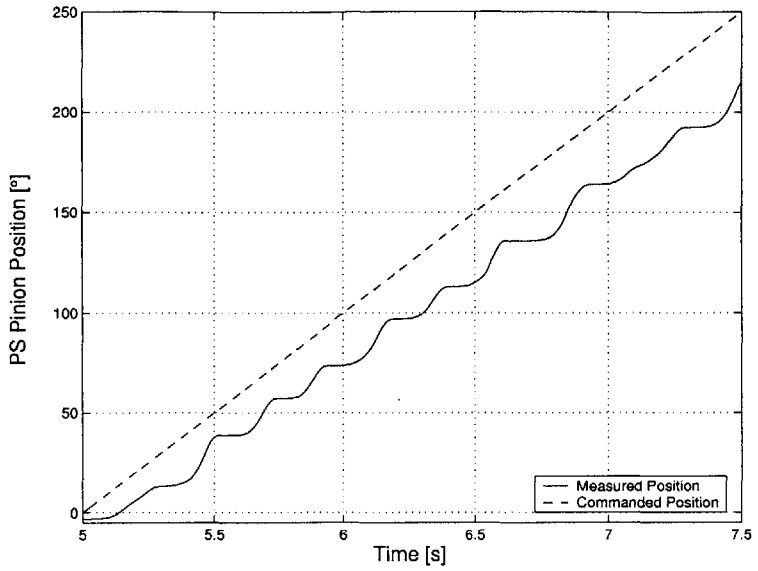


Figure 5-8: Blowup of a portion of Fig. 5-7.

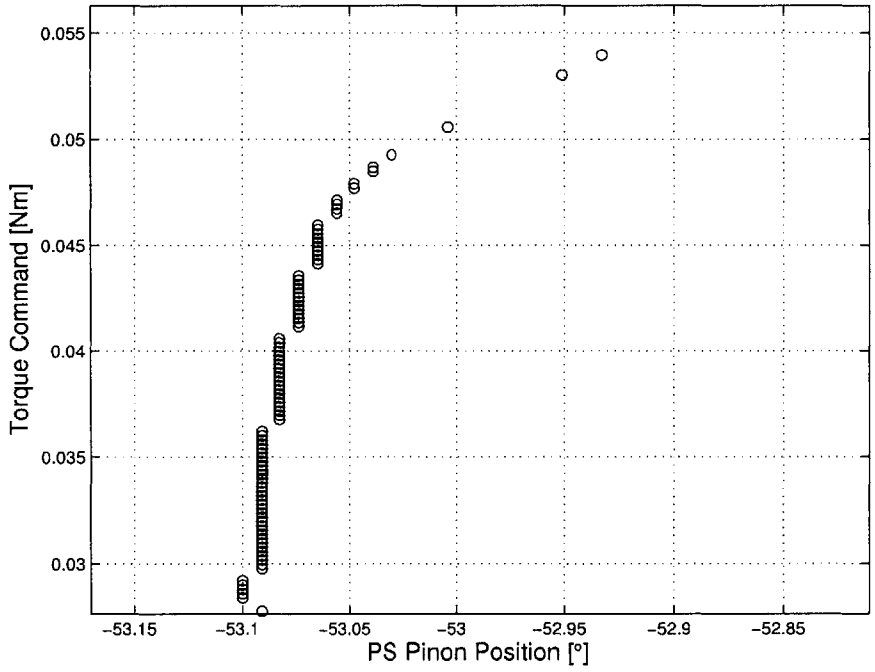


Figure 5-9: Breakaway during PS ramp test.

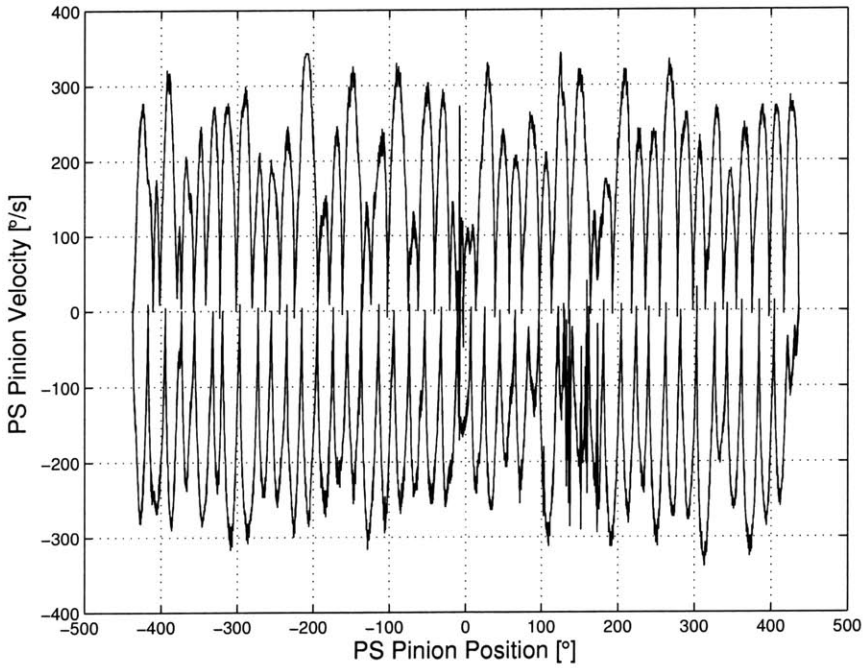


Figure 5-10: PS pinion velocity versus position during ramp test.

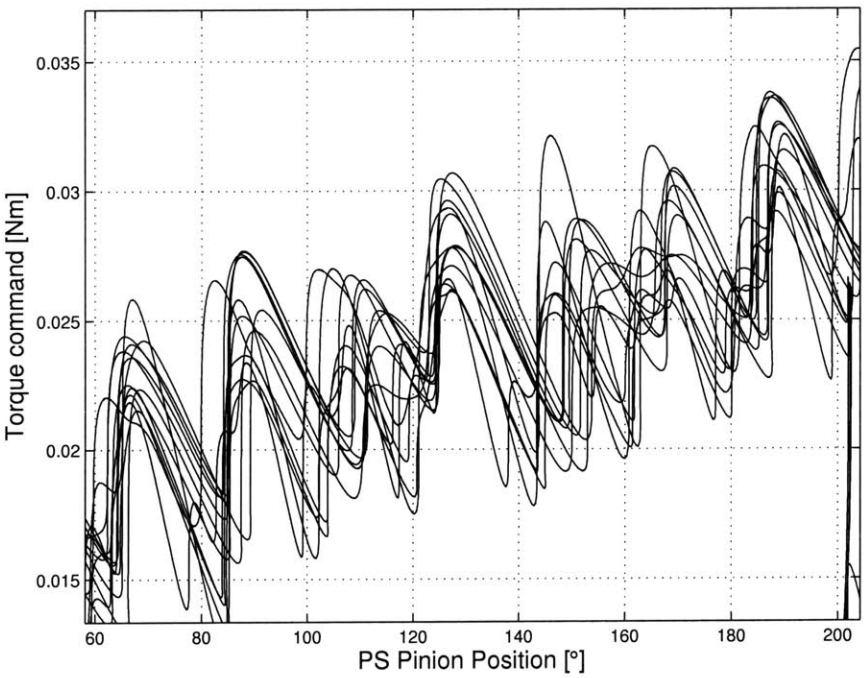


Figure 5-11: Ramp test results over many trials.

In doing so, the dynamic effects do not need to be considered. Figure 5-9 analyzes the zero-velocity points of this response at the end of a single plateau, plotting the torque command versus the rotor position. A static friction model requires that the position remain constant until the torque provided by the motor is high enough to break static friction and move. The effect shown here is typical of Dahl or Lu Gre models of friction, in which the interaction of asperities is modeled with some compliance. Another possible explanation for this apparent compliance is the motor cogging, which can behave like a spring in regions close to the location of the cog. Examination of the velocity versus position in Fig. 5-10 shows that the system does come to rest[5] at fairly regular intervals of 20°, consistent with the observed fact that the motors go through 18 cogs per revolution. The cogging map, however, is not purely sinusoidal in nature; the perceived gaps and variations of the positions of zero velocity crossings are due to motor specific factors such as irregularities in the windings, slot geometry, and air gap geometry that, while varying in rotor position, are not necessarily strong functions of rotor position. This, in addition to an unknown, complicated friction function may account for the variation in gap spacing in Fig. 5-10. Figure 5-11 plots the command torque versus rotor angle results for all trials. The data seems fairly repeatable with some results following nearly the exact same path and others following slightly different ones. This points toward an underlying structure for whatever effect is causing the stepping characteristics, albeit a highly nonlinear one. Attempts at fitting a periodic waveform to this data in order to have a model that accurately captures the cogging characteristics were unsatisfactory. For the purposes of the model developed in this chapter, the effects of cogging are lumped together with those of static friction. The consequences of this assumption can be evaluated at a later date.

Calculation of the gravity load and static friction involves analyzing the zero-velocity points on a torque versus position plot (Fig. 5-12) while the robot is moving against gravity. The torques used are the scaled input commands recorded by the

[5]The system is considered to be at rest when the magnitude of the velocity is below the threshold of 20 $\frac{\circ}{s}$ of pinion velocity.

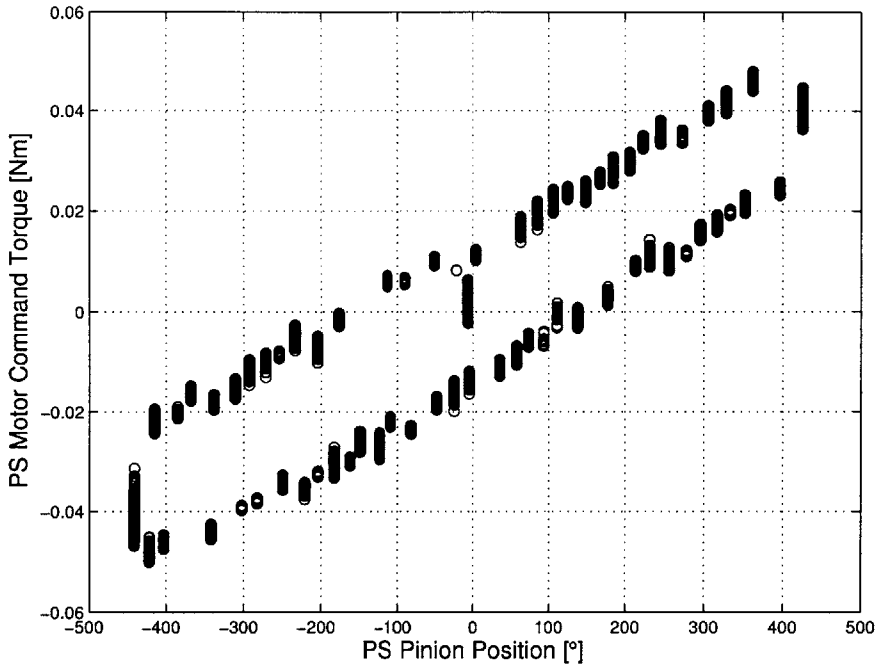


Figure 5-12: PS ramp test response (zero velocity points).

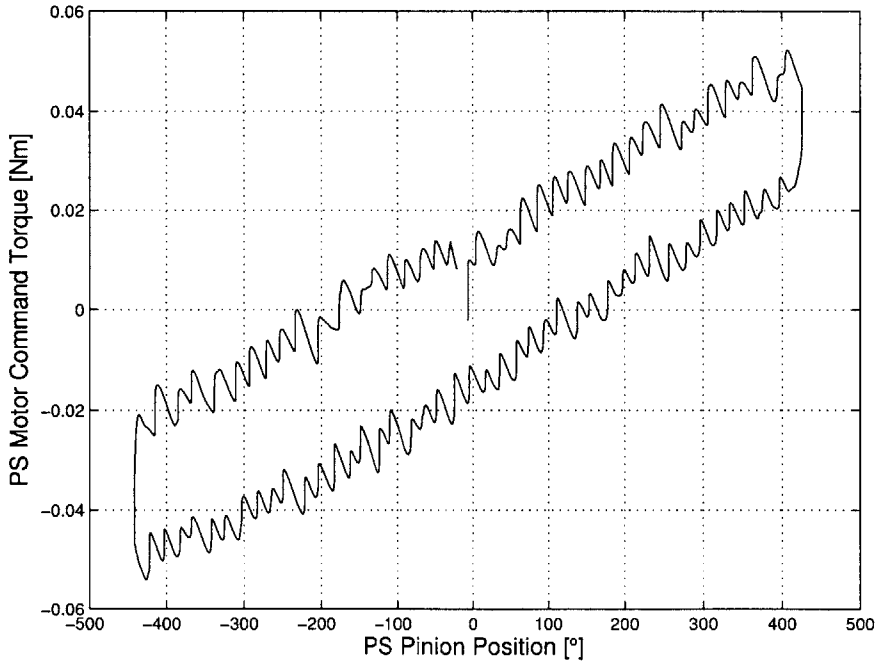


Figure 5-13: PS ramp test response (all points).

computer. The apparent gaps in the plot are due to positions where the system does not come to a complete stop. The full plot of torque versus position in Fig. 5-13 shows that the system indeed alternates between sticking and slipping with some irregularities. The static friction could be estimated as the highest torque recorded at $\theta_{ps} = 0\,^{\circ}$, where there is no gravity load on the system. Alternatively, the entire set of maximum torques[6] is fit to a function of the form

$$\tau = (mgh)\sin\theta_{ps} + \tau_s\,\mathrm{sgn}(\theta_{ps}) \tag{5.2}$$

where $\tau_s$ is the magnitude of the static friction function. The sign of $\theta_{ps}$ can be used to calculate the static friction because motion against gravity is being considered. Fitting the data to this function using `fminsearch`[7] results in an estimated static friction of 0.015 Nm at the motor along with a gravity load of 0.054 Nm. Reflected out to the endpoint, this analysis estimates a lumped static friction of 0.158 Nm and a gravity load of 0.57 Nm, suggesting that the center of gravity is located on the order of a few centimeters from the PS axis. This model, as seen in Fig. 5-14, accounts for 98.7% of the variance in the data. The plot shows the motor command torque required to balance gravitational forces as a function of $\theta_{ps}$. Notice that in the range of operation shown, the sinusoidal function is nearly linear.

Figure 5-15 shows the oscillation of the PS pinion about the moving average of its position as computed using a least-squares regression over the first 5 seconds of movement. The response is somewhat irregular, *i.e.*, it cannot be easily described by, say, a single sinusoid. Even so, this supports the idea of modeling this effect as a stick-slip limit cycle oscillation[8]. Upon breaking static friction, the moving pinion is slowed by damping until it stops again. The equilibrium point continues to move away from the current position until the actuator torque, behaving as a spring, is again high enough to break static friction, thus repeating the cycle. Figures 5-16

[6]The set of command torques at breakaway points as suggested by the highest point in Fig. 5-9.

[7]`fminsearch` is an optimization solver provided by MATLAB. It is briefly discussed in Appendix B.

[8]In Figs. 5-15 and 5-16, $\omega_{ps}$ is the PS pinion velocity and $\Delta\theta_{ps}$ is the difference between the PS pinion position and the equilibrium position as determined by least squares regression.

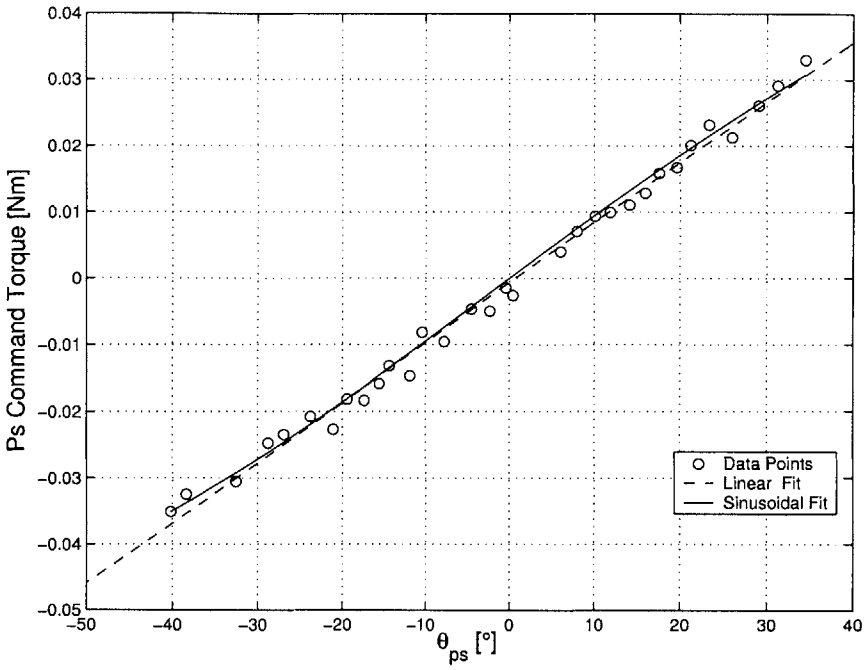


Figure 5-14: PS ramp test fit results.

show closed loops in the phase plane, indicating the existence of limit cycles. The zero-velocity band, clearest in Fig. 5-16(a), shows the effect of static friction.

### Step Input Results

Step response test were conducted and analyzed in the manner discussed in section 4.3[9] according to the parameters given in Table 5.4. The frequency of damped oscillations along with the decrement are used to find the system's dynamic parameters. The analysis method allows for the calculation of inertia, viscous friction, and Coulomb friction, but is not accurate when applied to systems exhibiting other nonlinearities. While neither cogging nor backlash were perceptible in the feel of the robot before the test[10], these phenomena are known to be present. Accordingly, the results of this analysis must be examined carefully. Ultimately, the model will be ver-

[9]Recall that a single step "test" consists of four distinct step responses.

[10]These tests were performed with the PS axis still in an anti-backlash configuration. See section 3.4.2 for details.

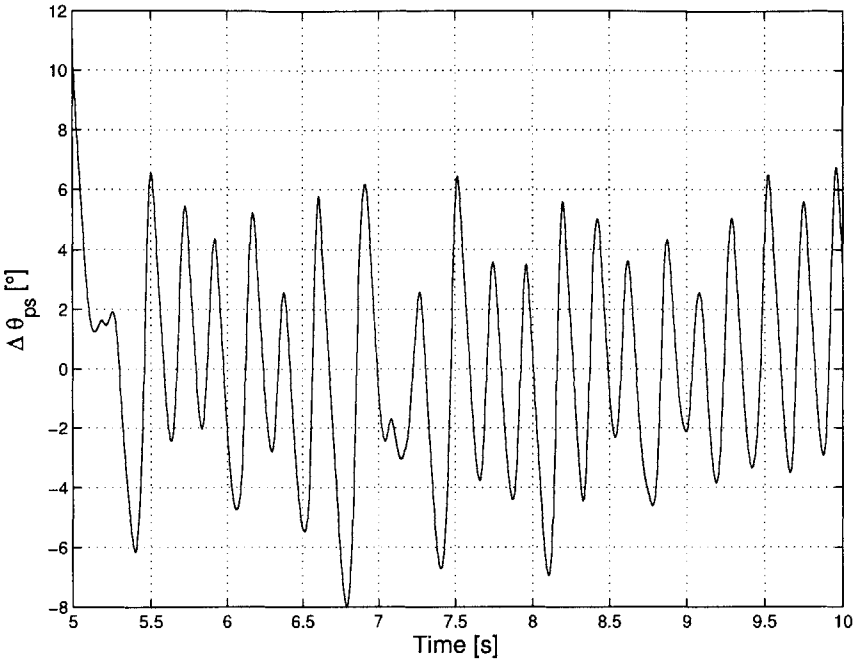


Figure 5-15: PS pinion oscillation about its average position.

| Controller Gain $[\frac{\text{Nm}}{\text{rad}}]$ | Pinion Step Amplitude [°] | Number of Tests |
|---|---|---|
| $39.5 \cdot 10^{-3}$ | 100 | 6 |
| $39.5 \cdot 10^{-3}$ | 300 | 6 |
| $79.1 \cdot 10^{-3}$ | 100 | 6 |

Table 5.4: PS step test conditions.

ified through simulation, helping to address concerns with the parameter estimation techniques. Figure 5-17 shows a typical position response to a step in input for the PS axis. Steady state errors are expected in the response as caused by gravity (when the equilibrium position is not gravity-neutral) and static friction. The steady state errors observed throughout testing do not contradict the level of static friction found in the ramp response testing.

The oscillations are characterized by a damped frequency of $28.6\frac{\text{rad}}{\text{s}}$ and a damping factor $\zeta$ of 0.26. This yields a natural frequency $\omega_n$ of $29.6\frac{\text{rad}}{\text{s}}$. Steps toward a gravity-neutral position, as the one shown in Fig. 5-17, have an additional component to their

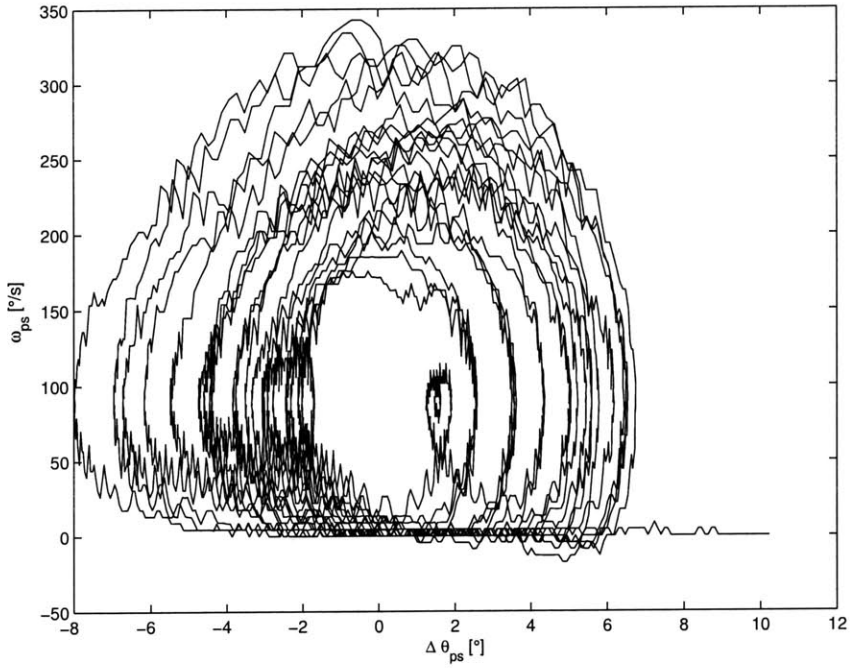


(a) During first leg of PS ramp test.

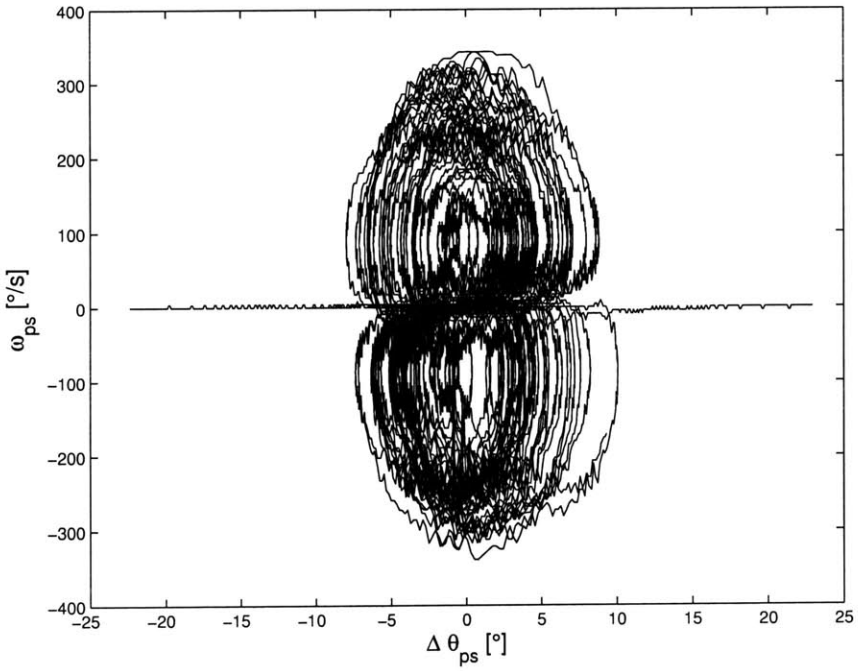


(b) Over full course of ramp test.

Figure 5-16: Phase-plane portraits for PS ramp test.

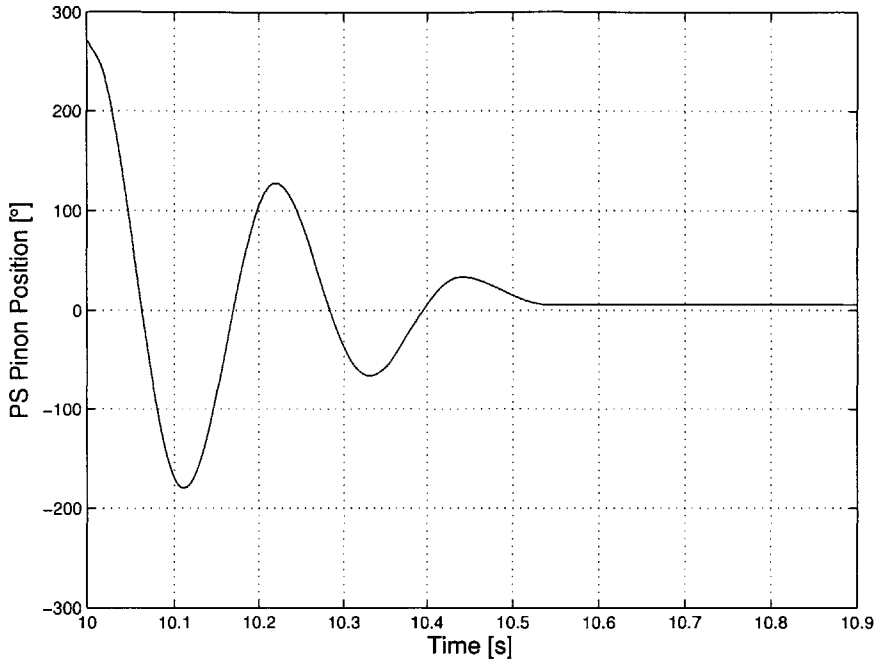


Figure 5-17: Typical PS step response.

stiffness. Using the linear approximation for the gravity loading, the stiffness $k_m$ of the mechanism is

$$k_m = k_{ctrl} + k_{g,lin} \tag{5.3}$$

where $k_{ctrl}$ is the controller stiffness as specified in Table 5.4 and $k_{g,lin}$ is the linearized gravitational stiffness, estimated as $4.97 \cdot 10^{-3} \frac{\text{Nm}}{\text{rad}}$, significantly lower than the controller stiffness. From these, the endpoint inertia of the PS axis, $J_{ps}$, is estimated as $5.6 \cdot 10^{-3}\,\text{kg} \cdot \text{m}^2$ ($19.1\,\text{lb}\cdot\text{in}^2$), the viscous damping coefficient is estimated as $0.086\,\frac{\text{Nm s}}{\text{rad}}$, and the Coulomb friction term is estimated as $0.085\,\text{Nm}$.

Using the parameters summarized in Table 5.5, the system response to various inputs can be simulated. For the purposes of these simulations, velocities below some nominal threshold (specified to be $\omega_{ps} < 0.01\,\frac{\text{rad}}{\text{s}}$) are considered equal to zero and, therefore, subject to stiction forces. This is to account for the precision of the MATLAB simulation using numerical differential equation solvers from the ode family. The simulation qualitatively reproduces the stepping quality and the steady

| Endpoint Inertia | $5.6 \cdot 10^{-3}\,\mathrm{kg} \cdot \mathrm{m}^2$ |
|---|---|
| Endpoint Static Friction | 0.157 Nm |
| Endpoint Coulomb Friction | .085 Nm |
| Endpoint Viscous Friction | $0.086\,\frac{\mathrm{Nms}}{\mathrm{rad}}$ |
| Gravity Load | $0.57 \sin\theta_{ps}$ [Nm] |
| Endpoint Backlash | $0.48\,^\circ$ |

Table 5.5: PS model parameters reflected to the endpoint.

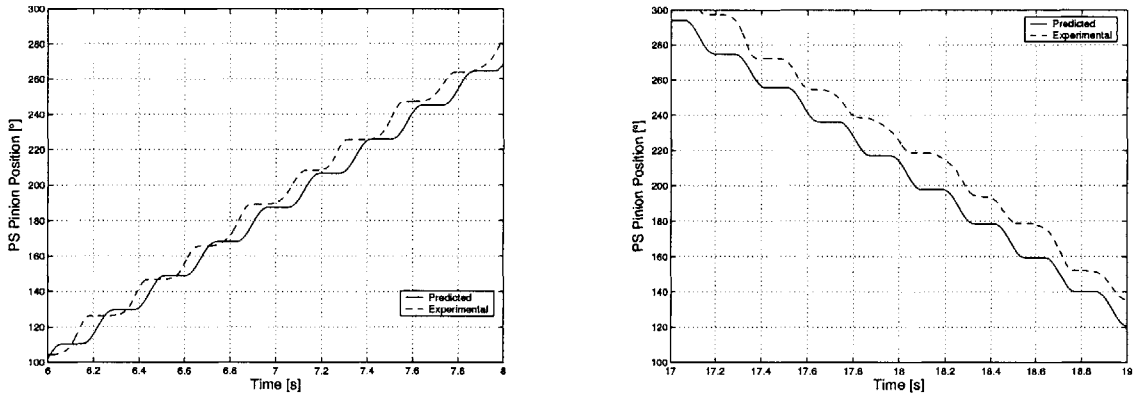


(a) Against gravity.

(b) With gravity.

Figure 5-18: PS simulation results with experimental data.

state error, the two main features noticed during those tests. The exact character of the ramp response is not predicted by this model, since the details of the cogging and the position dependence of the friction terms were not accounted for.

### 5.3.2 DIFF Transmission

The DIFF transmission, as previously discussed, involves the cooperation of the ADR and ADL motors through a two-stage gear reduction and differential gear mechanism to actuate the arm of the robot. The inertia and gravity effects for wrist rotations should be much less pronounced than those found in the PS axis. This is due to the fact that only the robot arm and handle are moved around by the actuators. The resulting handle motion from the ADR and ADL actuators should be decoupled. Experimentation has shown coupling between the axes due to an inability to eliminate

| Controller Gain $[\frac{\text{Nm}}{\text{rad}}]$ | Pinion Ramp Rate $[\frac{\text{o}}{\text{s}}]$ | Number of Tests |
|---|---|---|
| $38.7 \cdot 10^{-3}$ | 20 | 4 |
| $38.7 \cdot 10^{-3}$ | 50 | 4 |
| $77.0 \cdot 10^{-3}$ | 20 | 4 |
| $77.0 \cdot 10^{-3}$ | 50 | 4 |

Table 5.6: DIFF ramp test conditions.

the influence of gravity on the test setup. The remainder of this chapter presents the data collected for the DIFF axes. The test conditions and data analysis for the DIFF axis system identification are similar to those discussed above for the PS axis since, in essence, the same model is used for the ADR and ADL axes as for the PS axis. Each set of tests was conducted on the ADR and ADL axes individually as well as the ADR and ADL axes working together in both flexion and abduction.

### Ramp Input Results

The expected position dependence of the gravitational load for the DIFF axes is proportional to a cosine function so that, within the workspace of the robot, gravity always contributes an adduction torque. Denoting the gravity load $mgl$,

$$\tau_{g,diff} = mgl\ \cos(\theta_{ad} + \beta_{ad}) \tag{5.4}$$

where $\tau_{g,diff}$ is the gravity torque produced by the handle on the differential axis and $\beta_{ad}$ is a parameter indicating the angle of a line connecting the origin of the differential axis and the center of mass of the handle. Figure 5-19 shows a typical response for a ramp profile sent to the ADR motor. The results of these experiments exhibit the same characteristics as the results from the PS axis, though the difference between the actual angle and the commanded angle does not show as much of a position dependence.

Figure 5-20 plots the torque versus position curve for motion in pure abduction/adduction. The co-sinusoidal characteristic is noticeable and shows the peak torque (and, consequently, the neutral position) to occur at a negative angle, sup-

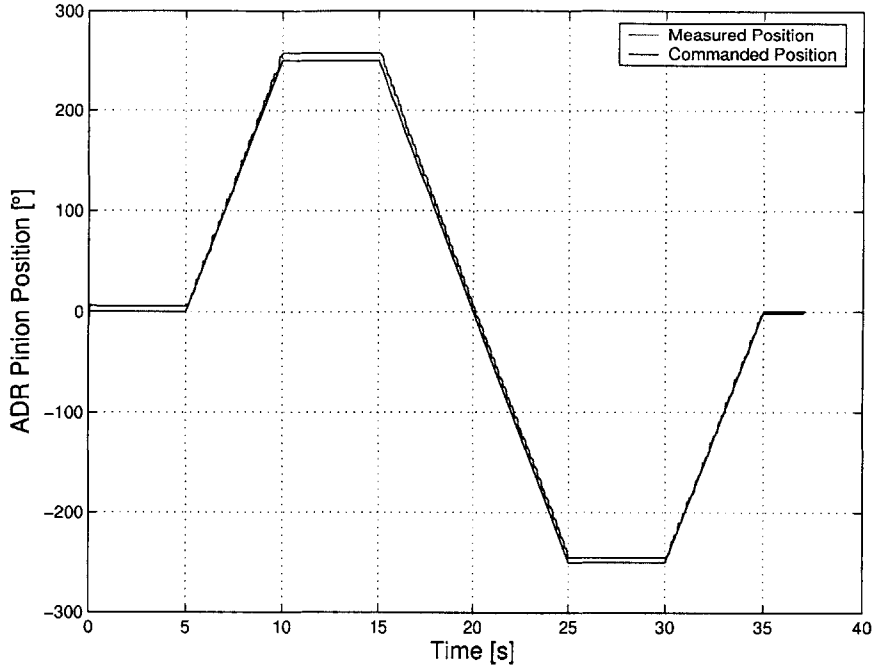


Figure 5-19: Typical ADR ramp result; $k = 38.7 \cdot 10^{-3} \frac{\text{Nm}}{\text{rad}}$.

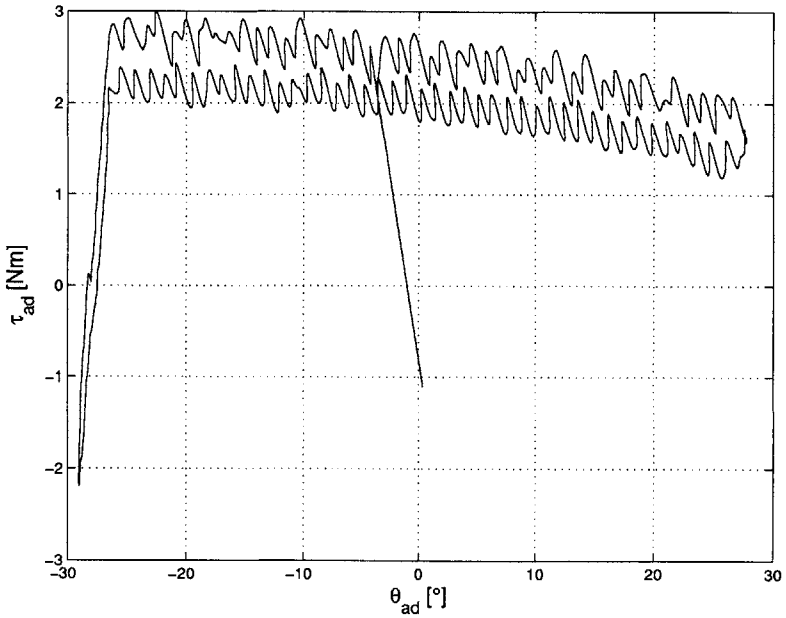


Figure 5-20: Response to command in abduction/adduction; $k = 77.0 \cdot 10^{-3} \frac{\text{Nm}}{\text{rad}}$. Central peak in torque is due to starting conditions, while peak in adduction torque is due to the robot pushing against a stop.

porting the model with some positive $\beta_{ad}$. The results show that the gravity load is nearly constant over the range of the experiment. Fitting to the model given above, $mgl$ is estimated to be 0.26 Nm and $\beta_{ad}$ is estimated to be 15.4 °.

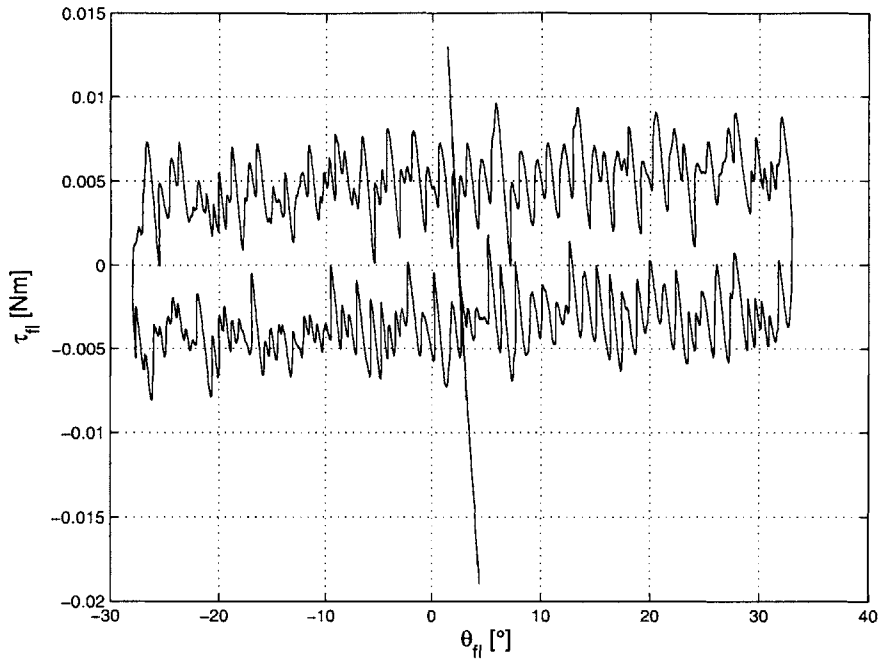


Figure 5-21: Response to ramp command in flexion/extension; $k = 77.0 \cdot 10^{-3} \frac{\text{Nm}}{\text{rad}}$. Central peak in torque is due to starting conditions.

Movements in pure flexion and extension are subject to a constant torque in abduction/adduction due to gravity, but the motion in flexion/extension should not be affected. Figure 5-21 supports this, showing the torque response[11] for a ramp test in flexion and extension. The fluctuation of the response over the course of the test is a result of the friction and cogging affects. The mean value of Fig. 5-21 does show some position dependence due to the nature of the tests: the controller gain for the ADR and ADL motors was set to the same voltage per degree without accounting for the slight difference in motor torque.

| Controller Gain $[\frac{\text{Nm}}{\text{rad}}]$ | Pinion Step Amplitude [°] | Number of Tests |
|---|---|---|
| $38.7 \cdot 10^{-3}$ | 50 | 4 |
| $38.7 \cdot 10^{-3}$ | 100 | 4 |
| $77.0 \cdot 10^{-3}$ | 50 | 4 |
| $77.0 \cdot 10^{-3}$ | 100 | 4 |

Table 5.7: DIFF step test conditions.

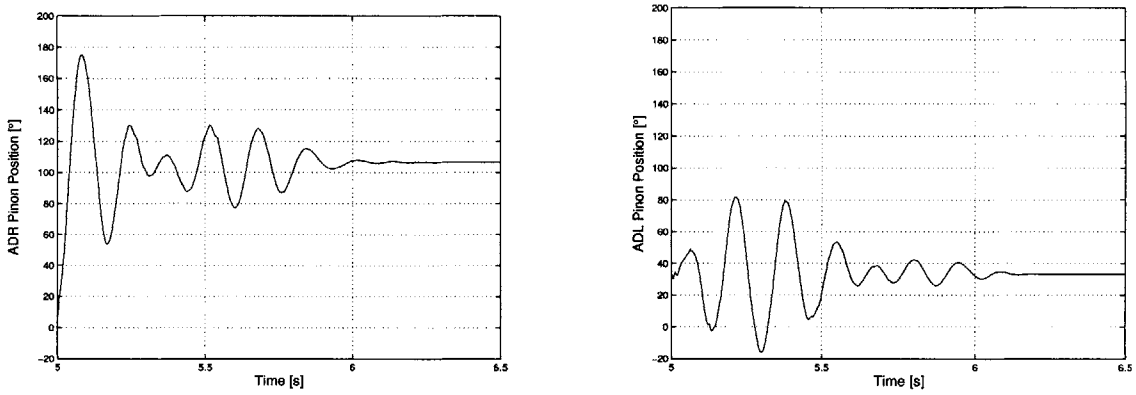


(a) ADR response.

(b) ADL response.

Figure 5-22: DIFF step response results for commanded step in ADR.

### Step Input Results

The gravity load encountered from the handle disrupts the character of the oscillations during a step response. This is shown in Figs. 5-22, the response of the ADR and ADL motors to a commanded step in ADR position. In order to analyze the characteristics of the system, a pure flexion/extension test will again be performed. Figure 5-23 shows such a response to be well behaved with a nearly linear decrement (indicating that Coulomb friction dominates viscous friction). The oscillations occur at a frequency of 6.8 Hz, so that the endpoint robot inertia (due mostly to the handle) of this axis is estimated at $0.34 \cdot 10^{-3}\,\text{kg} \cdot \text{m}^2$.

[11]Note that the reported command torques are actuator torques as opposed to endpoint torques.

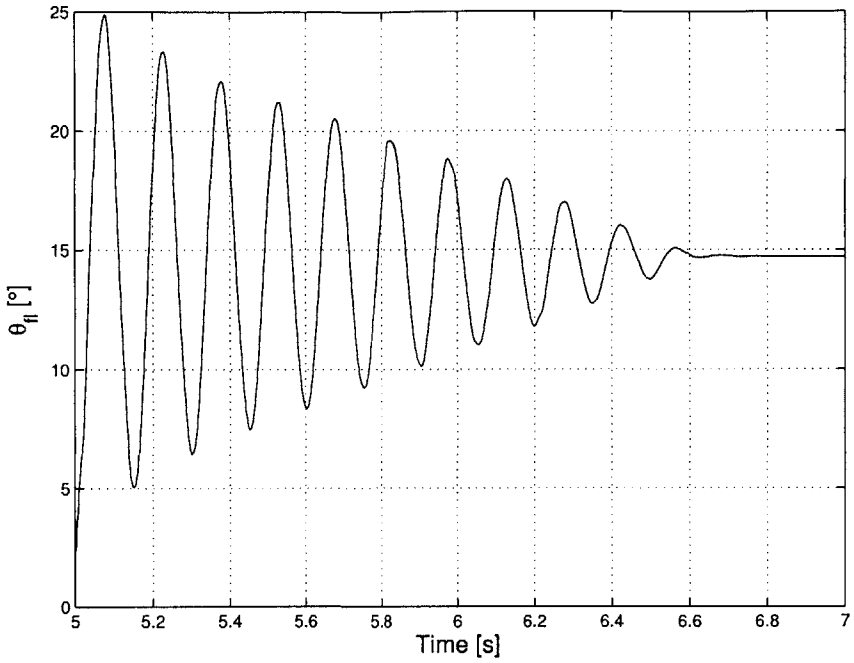


Figure 5-23: Response to step command in flexion/extension; $k = 77.0 \cdot 10^{-3} \frac{\text{Nm}}{\text{rad}}$.

## 5.4 Patient Interaction

The transmission of forces from the actuators to the base of the handle, as described in section 5.2 above, does not completely characterize the interaction between the robot and human. Patient posture has already been introduced as critical for proper robot operation. To review, the patient is secured at the bicep, wrist, and hand. The bicep constraint is meant to discourage the patient from lifting his arm out of the device and isolate forearm rotations during robotic therapy. The wrist is secured to the transmission housing to further ensure that the patient remains in the device and uses his wrist to move the handle around (rather than attempting to compensate by lifting the forearm, for example). The handle itself, heretofore left out of the modeling process, has two degrees of freedom to allow for mobility. Securing the patient's hand to the handle regulates the distance between the wrist and handle. This is particularly important for patients with a loose or flaccid grip, which can diminish the effectiveness of abduction/adduction training if not properly reinforced.

Ultimately, the transformation between motor torques and endpoint forces depends on specific patient geometry and robot orientation.

The PS properties were determined while commanding the DIFF axes to some nominal stiffness at its neutral position. The actual transmission characteristic of this axis will depend on the orientation of the handle. For $(\theta_{fl}, \theta_{ad}) = (0, 0)$, a PS torque produced by the robot is transmitted identically to the hand. Denoting $\tau_{ps,h}$ as the PS torque transmitted to the hand,

$$\tau_{ps,h} = \tau_{ps} \cos(\theta_{fl}) \tag{5.5}$$

so that the transmitted torque is a function of $\theta_{fl}$, but not $\theta_{ad}$. Initial trials with the device will focus on isolated forearm rotations and isolated wrist motions of pure abduction/adduction and pure flexion/extension along with some select circumduction motions[12]. This fact makes the angle dependence of $\tau_{ps,h}$ somewhat moot, but once combination wrist and forearm rotations are requested of this device, it should be noted.

During the design [54], the mechanism for abduction/adduction was correctly modeled as a single degree of freedom mechanism, shown in Fig. 5-24. In this figure, the robot axis and wrist axis are aligned, so that the closed loop chain defined by the wrist and robot consists of an inversion of a slider-crank mechanism. The transmission characteristic is dependent upon the patient size; the separation of the axes, $a$,(denoted in Fig. 5-24 by $\alpha$) can be approximated by the sum of half of the wrist breadth (see Chapter 2) and the distance between the forearm support and differential axis, while the link length, $L$, is approximately the distance from the distal wrist crease to the handle center. The review of anthropometric data provides bounds for for these quantities when the $1^{st}$ and $99^{th}$ percentiles are considered: $2.6 < L < 3.4$ and $\left(\frac{2.3}{2} + 1.36\right) < a < \left(\frac{3.0}{2} + 1.36\right)$, with all dimensions in inches. A kinematic analysis reveals the relationship between input and output angle as well as the transmission

[12]Namely, motions along the ADR and ADL axes.

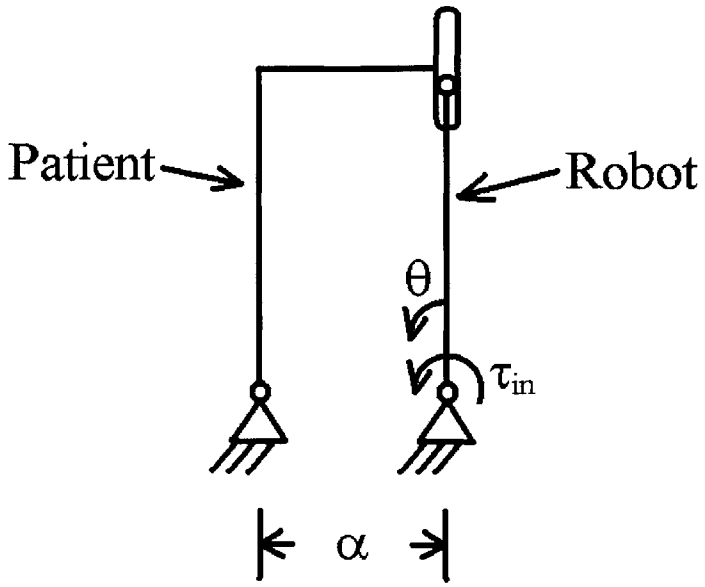


Figure 5-24: Model of mechanism for abduction/adduction [54].

ratio.

$$\tan\theta_{ad,h} = \frac{d\sin(\theta_{ad}+\beta) - a}{d\cos(\theta_{ad}+\beta)} \tag{5.6a}$$

$$d^2 = L^2 + a^2 \tag{5.6b}$$

$$\tan\beta = \frac{a}{L} \tag{5.6c}$$

where $d$ and $\beta$ are parameters defined for convenience as shown. The torque transmission ratio, $m_T = 1/m_V$, is then found by differentiating the position relationships.

$$m_T = \frac{d^2 + a^2 - 2da\sin(\theta_{ad}+\beta)}{d^2 - da\sin(\theta_{ad}+\beta)} \tag{5.7}$$

The output angle, $\theta_{ad,h}$, and the transmission ratio, $m_T$ are plotted as a function of the robot angle input in Figs. 5-25 and 5-26. Each relationship is plotted for five different patient sizes within the expected range. Here, the ratio of wrist breadth to $L$ is assumed constant and their values are chosen to be equally spaced within the range given above. Figure 5-25 shows that the input-output angle relationship

is nearly independent of patient size over the range of input angles shown. It is also worth noting that for $-5\,^\circ < \theta_{ad} < 5\,^\circ$, $\theta_{ad} \approx \theta_{ad,h}$. Outside of this range, the recorded robot data is not a good approximation of the hand angle. The transmission ratio, in Fig. 5-26, shows a greater dependence on patient size, especially for angles $\theta_{ad} > 5\,^\circ$. Still, the spread of the functions for output angle and transmission angle over varying patient size are small enough that meaningful data can still be extracted without knowledge of patient parameters.

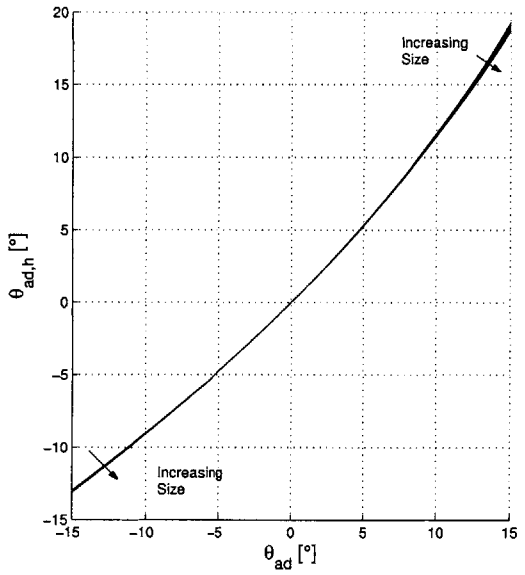


Figure 5-25: Input-output angle relationship for abduction/adduction mechanism. Curves are plotted for five different patient sizes within the expected range (direction of increasing patient size indicated by arrow).

In practice, DIFF operation is accomplished by specifying the stiffness (and damping) of the ADR and ADL motors. Figures 5-27 shows the effect of the differential transmission by assuming some stiffness $k = 5\,\frac{\text{Nm}}{\text{rad}}$ for each actuator (reflected out to the differential end gears) and examining the limits of torque and angle in all orientations if $\theta_R$ and $\theta_L$ are limited between -0.2 and 0.2 radians. The resulting diamond-shaped patterns are combined in Fig. 5-28 to show that the stiffness of the differential axes is independent of orientation[13]. The ADR and ADL actuators

[13]This analysis is not taking into account the handle analysis; the "differential stiffness" referred

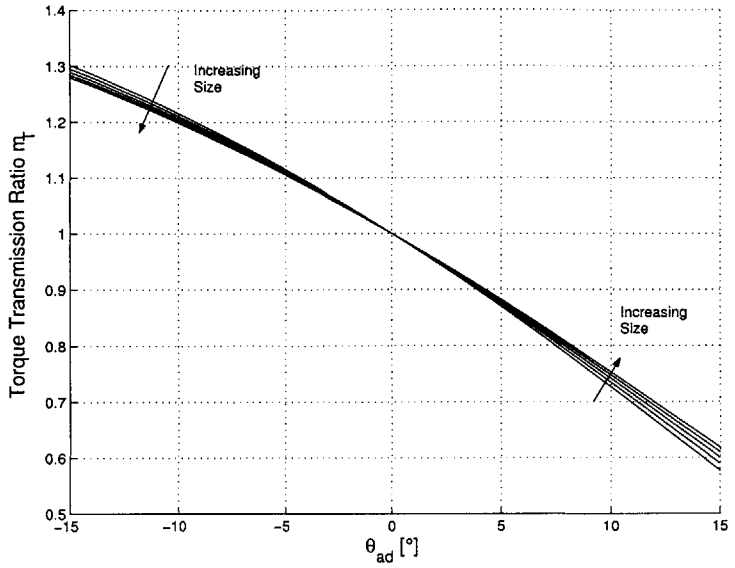


Figure 5-26: Transmission ratio for abduction/adduction mechanism. Curves are plotted for the same five patient positions shown in Fig. 5-25.

combine to give double the stiffness of either actuator.

## 5.5 Conclusions

A model competent to describe the encountered system behaviors has been developed. General operating characteristics involving positioning and force production were verified. Experiments were then conducted to find the parameters for the model. The model for each axis, based on the information gathered throughout Chapter 4, included the effects of inertia, stiction, viscous and Coulomb damping, gravity, and backlash. The basis for patient interaction is also discussed. The models developed are intended to be simple enough to work with, yet rich enough to describe the observed behavior of the system. In the next chapter, attempts are made to use these models to predict system stability and devise control methods.

---

to is for the robot.

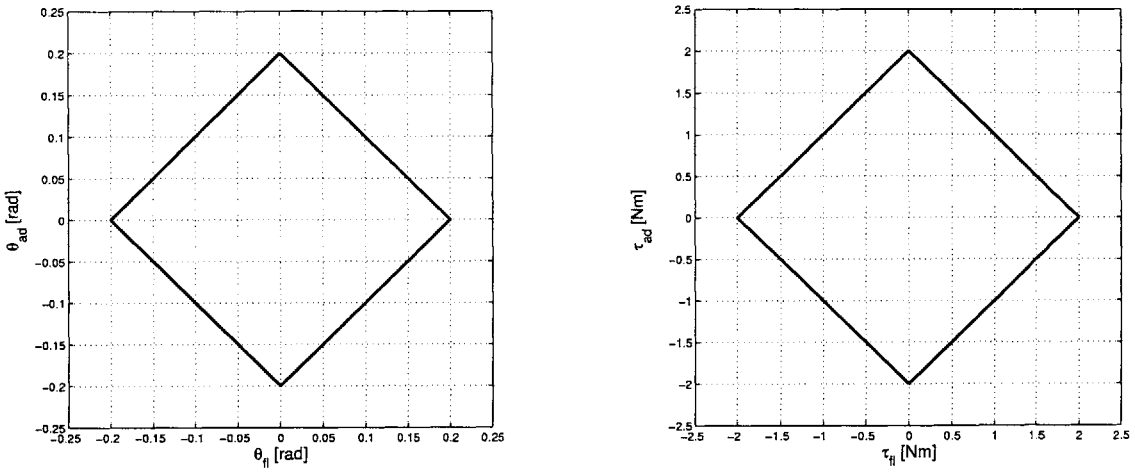


(a) Limited reachable workspace.

(b) Torque envelope.

Figure 5-27: Maps of angles and resulting torques for $\theta_R$ and $\theta_L$ limited between -0.2 and 0.2 rad. Torque is calculated using actuator stiffness $k = 5\frac{\text{Nm}}{\text{rad}}$.

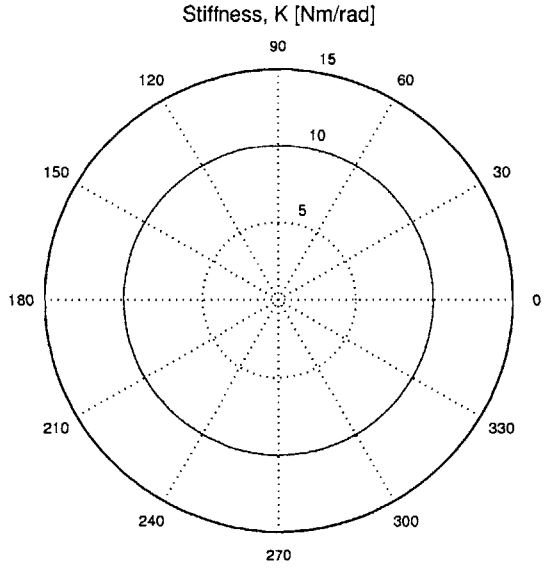


Figure 5-28: Endpoint stiffness combining the information from Figs. 5-27. Notice that $K = 2k = 10\frac{\text{Nm}}{\text{rad}}$.

# Chapter 6

# Stability and Control

With a model of the system behavior now in place, the goal is to provide the appropriate actuator commands in response to sensor inputs. In its most basic form, the controller should provide some desired stiffness and damping to some equilibrium point. The three main properties that are expected of this controller are that the resulting operation of the robot be smooth, stable, and isotropic. This chapter consists of a discussion of the attempts to provide such a controller and the known obstacles that remain.

## 6.1 Controller Requirements

Controller design is often posed as a trajectory or set-point tracking problem. Performance measures indicating the effectiveness of these types of controllers include steady state error, overshoot, and settling time. When used in therapy, this robot will be given a reference trajectory, but is required only to provide some predetermined environment (stiffness and damping) with respect to its equilibrium point. This section briefly discusses more appropriate controller requirements for this application.

The safe interaction between the robot and human demands assurance of stability. There are many types of stability that can be considered. For this device, "operational stability" will be considered violated for any unwanted system behavior. For example, the existence of stable limit cycles during operation will be considered "unstable" in

that their behavior is undesirable and disrupts the delivery of therapy. The patient must have confidence in the machine for its therapy to be effective. This will only be the case if the robot appears to be working, *i.e.*, it should operate smoothly and quietly. The stability limits of the device, as discussed in section 6.2, are an indication of the machine's effectiveness.

All perceived effects should be biological, not mechanical or otherwise hardware-related, in origin. In other words, robot operation, passive or otherwise, should be smooth. Smoothness can be classified as a stability concern as well, as the nonsmooth behavior encountered can be at least partially explained by stick-slip phenomena. More than just a functional asset, smooth operation goes a long way toward building patient confidence in the machine.

Defining the endpoint impedance at some equilibrium point must be meaningful throughout the workspace. Gravity has already been shown to influence the operation of the robot, especially in the PS axis. These position-dependent effects should be compensated for properly. The control strategy that is used in this chapter is one of specifying the joint impedances through proportional-plus-derivative control. This was partially done for simplicity, though it is somewhat justified based on the discussion of section 5.4 (see Eq. 5.5). For the movements being considered, joint control of the PS and flexion axes coincides with the endpoint impedances for PS and flexion quite well. Though not implemented here, an impedance controller could be readily designed based on the analysis of the abduction/adduction axis of section 5.4. Equation 5.7 giving $m_T = 1/m_V$ can be used to formulate the one-degree-of-freedom impedance controller as follows:

$$\tau_{ad} = m_T \tau_{ad,h} \tag{6.1a}$$

$$k_{ad}\theta_{ad} = m_T k_{ad,h}\theta_{ad,h}\left(\theta_{ad}\right) \tag{6.1b}$$

where $k_{ad}$ is the robot adduction stiffness, and $\theta_{ad,h}\left(\theta_{ad}\right)$ is given by Eq. 5.6, the forward kinematics of the mechanism. So, for some desired hand stiffness, $k_{ad,h}$ the

programmed robot stiffness in adduction/abduction will be a function of position:

$$k_{ad}\left(\theta_{ad}\right) = \frac{\partial}{\partial \theta_{ad}}\left(m_t k_{ad,h} \theta_{ad,h}\right) \tag{6.2}$$

From here, each actuator stiffness can be written in a form that can be implemented by the controller. The Jacobian transformation from joint coordinates to DIFF coordinates (from the discussion of section 3.4.3) is simply

$$J = \begin{bmatrix} 1 & 1 \\ 1 & -1 \end{bmatrix} \tag{6.3}$$

so that the actuator torques $\vec{\tau}_{act} = [\tau_R \ \tau_L]^T$ are given by

$$\vec{\tau}_{act} = J^T \vec{\tau}_{diff} \tag{6.4}$$

where $\vec{\tau}_{diff} = [\tau_{fl} \ \tau_{ad}]^T$, the torques on the robot arm. This derivation considers stiffness only, but could easily be extended to include damping. Specifying the actuator commands in this way should allow for the specification of an position-independent endpoint stiffness and may be implemented in the future.

The remainder of this chapter will cover some of the attempts at achieving these goals in the presence of the system properties and nonlinearities found in Chapter 5. The major difficulties all occur near the controller equilibrium point. At this point, torques due to the controller stiffness are comparable to those produced by the cogging map. In addition, it is within this region that difficulties with backlash occur. Finally, low-speed operation of the robot, which often occurs close to the controller equilibrium point, is hampered by friction (and cogging) effects.

## 6.2 Stability

Robot operating conditions will be limited to those for which the system is deemed stable. Blindly considering the maximum actuator output and the lowest perceivable

position change by the human provides an upper limit on the performance of the robot of 63.4$[\frac{\text{Nm}}{\text{rad}}]$ Even if stability issues did not preclude the attainment of this stiffness, it would still be slightly misleading, as actuator saturation would occur at small displacements. This robot has exhibited a number of behaviors that can be classified as unstable. The structural instabilities presented in Chapter 3 are not included in this discussion, as they cannot be influenced by the controller. These vibrations have been removed from the PS axis and have been deemed acceptably low for the DIFF axes. It is assumed that uncoupled stability will be more restrictive on the achievable gain set than coupled stability. Coupled stability refers to stability of the closed loop system including the robot and patient. While not guaranteed, it is expected that the load of the patient will add inertia and damping to the device, thereby acting as a stabilizer.

Testing for stability involved working with each axis and commanding the robot to some equilibrium position. The axis was then excited by hand in an attempt to induce some instability. Once deemed stable for this test, the same gain set was used with a series of step commands. Tests were terminated at any sign of instability, generally audible in nature. The test conditions were chosen by starting at a high damping, and incrementing the stiffness at that damping until the stability boundary was found. The damping was then decremented and the process was repeated. Two factors contributed to the difficulty in generating the stability maps of Figs. 6-1 and 6-2. First of all, there was initially some confusion during the discovery of the shaft deflection problems. These forced oscillations were originally attributed to to controller gain set, resulting in stability maps with poorly defined boundaries. The greater problem, however, has been exciting an instability.

Systems involving nonlinearities are difficult to analyze because they are not linear systems. This statement seems self-evident, but important nonetheless. All physical systems have some inherent nonlinearities, but systems involving hard nonlinearities, such as those present in the wrist robot, are especially difficult to linearize. This means that it is difficult to recast the dynamics into a form that can be easily solved for an arbitrary input condition. The stability of this robot has also been difficult to

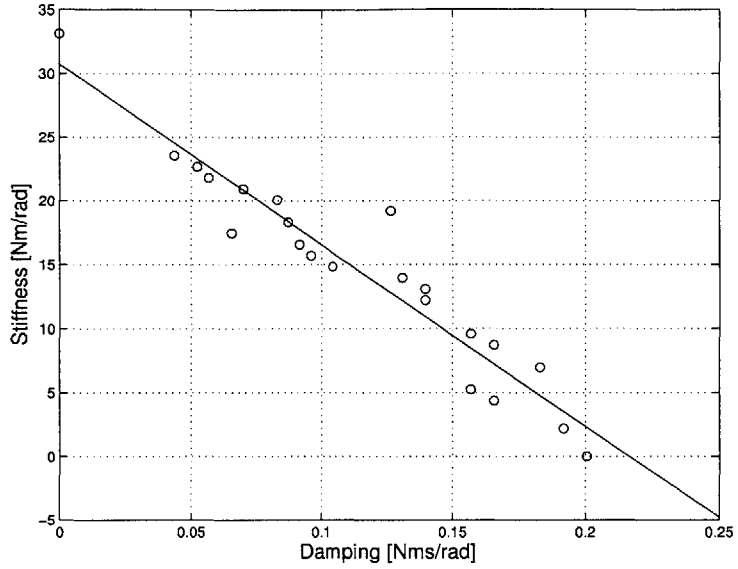


Figure 6-1: PS stability map with best-fit line. The region above the boundary formed by the data points is unstable

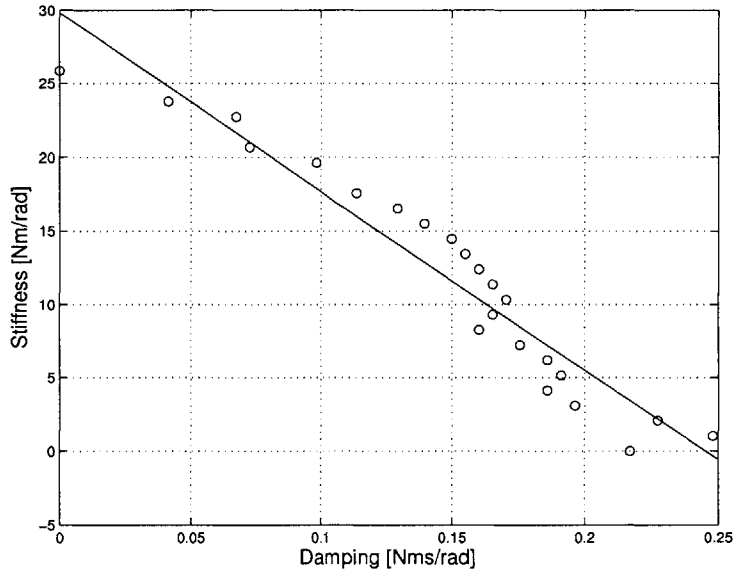


Figure 6-2: DIFF axes stability map with best-fit line. The region above the boundary formed by the data points is unstable.

quantify experimentally, due to difficulties in detection. Some situations are clearly unstable, as in Fig. 6-3, where the behavior of the machine is so immediately erratic that it cannot possibly be considered operational. Figure 6-4 shows an example of an instability that was difficult to discern during testing. Both test conditions involved only damping of the PS axis, but it was only after some provocation (actuating the system by hand) that the instability in Fig. 6-4 manifested itself. Because of these difficulties in determining stability, the value of the maps provided in Fig. 6-1 and 6-2 are somewhat questionable. Attempts were made to exhaustively test the potential for instability before implementing any gain set in the final robot games (introduced in Chapter 7).

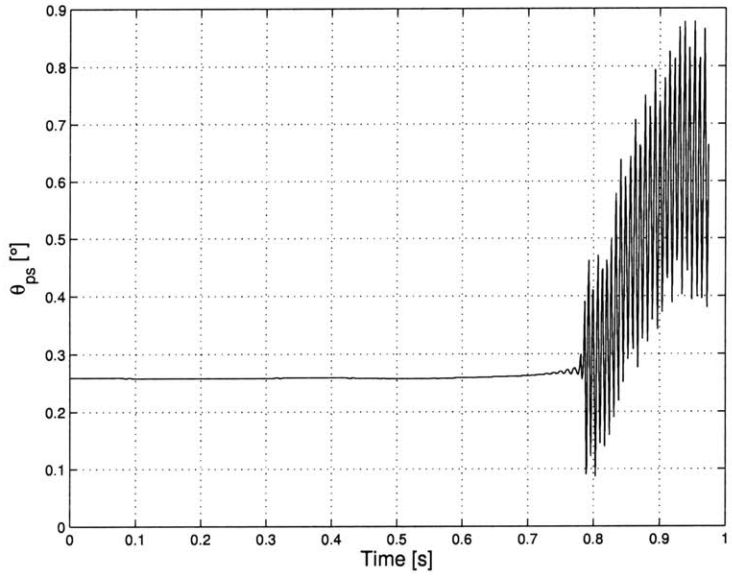


Figure 6-3: Results of a stability test with the PS axis. The controller is set with no stiffness and damping of $0.83\frac{\text{Nm s}}{\text{rad}}$. Instability occurred with no provocation.

The work done to derive the cause of instability from the models of Chapter 5 was incomplete at the time of printing of this document. The most likely candidate for instability is backlash. Empirically, it is known that stability problems only occur near the controller equilibrium point. In such situations, the actuator command is low and the pinion is in the backlash region. When the pinion disengages its mating gear, the dynamics describing its motion are altered (most significantly because of the

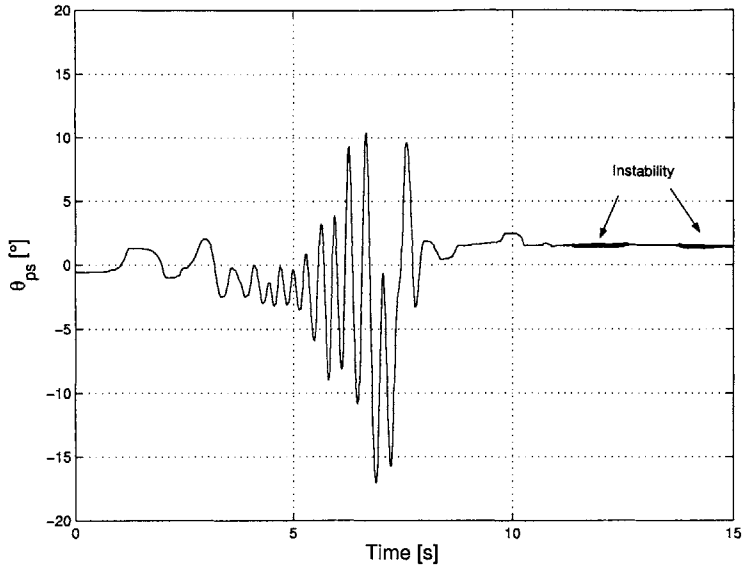


Figure 6-4: Results of a stability test with the PS axis. The controller is set with no stiffness and (endpoint) damping of $12.5 \cdot 10^{-3} \frac{\text{Nms}}{\text{rad}}$. Instability manifested itself after a long period of motion.

change in loading conditions). The exact nature of the resulting pinion and endpoint motion depends on whether the dynamics are dominated by friction or inertia. The dead-zone behavior of a system with backlash at torque reversals effectively places a delay into the system, a potential destabilizer.

Backlash, however, cannot explain the instabilities encountered in section 4.3, which occurred without any gears attached to the actuator. These, as stated in that section, are likely due to the effects of cogging. This is supported by the fact that there appears to be a lower limit for stiffness to achieve stable operation. The low gain limit is not shown on the plots of Figs. 6-1 and 6-2 as they were very difficult to locate precisely and not detrimental to system performance.

Figures 6-5 show the time response and phase diagram of an instability in the PS axis (under the same conditions as seen in Fig. 6-4. The trajectory in the phase plane shows convergence toward the final steady state oscillations. The instability pictured here was not easily discernable during testing due to its low amplitude. Limit cycles can be classified as either "soft self-excitation" or "hard self-excitation,"

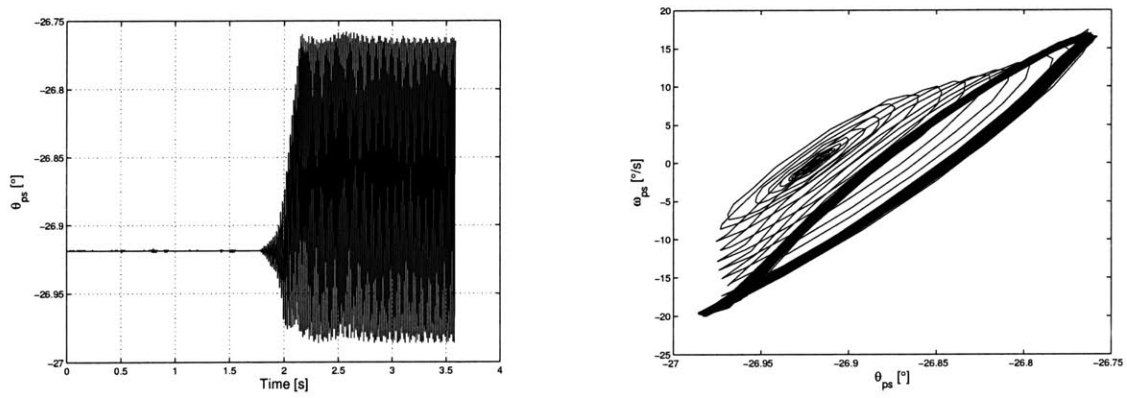


(a) Time response.

(b) Phase space diagram.

Figure 6-5: Results of an instability test with the PS axis. The controller is set with no stiffness and (endpoint) damping of $12.5 \cdot 10^{-3} \frac{\text{Nm s}}{\text{rad}}$. The instability was not apparent during testing due to the small amplitude of vibrations.

indicating how susceptible the system is to ending up exhibiting limit cycle behavior. Hard self-excitation systems depend on a specific set of conditions being present before entering a limit cycle [22]. This appears to be the case with the instability exhibited by the wrist robot, which is not consistently excitable. Full characterization of a nonlinear system requires testing and/or analysis over a broad range of input conditions. Quasi-linear methods exist to aid in the determination of conditions for stability analytically. Though not successfully applied here, describing function analysis offers such a method, based on a Fourier analysis of the nonlinearity and the assumption that the physical system (receiving the output of the nonlinearity as input) acts as a filter to higher frequency modes. This is one of many topics presented in this chapter that should be pursued in the future.

## 6.3 Compensation

### 6.3.1 Gravity

Gravity compensation figures most prominently in passive robot operation, when it is the most noticeable. The method used to compensate for gravity is to simply

command a torque equal in magnitude and opposite in direction to the expected gravity torque as predicted by the models of Chapter 5. Initially, the gravity-balancing torque produced by the DIFF actuators to counteract the load of the handle was made independent of the orientation of the DIFF axes. This form was chosen for its simplicity and effectiveness, since the load produced by the handle is reasonably independent of the orientation of the robot in the range of operation (see section 3.4.3). In the controller, this torque is modulated to account for changes in $\theta_{ps}$. When $\theta_{ps} = 0\,^{\circ}$, balancing the gravity torque requires commands that produce torque purely about the abduction/adduction axis, *i.e.*, $\tau_{fl} = 0$. Changing the orientation of the transmission housing requires the resolving of this torque into components so that

$$\tau_{ad} = mgl\,\cos\theta_{ps} \tag{6.5a}$$

$$\tau_{fl} = mgl\,\sin\theta_{ps} \tag{6.5b}$$

where $mg$ is the weight of the handle and $l$ is the moment arm of the handle, which has been approximated as a constant. This can be readily converted back into actuator torque requirements using Eqs. 3.6 to give

$$\tau_R = \frac{mgl}{2}\left(\cos\theta_{ps} + \sin\theta_{ps}\right) \tag{6.6a}$$

$$\tau_L = \frac{mgl}{2}\left(-\cos\theta_{ps} + \sin\theta_{ps}\right) \tag{6.6b}$$

Eventually, this compensation was updated to include the dependence of $mgl$ on $\theta_{ad}$, thus providing a more isotropic feel to the compensation. This was accomplished by considering Eqs. 5.4 and 5.7, giving the position dependence of the gravity load when the handle is fixed along the slider and the torque transmission ratio, respectively. The values for $mgl$ and $\beta_{ad}$ used were those found in the system identification. The final form of the DIFF gravity compensation is

$$\tau_R = \frac{m_T\, mgl\,\cos\left(\theta_{ad} + \beta_{ad}\right)}{2}\left(\cos\theta_{ps} + \sin\theta_{ps}\right) \tag{6.7a}$$

$$\tau_L = \frac{m_T\, mgl\, \cos\left(\theta_{ad} + \beta_{ad}\right)}{2}\left(-\cos\theta_{ps} + \sin\theta_{ps}\right) \tag{6.7b}$$

as shown in Fig. 6-6.

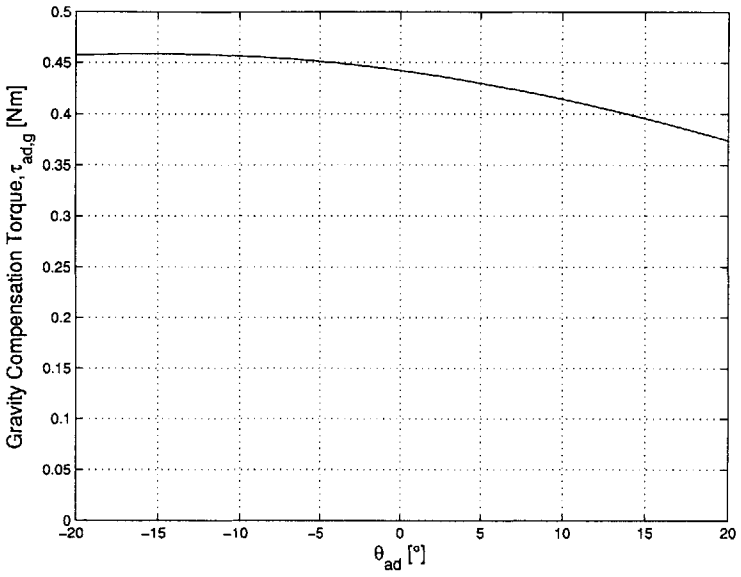


Figure 6-6: Gravity compensation command in the DIFF axis. This torque is provided by contributions from each of the DIFF actuators, the proportion of which is a function of $\theta_{ps}$.

The torque levels involved are fairly low (on the order of 0.03 Nm endpoint torque produced by each actuator) and could conceivably be ignored, yet they serve a more important purpose related to the smoothness of operation. Introducing a constant bias on each actuator forces the gears to one side of the backlash and provides a higher reference (than zero) to measure the cogging effects, both of which promote smoother operation. These points will be touched on in subsequent sections.

PS gravity compensation was also accomplished by simply adding the modeled form of the gravity load to the controller output. This effectively adds a spring with negative stiffness at the origin which is always stable as long as the gravitational load is still applied. Due to the influence of gravity, the commanded position does not coincide with the equilibrium point for a given time, a fact that will prove important in the backlash compensator development below. The equilibrium point is derived

by considering where the gravitational load as identified above is equilibrated by the command torque as follows:

$$\tau_c|_{\theta_{ps}=\theta^*_{ps}} + \tau_g|_{\theta_{ps}=\theta^*_{ps}} = 0 \tag{6.8a}$$

$$k\left(\theta_o - \theta^*_{ps}\right) + mgh\sin\theta^*_{ps} = 0 \tag{6.8b}$$

where $\tau_c$ is the commanded torque, $k$ is the commanded controller stiffness in $\left[\frac{\text{Nm}}{\text{rad}}\right]$, $\theta_o$ is the controller equilibrium point[1], and $\theta^*_{ps}$ is the apparent equilibrium point due to the effects of gravity. Linearizing so that $\tau_g = k_{lin}mgh\theta_{ps}$,

$$\theta^*_{ps} = \theta_o \frac{k}{k - mgh\,k_{lin}} \tag{6.9}$$

where $k_{lin}$ is the slope linearized version of $\sin\theta_{ps}$. The gravity term was linearized by finding the best-fit line using a least squares regression on the sin function over the range of $-50\,^\circ \leq \theta_{ps} \leq 50\,^\circ$, resulting in $k_{lin} = 0.926$ (for $\theta_{ps}$ in radians). Both the sinusoidal and linearized versions of this compensation were experimented with on the device and both were effective in relieving the user of the weight of the machine.

### 6.3.2 Friction

Ideally, the control strategy that is chosen will not limit the achievable endpoint impedance of the robot. When considering friction, specifically the stick-slip behavior noted in Chapter 5, it is sometimes useful to increase the controller damping to achieve a desired motion. This approach should be avoided with the wrist robot since it restricts the number of environments the robot can produce and is, in general, difficult to achieve (due to the limitations conveyed in the stability maps). One widely used method for overcoming stick-slip type phenomena is dither. The use of dither involves the superimposition of a high frequency, low amplitude signal to the control law. This is done to prevent the mechanism from being stopped by static

[1]Note that, in general, $\theta_o = \theta_o(t)$

friction. Trajectories in phase space at the application of a dither component will appear (nearly) vertical, setting the system onto a new trajectory as defined by the dynamics and eventually converging to the equilibrium point. This method would also be difficult to implement with the wrist robot due to the potential for exciting an instability. The idea of keeping the applied torque above the static friction value however, was explored.

There were two main attempts at friction compensation with the wrist robot. The first involved adding a constant-magnitude torque in the direction of the velocity. The noise involved in the method of measuring the velocity (a back difference of the position measurement) led to uncertainty in its sign at low velocity. In order to use this method stably, a threshold region around zero velocity had to be introduced in which the friction compensation was not added. In doing so, the purpose of introducing the compensation was negated; friction effects are the most detrimental to system operation at low velocities.

The second major friction compensation attempt aimed at sustaining torque commands above their static friction value. More specifically, a position-insensitive torque was applied near the controller equilibrium point to discourage the system from entering a pre-sliding regime. There are at least two major problems with this approach for this system: for one, this necessarily introduces a discontinuity in the torque command at the controller equilibrium point. This situation, akin to an infinite stiffness, is unstable considering the discussion of backlash in the previous section. The other problem, perhaps even more significant, is that this method did not result in smooth operation when applied. The nonsmooth behavior of the device has been modeled as an effect of friction, but the possibility that this characteristic is determined by cogging phenomena has not been eliminated. If this is the case, friction compensation will not be effective in compensating for the position dependent, spring-like behavior of the cogs. A feedforward cogging map was unsuccessful due to an inability to analytically describe the cogging. Recall from Chapter 4 that the cogging map is not necessarily a pure sinusoid. The results of Chapter 5 suggest that the combination of cogging and friction is very repeatable with position, suggesting that a

table-lookup could be implemented as a compensation technique. However, it is not a certainty that these characteristics will remain constant or repeatable, as there are time-dependent factors involved (especially with the friction due to wear in the gear teeth). This approach may be more feasible if the cogging had been characterized more fully using the method proposed in section 4.3 and may be revisited in future work. The problem of guaranteeing smooth operation remains a challenge in the design and control of this system.

### 6.3.3 Backlash

Backlash, while often necessary for gear train operation, has proved itself to be undesirable in this design. During normal operation, the robot is expected to make many torque reversals and, consequently, frequently traverse the backlash region. In order to avoid the instabilities encountered in section 6.2, the effects of this backlash should be compensated for. Doing so is limited by the system's sensing capabilities; there is no output shaft sensing. When not mechanically eliminated from the system, there are some backlash control methods in use. Among these are phase-lead compensators and adaptive techniques. In general, the adaptive techniques depend on defining a suitable backlash inverse or creating a backlash estimator. The implementation of these techniques depends on the backlash model used, of which there are quite a few. Besides the exact model of backlash seen in section 3.4.1, backlash can be modeled as a dead zone or as highly nonlinear spring with very low stiffness near the origin, just to name a few.

The major backlash compensation technique presented here is an attempt to simplify the problem. Its development involved as much art as science, accounting for its inability to suitably handle the problem. The idea for the technique originated with observations mentioned in section 6.3.1 that a constant torque bias improved the general feel of a gear set with backlash. If the pinions could always be pushed up against one side of their mating gears, the backlash region could be avoided. A region of torque-insensitivity, as proposed for friction compensation, could accomplish such a task. If the impact between the pinion and gear is ignored, this concept is

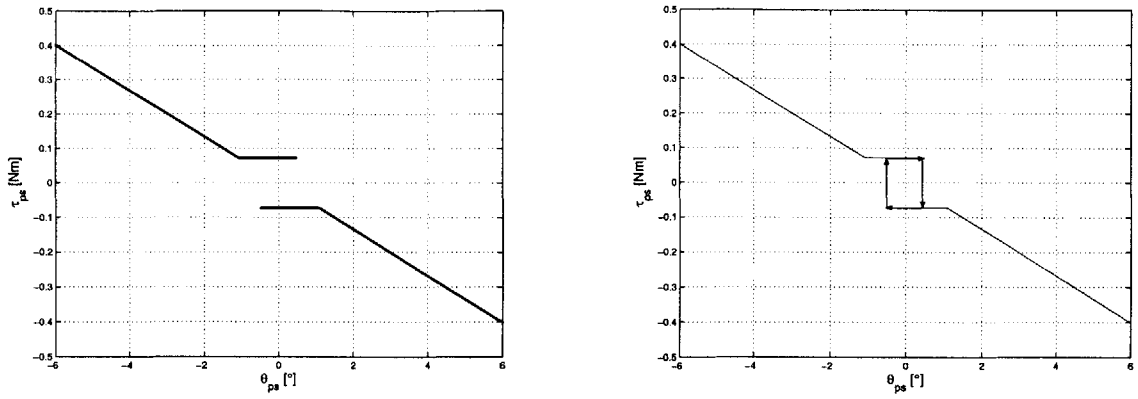


(a) Torque versus angle.

(b) Torque versus angle with hysteresis loop shown.

Figure 6-7: Hysteretic backlash compensator with controller equilibrium at a gravity neutral position.

much like a virtual anti-backlash system. At the time, it was though that this control scheme could simultaneously solve the problems with backlash and friction. The first problem with this concept has been covered in the previous section: the torque discontinuity at the controller equilibrium position. Figure 6-7 shows the proposed solution to this problem: the introduction of a toggle to the control law. The introduction of yet another nonlinearity to the system may not seem like a good idea at first, but consider that now the system cannot cross back and forth between positive and negative commands without moving some distance. The two levels of constant torque no longer create a discontinuity that looks like an infinite stiffness; there are now two steps in torque, separated by some distance.

Stepping the torque command in such a manner has not caused any problems with stability. The level of the constant torque was chosen so that it was high enough to keep the gears in contact at reasonable speeds, yet low enough so as not to move the coupled system (which could lead to new instability problems). The separation was chosen as the larger of the backlash and the distance between points where the controller command drops below the threshold and, in general, needs to be a function of stiffness. A flag is set in software to define whether the controller should be on the high side or the low side of the hysteretic loop, centered on the apparent

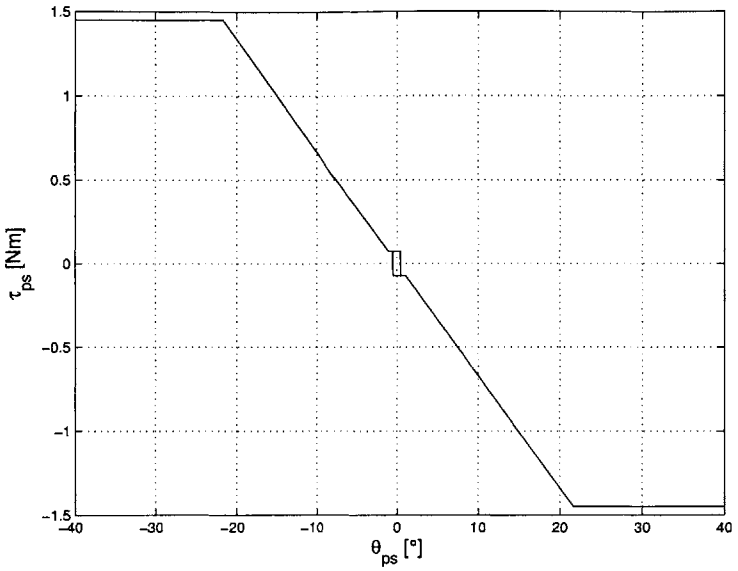


Figure 6-8: Torque versus position curve for control law showing actuator saturation.

controller equilibrium point, $\theta_{ps}^{*}$ (derived in section 6.3.1 as a consequence of gravity compensation). The flag is held in the "high" position (corresponding to the upper rung in Fig. 6-7(b)) until the position is greater than the equilibrium position by more than the threshold, at which point it switches to the bottom rung. The control law remains on this bottom rung (with the flag set to "low") until the position is less than the equilibrium position less the threshold.

Figure 6-9 shows the position response using this backlash compensator for a sinusoidal reference trajectory. The resulting motion appears to have the same problems exhibited by the standard PD control of the device, namely the nonsmooth behavior. That in and of itself would support using the compensation, as the achievable stiffness has increased. Figures 6-10 through 6-12, however, show why this technique cannot be used. When moving with gravity (toward a gravity-neutral position), the control law switches undesirably. Consider the closeup of the position response of Fig. 6-10, which is typical of movements toward the neutral position (when the the position is in between the controller equilibrium point, $\theta_o$, and the zero command torque point, $\theta_{ps}^{*}$). This is due to the pinion remaining stationary while the equilibrium point moves past it. Once the difference between the controller equilibrium point and the pinion

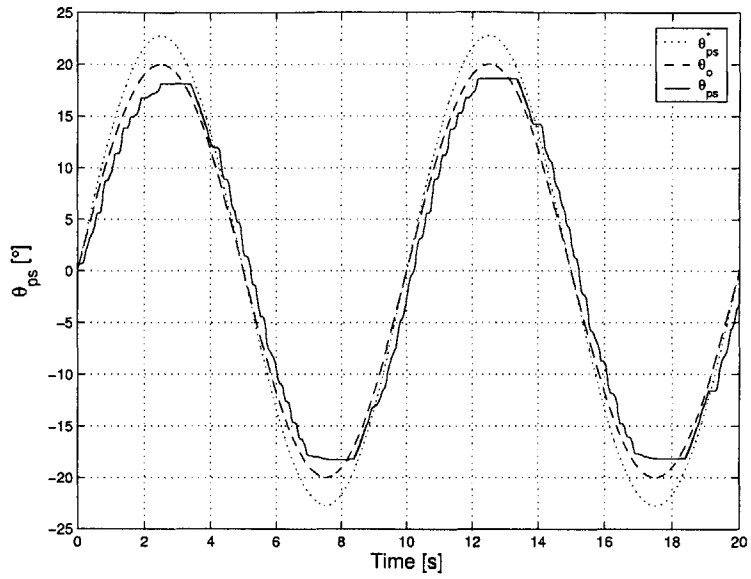


Figure 6-9: Position response to a sinusoidal input using backlash compensation. The controller equilibrium point, $\theta_o$, and zero command point, $\theta^*_{ps}$ are also plotted.

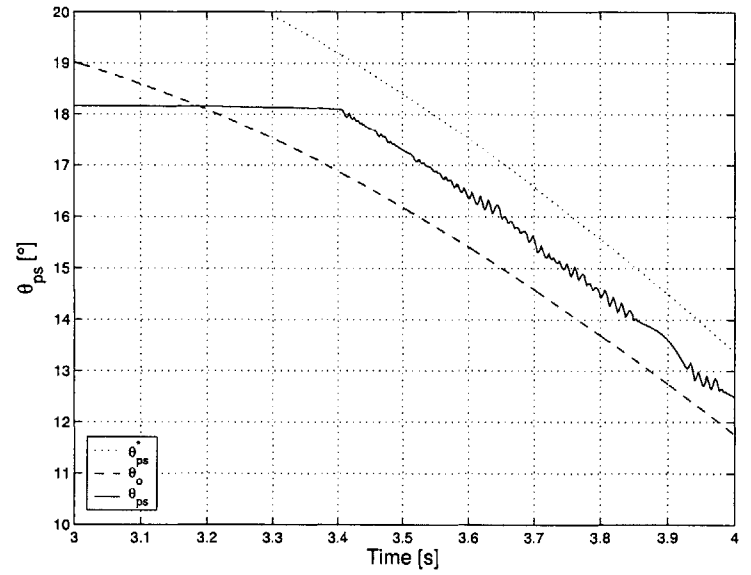


Figure 6-10: Closeup of position response to a sinusoidal input using backlash compensation. The response shown is typical of movements toward the neutral position.

position is greater than the threshold, the pinion switches to the other side of its gear and initiates movement of the transmission housing. If the pinion moves far enough to cross the other threshold, the level of the command torque switches again, allowing the process to repeat. The resulting operation creates some noise and is generally unsatisfactory. When coupled to a human, the control law does its job properly, but this operation cannot be guaranteed.

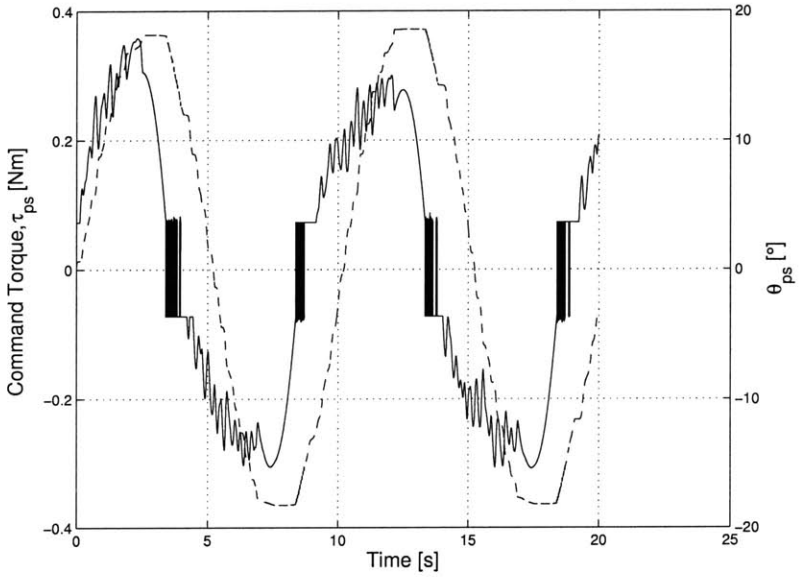


Figure 6-11: Backlash compensator command torque along with position response. The dashed line is the position response, using the right y-axis, while the solid line is the command torque, using the left y-axis. The plot shows that, when moving with gravity, the control law switches undesirably, accounting for the position response seen in Fig. 6-10.

While this controller seems to work well for a stationary equilibrium point and even a moving equilibrium point when coupled to a human, its inability to operate smoothly very close to a moving equilibrium point makes it unusable in its current form. Attempts to shape the hysteresis loop to avoid regions where the performance degrades as discussed have as yet been unsuccessful. Investigation of a similar technique with the DIFF axes was abandoned in light of the difficulties with the PS axis. The next step in controller design should follow closely the established literature on backlash control. The use of model-referenced adaptive controllers may allow the

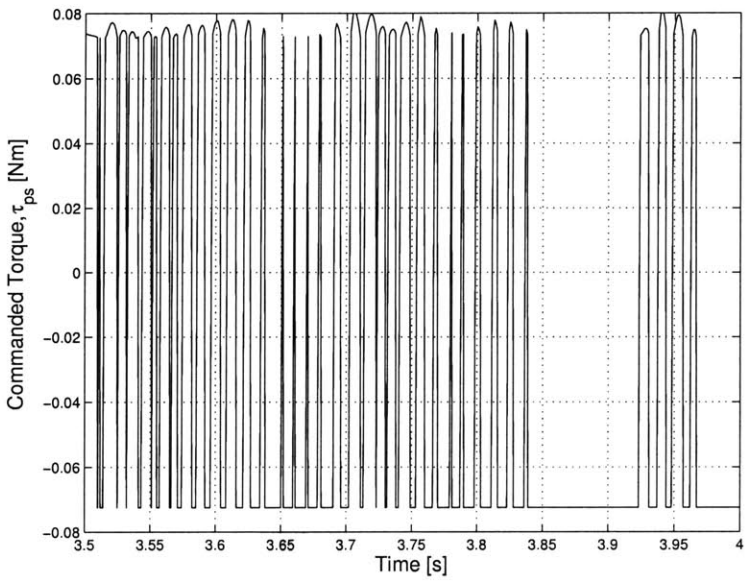


Figure 6-12: Closeup of backlash compensator actuator command. In this figure, the pinion remains below the zero command point (*cf.* Fig. 6-10) so that the nominal command is always above zero. When the backlash compensator is applied, the actual command must be either above 0.725 Nm or below -0.725 Nm.

design of systems that behave according to the desired model (in this case, an endpoint that behaves like a damped spring) while compensating for the effects of the nonlinearities behind the scenes.

## 6.4 Controller Conclusions

This chapter has focused on the characterization of the achievable impedances of the wrist robot under PD control. The desired motion profile, the reference for the controller, is developed in Chapter 7 along with interactive video games for therapy. Therapy requires that the device should be predictably stable under all operating conditions and should operate smoothly when recreating therapy environments. The task of providing a suitable endpoint impedance for the robot is complicated by the presence of both hard and soft nonlinearities in the device. Specifically, the presence of backlash and motor cogging give rise to situations in which stable limit cycles can develop. In order to avoid these situations, limits must be placed on the controller

stiffness and damping. Stability was tested over a broad range of impedances, but the prevalence of so-called "hard self-excitation" limit cycles has hampered the accurate characterization of the operational limits of the device.

The current implementation of the controller is a joint based PD controller on each axis with gravity compensation. Gravity compensation in the PS axis is accomplished by supplying a command to counteract the load, which behaves like a spring at $\theta_{ps} = 0\,^{\circ}$. In the DIFF axes, the gravity compensation was simplified to a constant command to each actuator, modulated only by the PS position. This was initially done to account for the uncertainty in the location of the handle due to the slider, but, since that kinematic relationship is well-defined (see section 5.4) and variations due to patient size are rather small, this was adjusted to include an adduction orientation dependence. As it stands, even a constant force contributes to the smoothness of the DIFF axes during passive robot operation, as the gears are forced to one side of the backlash.

A simple method for counteracting the effects of backlash and friction simultaneously without limiting the range of impedance was introduced in this chapter, but not successfully implemented. The basic concept was to introduce a hysteretic toggle, yet another nonlinearity to the system, so that at the command always stays above some threshold level and a virtual anti-backlash system is applied to the gears. The threshold is meant to be above the static friction level to keep the device out of the pre-sliding regime. By creating a region of torque insensitivity at low commands and separating the transitions between positive and negative commands, the controller behaves as if there is a discontinuous torque at the transition (rather than an infinite stiffness). Smooth operation remains challenged by the cogging characteristics of the actuators, which are not easily described in a functional form. Currently, efforts involve employing the model developed in Chapter 5 to gain a better understanding of the instability encountered and aid in the controller development.

# Chapter 7

# Robotic Therapy

The discussion now returns to this machine's intended purpose: as a robotic wrist rehabilitator. Following in the footsteps of MIT-MANUS, this robot will engage the patient through a series of interactive video games. Therapist duties will include indexing the robot and ensuring that the patient is seated at the device properly before overseeing therapy. General robot operation is described in the User Manual, Appendix D of this thesis.

One of the long term goals of therapy implementation with this robot is to execute activities that mimic functional tasks, such as those depicted in Fig. 7-1. Based on the discussion of Chapter 2, the ability to complete a specific task is improved by practicing that task. Early clinical trials will instead focus on gross motions of the wrist and forearm. Therapy will still be goal-directed, but the goal is the movement itself with no other "real world" context provided. This approach is compatible with the current capabilities of the hardware and simplifies the specification of desired environments/trajectories. Concentrating on providing a working prototype to the clinic allows the development of long term goals to be influenced by the initial results.

In order to deliver therapy, the system must successfully convey the desired motion through visual cues. The actuators provide the corresponding assistance (or resistance) to emulate the therapy environment. The robotic therapy introduced here mainly consists of robot-assisted point-to-point movements using a simplified display and the controllers from the previous chapter.

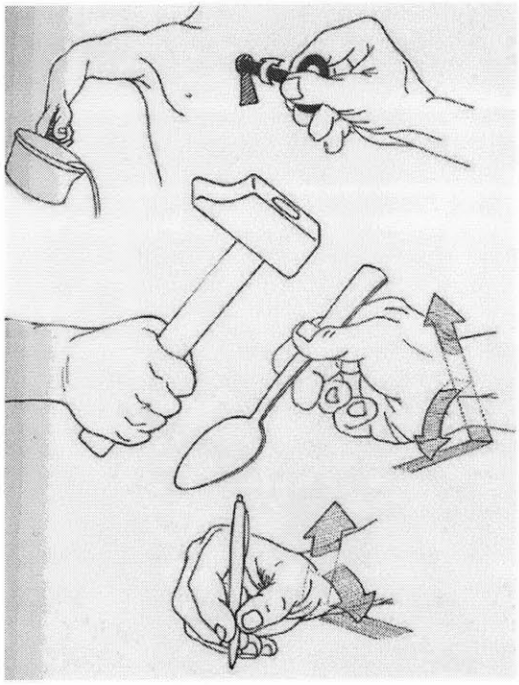

Figure 7-1: Some functional wrist and forearm tasks [31].

## 7.1 Visual Display

To date, communication between the robot-therapist and patient has been accomplished through a series of interactive video-games. The displays developed for this device must convey three rotational degrees of freedom onto the monitor. The tools used were part of the QNX packages already in the robot libraries, capable of producing lines and ellipses along with providing color manipulation. The basic requirement for the visual display is that it accurately and logically represent the position of the end effector in the workspace. There are concerns over whether stroke patients will be capable of understanding the abstract representation of their own wrist motions on a two-dimensional screen, especially in light of possible cognitive deficits. Those same concerns present themselves when considering the use of perspective in the rendering of three-dimensional images on a screen. The development of a basic display that properly interfaces with the controller software is discussed here, with further development and evaluation of advanced display methods deferred to the future.

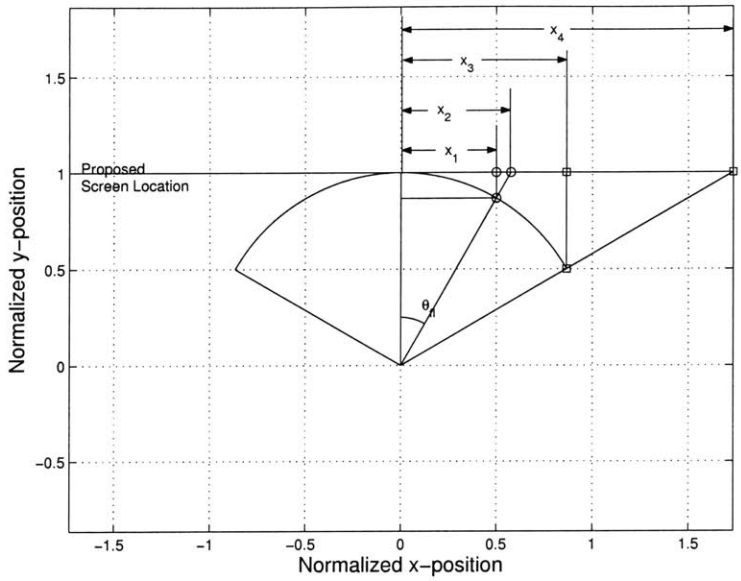


Figure 7-2: Diagram indicating the process used to create a screen representation of the cursor. Flexion is shown, though the formulation for abduction is identical. The circles represent $\theta_{fl} = 30\,^\circ$ while the squares represent $\theta_{fl} = 60\,^\circ$. Using the 'sine' formulation gives points $x_1$ and $x_3$ as screen representations, while using a 'tangent' formulation would give points $x_2$ and $x_4$.

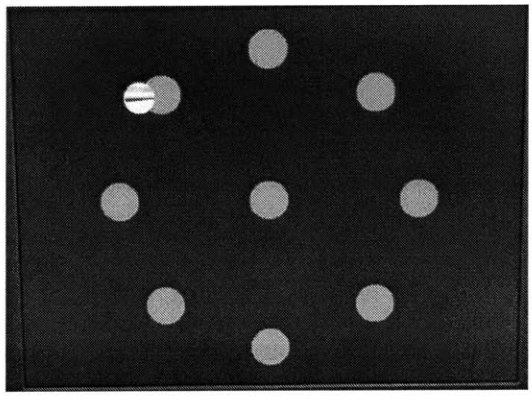

Figure 7-3: Initial video game display. The cursor location represents the wrist orientation while the black line on the cursor represents the PS orientation.

The endpoint of the robot is represented on-screen by a circular, yellow cursor. There is a one-to-one mapping of the $(x, y)$ position of the cursor on the screen to the latitude and longitude of the robot arm, $(\theta_{fl}, \theta_{ad})$. Equations 3.5 give the basic relationship between motor angles and handle orientation. The paradigm employed for the display is to assume that the patient is pointing at the inside of a sphere. That point is then projected (from behind) onto a screen some distance $l_{scr}$ away. The position on the screen is then given by

$$x = -l_{scr} \sin \theta_{fl} \tag{7.1a}$$

$$y = l_{scr} \sin \theta_{ad} \tag{7.1b}$$

where the negative sign in the equation for $x$ indicates that the mirror image is displayed on the screen. PS motion is conveyed through the orientation of a bar on the cursor. Figure 7-2 shows how using a 'sine' formulation rather than one involving the tangent of the angle scales the position so that changes in angle at large angles result in smaller changes in screen position. The original implementation of this display included scaling factors to normalize the ranges of motion of wrist rotation[1]. This led to the introduction of the circular set of targets shown in Fig. 7-3, reminiscent of the visual display used with MIT-MANUS. The horizontal black line seen on the cursor in Fig. 7-3 rotates during pronation/supination so that all three robot degrees of freedom are mapped onto the screen.

The current wrist robot displays are shown in Figs. 7-4. Scaling the wrist dimensions added an extra, unnecessary level of abstraction between wrist motion and cursor motion that was deemed undesirable. Removing these factors in favor of a direct application of Eqs. 7.1a is less limiting in terms of conveying the different ranges of motion in each direction. This approach was chosen over other candidate representations so that the aspect ratio of the workspace would be more appropriate for the shape of the screen while preserving the proportions between flexion and ab-

[1]Recall that the range of motion for the robot is greater in flexion/extension than in abduction/adduction.

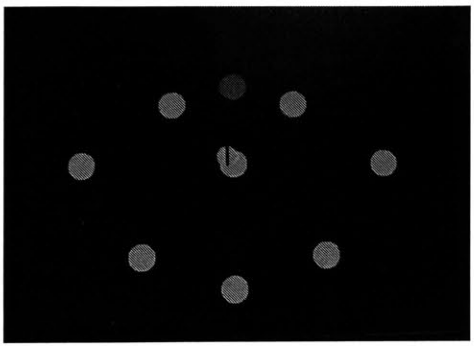

(a) Basic display for wrist games.

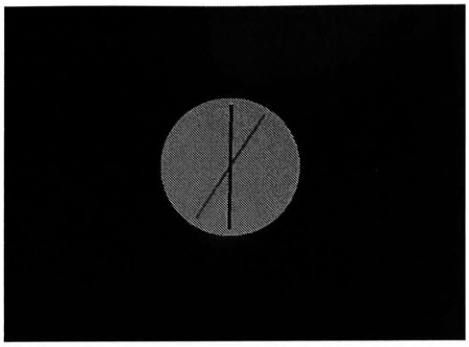

(b) Display for PS mode.

Figure 7-4: Visual display types.

duction movements. It would have been possible, for example, to use the joint-space coordinates of the robot as its position on-screen, as in Fig. 7-5. Doing so, however, would require the targets to be spaced close together in the vertical direction, while far apart in the horizontal direction.

Target locations were chosen qualitatively, erring on the conservative side, to provide useful therapy games. Figure 7-5 shows the target locations in DIFF coordinates[2]. Since the circular pattern of targets is not used, the targets are not required to lie on an ellipse in joint-space. The abduction target length is less than the adduction target length, as required by the biology. The adduction length was chosen to avoid the mechanical limit stop in that direction, though future versions of the device should accommodate more adduction. The flexion and extension targets were chosen to approach a comfortable[3] wrist extension position[4]. The combination movements, chosen along the axes of the ADR and ADL motors, were also chosen according to feel. Information gathered during clinical use of the robot will assist in determining the best target lengths to use.

The PS representation was adjusted, based on therapist recommendation, so that

[2]The target locations of Fig. 7-4(a) and Fig. 7-5 are not exactly the same; Fig. 7-5 represents the latest set of target locations.

[3]as judged by the author

[4]Since the handedness of the patient determines which side of the robot corresponds to flexion as opposed to extension, extension movements must be taken as the limiting factor. This is mainly because maintaining the "neutral" handle position requires the patient to extend his wrist.

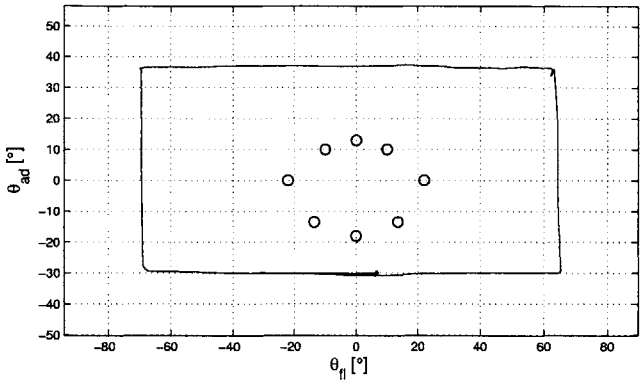


Figure 7-5: Current target locations in DIFF space. The rectangular outline represents the extents of the robot workspace.

the neutral position of the robot would correspond to a vertical bar. In other words, the orientation of the line on the cursor now represents the orientation of the handle. Games that only involve PS motion dispense with the moving cursor, as seen in Fig. 7-4(b), increasing the emphasis on forearm rotation.

## 7.2 Video Games

Now that the patient can receive visual feedback, interactive routines for therapy must be established. While the usefulness of the robot is based on the effectiveness of the control algorithm, the game development and controller development are largely independent[5]. The programs, written mainly in C/C++, are executed on the QNX 4.24 operating system in an XWindows environment. The monitor program updates at a rate of 60 Hz, higher than the 24 Hz required for human persistence of vision to give the illusion of continuous motion. Visual cues are given to the patient by changing the color of the targets. In keeping with convention used in the MANUS games, light blue indicates an inactive target, red indicates an active target, and dark blue indicates that the cursor should be held at the specified target.

[5]Of course, controller performance measures are often based on properties of the task and more complex tasks may require more complex controllers. This statement is only meant to imply that the controller for a given therapy task is not a unique one.

Data from each game is stored in a binary file containing a recording of each robot state for every sample period[6]. There are nine robot states included in every data file, the descriptions of which are given below.

**State 1: Flexion Angle** Robot arm flexion angle in [°], nominally equivalent to the patient flexion angle. Positive readings correspond to flexion for a right-handed patient and extension for a left-handed patient.

**State 2: Abduction Angle** Robot abduction angle in [°], distinct from patient abduction angle. The exact relationship between the degree of robot abduction and the degree of patient radial/ulnar deviation depends on the individual patient geometry (see section 5.4). Positive values are always indicative of radial deviation, regardless of which hand is used.

**State 3: PS Angle** The PS orientation of the robot in [°]. While the amount of forearm rotation is roughly equivalent to the PS angle indicated by the robot, patient orientation with respect to the device must always be considered in interpreting the results. Supination is a positive reading for right-handed patients and negative for left handed patients.

**State 4: Flexion Velocity** Time rate of change of state 1 in $[\frac{\circ}{s}]$ computed using a filtered back-difference[7].

**State 5: Abduction Velocity** Time rate of change of state 2 in $[\frac{\circ}{s}]$ computed using a filtered back-difference.

**State 6: PS Velocity** Time rate of change of state 3 in $[\frac{\circ}{s}]$ computed using a filtered back-difference.

**State 7: Commanded Flexion Torque** The commanded torque about the flexion axis in [Nm] computed by scaling the voltage command according to known

[6]Unless otherwise noted, games are sampled at 1 kHz.
[7]Velocity calculation is discussed in Appendix B.

calibration factors. This value is nominally equal to the commanded torque about the patient flexion/extension axis.

**State 8: Commanded Abduction Torque** The commanded torque about the robot abduction/adduction axis in [Nm] computed by scaling the voltage command according to known calibration factors. This value, like state 2 is related to the corresponding patient variable through geometry.

**State 9: Commanded PS Torque** The commanded torque about the pronation/supination axis in [Nm], roughly equivalent to the commanded torque imparted to the patient in forearm rotation (see section 5.4). It is computed by scaling the corresponding command voltage by known calibration factors.

The basic game is a record and playback game. The patient is allowed to move around the basic display while the robot operates in a passive mode, *i.e.*, gravity compensation for the weight of the device is provided. This file can be replayed by the actuators with the playback game. Recording capabilities can be useful in the evaluation of patient range of motion. Other potential uses include therapy involving some irregular, therapist defined trajectory. Record and playback eliminate the need for an analytically defined desired trajectory. It is worth noting that these games are sampled at 200 Hz to accommodate the system's need to read from and write to files during operation. In addition to the record and playback games, the robot is equipped with a number of games appropriate for strength and resistance training, described in the remaining sections of this chapter.

### 7.2.1 Resistance Games

The first set of games command the robot to hold a position in the center of the workspace. Visual cues prompt the patient to move toward the targets so that the actuators oppose the motion of the patient. In essence, the robot is commanded to behave as a damped spring centered at the center of the workspace. Two versions of the game exist: one for wrist movements using the basic display if Fig. 7-4(a), and

| Setting | DIFF Axis Values | | PS Axis Values | |
|---|---|---|---|---|
| | Stiffness $[\frac{\text{Nm}}{\text{rad}}]$ | Damping $[\frac{\text{Nms}}{\text{rad}}]$ | Stiffness $[\frac{\text{Nm}}{\text{rad}}]$ | Damping $[\frac{\text{Nms}}{\text{rad}}]$ |
| "Soft" | 2.44 | 0.05 | 2.21 | 0.0315 |
| "Medium" | 4.88 | 0.03 | 4.41 | 0.0315 |
| "Stiff" | 9.8 | 0.02 | 8.72 | 0.0179 |
| "Unassisted" | GRAVITY COMPENSATION, $k = b = 0$ | | | |

Table 7.1: Current settings in game software. The therapist is prompted with a menu of the setting descriptions in column one.

one for forearm movements using the PS display of Fig. 7-4(b). Return moves can be viewed as a kind of negative resistance game during which the patient must control his motion as the robot is forcing it along the same trajectory. All of the active games currently have three preset stiffness/damping combinations for the therapist to choose at the beginning of the game. Table 7.1 summarizes these values, which are presented to the therapist as either "soft," "medium," or "stiff." This is done as a safety precaution against unsafe gain selection. After some testing, it is anticipated that the appropriate gains for therapeutic application (within the constraints of the device) will be identified and implemented.

### 7.2.2 Sensorimotor Games

#### Star

One of the major advantages of MIT-MANUS has been its ability to provide sensorimotor training; visual feedback prompts the user to make a specified movement, which is assisted by the robot. The `star` game accomplishes this task with the wrist robot. This game involves the DIFF display of Fig. 7-4(a). To set up the game, the PS axis is set to either "medium" stiffness and held at neutral or to "unassisted" mode. During the game, the patient is prompted to move to and from the targets as the colors of the targets change. As discussed in section 2.3, the nature of human wrist movement is not yet well understood. Through experimentation with this device, more insight may be gained into this field, but for now, a therapy protocol must

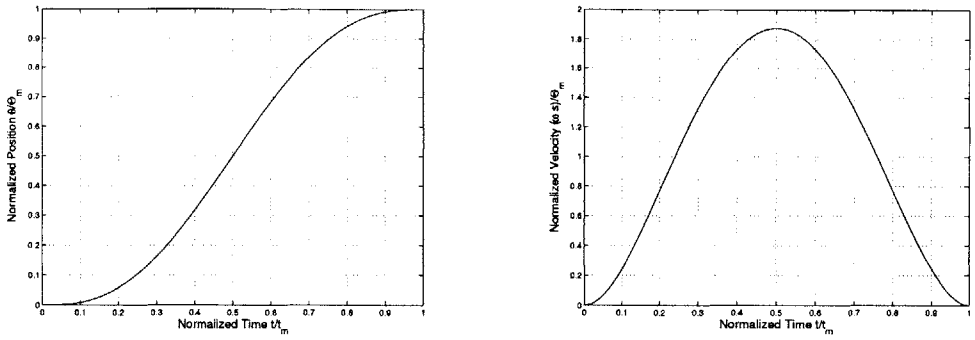


(a) Position profile.

(b) Velocity profile.

Figure 7-6: Normalized minimum-jerk profiles.

be established. The initial approach here is to suggest (through the controller) that the patient make minimum-jerk movements between targets. The most convenient way to do this is to consider a single-degree-of-freedom minimum-jerk profile[8], given by

$$\theta(\tilde{t}) = \Theta_m \left(10\,\tilde{t}^3 - 15\,\tilde{t}^4 + 6\,\tilde{t}^5\right) \tag{7.2a}$$

$$\dot{\theta}(\tilde{t}) = \frac{\Theta_m}{t_m} \left(30\,\tilde{t}^2 - 60\,\tilde{t}^3 + 30\,\tilde{t}^4\right) \tag{7.2b}$$

where $\Theta_m$ is the total angular excursion of the move, $\tilde{t}$ is the normalized time, and $t_m$ is the time allotted for the move. Figures 7-6 plot normalized position and velocity profiles for a point-to-point minimum-jerk movement.

The equilibrium point trajectory is not displayed on the screen; only the start and end targets are indicated on-screen. Stiffness can be set according to Table 7.1 for the DIFF axes and to either "medium" stiffness or "unassisted" mode for the PS axis. Figure 7-7 shows a test run of this game by the author attempting the moves with a moderate grip on the handle.

### PS Sweep

The `pssweep` game, using the PS display mode, presents the patient with a line target that moves with a sinusoidal trajectory. For the inactive axes (the DIFF axes) the

[8]See Appendix B for a brief introduction to this topic.

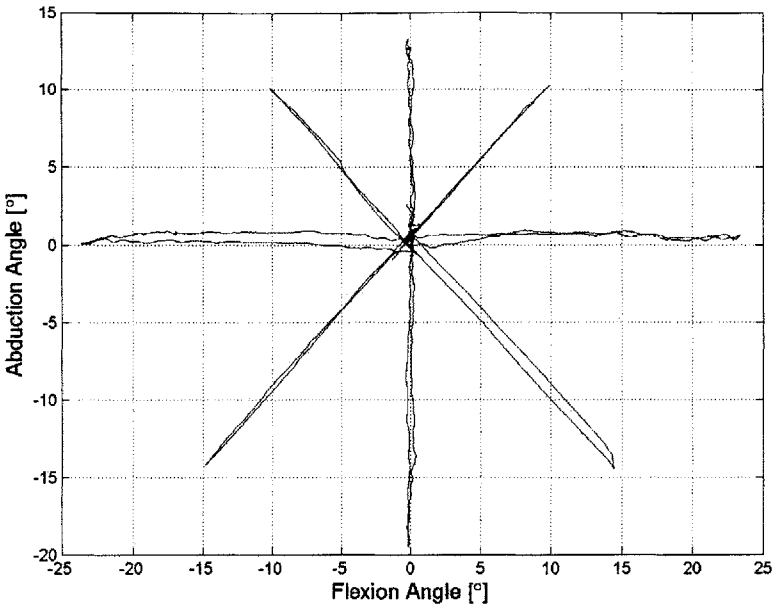


Figure 7-7: Sample test data from `star` game with the author.

therapist has the choice of setting them to "medium" stiffness or to unassisted mode. The patient is asked to follow the trajectory on the screen. When the patient is close enough to the target, the background will change from yellow to green. Game parameters like the number of periods, the total angular excursion, and the frequency of the sweep, currently hard-coded into the program, can be adjusted as necessary in the future. The current settings are for a 0.075 Hz sine wave swept with an amplitude of 35 °. Figure 7-8 shows the position response for a test run of this game by the author. The stiffness is set to "medium" and the subject is allowing the robot to lead the move.

### PS Target

The `pstarget` game is similar to `pssweep` except that, instead of sinusoidally sweeping through the desired range of motion, discrete target positions are given. The desired path of the controller consists of minimum-jerk movements between targets for the PS axis. The current robot settings specify 8 targets (4 on either side of the neutral

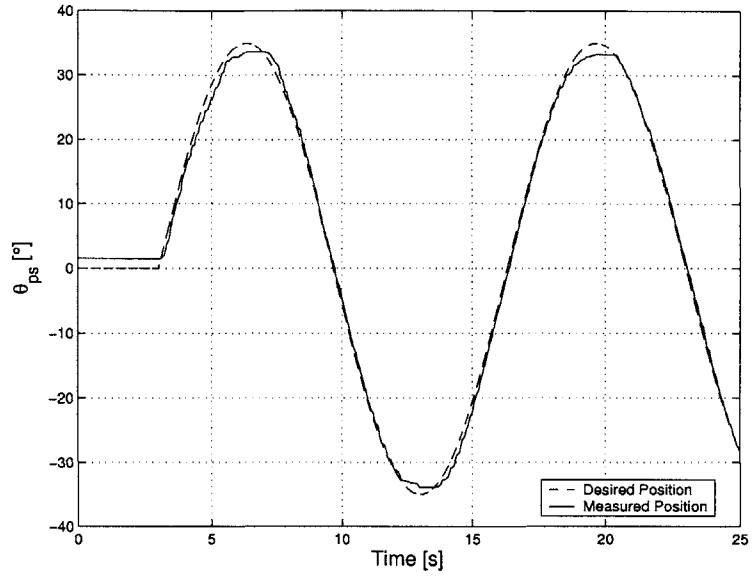


Figure 7-8: Data from test run of PS sweep game by author. Subject is allowing the robot to lead the motion, with the stiffness set to "medium."

position) at increments of 8 ° away from neutral. The two PS games mentioned do not take into account what hand the patient uses. The importance of patient positioning with regard to PS motion has already been discussed and may necessitate coding separate programs for right and left handed robot usage.

### 7.2.3 Strength Training Games

Each of the movement therapy games described above can also be used as a strength training game. The therapist can instruct the patient to hold the handle in the center. The game controller will attempt to move the patient toward the targets. By resisting the forces exerted by the robot, strength training therapy is accomplished.

### 7.2.4 Partial-Assist Games

The games described above set an equilibrium point for the robot. If the patient moves ahead of the prescribed trajectory, he will be forced back. In order to allow the patient to move ahead of the robot without penalty, the `star` and `pstarget` games

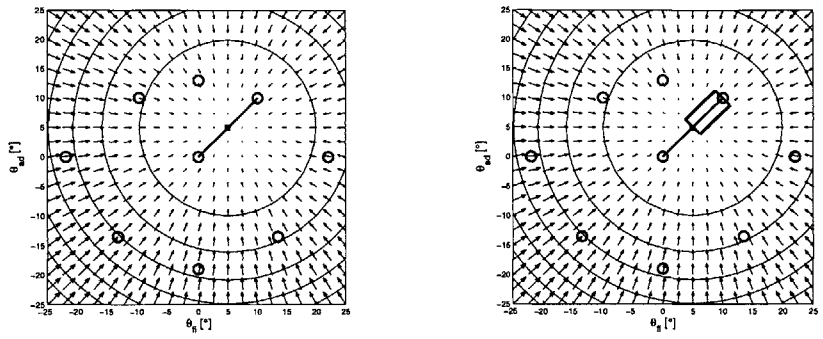

(a) Star game with equilibrium point shown.

(b) Partial assist star game torque field for same equilibrium point.

Figure 7-9: Diagrammatic representation of the effect of partial assist star game.

were modified. In the modified **star** game, the patient is still asked to move from target to target, but the robot switches from an active (assist) to a passive mode if the patient moves between the equilibrium point and the target location. In terms of the visual display, this area can be thought of as a box with some specified thickness and some time-dependent length. Figures 7-9 offer a diagrammatic representation of this concept; the initial star controller sets up a torque field about the equilibrium point as shown in Fig. 7-9(a). For the partial assist game, Fig. 7-9(b), this field is turned off within the rectangle in joint space existing between the equilibrium point and the target location. The partial assist version of the **pstarget** game is similar except for the fact that it is only one dimensional.

Due to the fact that this controller defines an assisted region and an unassisted region, there is necessarily a boundary between the two types of assistance. At this boundary, where the control law switches, the controller appears to have infinite gain. High gains, especially when passing through zero command, were covered as a source of instability in Chapter 6. In order to counteract these instabilities, the control law was augmented to include a transition region between the two modes of operation. With the control law defined as a piecewise linear function of position at any instant in time, the instability should be avoidable. At the present time, this instability has not been overcome; the system goes into limit cycle oscillations at the edges of the

"slot." It is anticipated, however, that these instability problems can and will be solved in the manner suggested here.

This partial assist type of therapy allows more patient directed movements to be accomplished. In addition, there is the potential for introducing adaptive algorithms. Such controllers are currently a topic of research with MIT-MANUS. A "slot" is defined between the equilibrium point (defined by the minimum-jerk trajectory) and the target, much like the rectangle in Fig. 7-9(b). Parameters like the stiffness of the walls and the geometry of the slot can be adjusted in response to patient performance. Implementing analogous controllers with the wrist device is something that could be done in the future.

## 7.3 Conclusions

The video games included with the robot emulate typical therapeutic tasks. The visual display, though primitive, effectively conveys the orientation of the robot on-screen and records this data for subsequent analysis. Improvements and increased sophistication of this display is only one of a number of goals for this device. Future development of virtual environments with the robot can allow a number of functional tasks to be programmed for therapy. It is hoped that, through pilot studies, a better understanding of the best ways to use the device will be gained. Parameters in the games concerning the amount of robot-assist and movement timing are of particular concern. It is also important how, in general, the patients respond to the device. Effective therapy relies on a comfortable workstation and robot feel and video exercises that can retain patient interest.

# Chapter 8

# Conclusions

The work presented in this thesis describes a step in the development of a robotic wrist rehabilitator. The first step, as described in Williams [54], details a design for the robot. Here, the robot is assembled and the design is reviewed and characterized. In addition, a controller and basis for therapy with the robot are developed. This chapter reviews the major accomplishments of this research and discusses what the next steps for this project should be.

## 8.1 Current State of the Project

### 8.1.1 Goals Accomplished

The major accomplishment of this work has been the realization of hardware for the robot from its initial design. The device is found to be most useful in movements of pure abduction/adduction, pure flexion/extension, and pure pronation/supination. Hard nonlinearities impede the development of controllers that can provide smooth and stable operation. The complexity of the control problem encountered here could be reduced through proper decision making at the design level. Revisiting and addressing the research objectives as presented in the first chapter:

- Basic functionality of the wrist robot was achieved according to the necessary modifications described in Chapter 3 and Appendix C. The details of the as-

sembly, especially of the fragile motor-encoder package, proved to be the main obstacle to this goal.

- Through the analysis of the design, a number of areas of focus for redesign were identified and addressed throughout Chapter 3 and Appendix C. These include reassessing the mechanism kinematics, redefining the functional requirements to address patient sizing/strength concerns, analyzing the gear loading on the shafts to avoid the excessive deflections seen in the current design, and emphasizing higher quality components. Where possible, solutions were suggested for the identified design issues, though the responsibility for those decisions ultimately lies with the designers.

- Component characterization showed the amplifiers and actuators to operate reliably. The main concern with the actuator performance is cogging.

- The parameter identification and system analysis of Chapter 5 aids in the understanding of device operation. The modeling and simulation carried out here was sufficient to encapsulate qualitative behavior.

- Closed loop control was successfully implemented on the device. Considering the patient-robot interaction, it seemed appropriate to focus on controlling the stiffness and damping of the actuators as a means of providing a given endpoint impedance. The framework for an impedance controller was introduced along with schemes for gravity, friction, and backlash compensation. In practice, only the gravity compensation was implemented successfully to complement the PD controller.

- The performance limits of the device under the current control scheme were mapped out. These impedances may suffice for therapy, a question that will be answered through clinical study, but the device itself is under-performing. In order to improve the achievable impedances with the current device, the control problem will need to be reassessed.

- Interactive video games using a simple graphics display were developed to emulate the common therapeutic exercises of strength training, resistance training, and sensorimotor training. The robot has the ability to record data for patient evaluation and analysis.

- The remainder of this chapter outlines suggestions for further work/research in terms of design, control, and device implementation, much of which has been introduced in this thesis.

### Clinical Trial Readiness

The robot as described within this thesis is currently installed at the Burke Rehabilitation Hospital in White Plains, New York, set to go through the early stages of clinical trials. Redesigned versions of the device based on this work and created at IMT are expected to come on-line soon as well. As mentioned above, the device has been outfitted with a full complement of video games to provide sensorimotor, strength, and resistance training. Part of the pilot study should include an evaluation of what gains and what games work well for therapy.

### Safety Features

Safety being paramount in any human-machine interface, it is useful to recall the following robot features:

- Mechanical limit stops prevent over-rotation about any of the robot axes. This nearly[1] guarantees that the robot will not interfere with itself during operation.

- Software limits shut down the actuators if the handle over-rotates[2] during a game.

- A PLC monitors the status of each servo-amplifier and shuts down the entire system in the event of a fault detected in any one of them.

[1] Contact between the linear slide rail and transmission housing cover remains possible, though unlikely during a therapy session.

[2] These limits are set slightly below the mechanical limits.

- Where possible, interfaces between the patient and the robot are cushioned, using Velfoam® and rubber stops.
- Commands at the beginning and end of each game are ramped up to their desired values in order to eliminate the possibility of a large discontinuous torque applied to the patient.
- In the event of either ADR or ADL actuator saturation, the commands to the DIFF actuators are scaled so as to preserve the intended force orientation.
- Three emergency stop buttons are provided: one is located on the front of the electrical panel, the other two, attached to the panel by $\sim$ 10 ft cables, can be positioned where convenient.
- Any program may be terminated through a keystroke.

### Device Limitations

While the robot has achieved functionality and is set to begin clinical trials, it is important to recognize the limitations of the device. The following list summarizes the issues that have not been satisfactorily addressed by this research. Some of these issues likely cannot be addressed within the current design; other issues have simply been deferred due to factors such as the time and cost required compared to the benefit.

- Patient positioning is critical for operation. The nature of the mechanism for wrist rotation requires that the flexion/extension axis of the wrist coincide with the flexion/extension axis of the robot. Furthermore, the hand must be securely attached to the handle. These restrictions on patient position emphasize the importance of the therapist in overseeing the robot therapy.
- The robot ranges of motion are limited: the range of motion in pure abduction is reduced due to the mechanical limit stop, PS motions are limited by interference with the human forearm, and circumduction movements are difficult as discussed in section 3.5.

- The controller design has not successfully accounted for backlash or motor cogging. Acceptable operation is achieved by limiting the gains and, therefore, the performance capabilities of the device.

- There is some unresolved flickering of the cursor during the robot games. The code for this should be addressed.

- Structural instabilities remain present in the DIFF axis, resulting in low amplitude vibration of the handle during therapy.

- The current design is not amenable to maintenance, as accessing most of the components requires partial or complete disassembly of the device.

## 8.2 Future Work

First and foremost, the work presented in this thesis should be reviewed independently by members of the research/project group. This is essential for the sake of the long term success of the project, as allowing errors to propagate will only slow the process once they are discovered.

### Technical Aspects

- The major the engineering effort should focus on the device limitations summarized above. With the redesign effort well underway, many of these known problems, especially those that depend on component quality, should be addressed. Once fully designed and constructed, the control problem can be reconsidered so that it is specific to the new hardware.

- There is also an opportunity to use the device as a test-bed for advanced controllers; this would constitute a case study in controller design for a system with built-in nonlinearities. This was the approach taken in Chapters 5 and 6, during which the existing hardware was taken to be a constraint. Clearly, there is room for improvement over the work presented in Chapter 6.

- Chapter 5 consisted mainly of identifying the impedance of the robot. A general method of robot impedance calibration would be useful for this and other similar applications. Such a procedure would consist of sensor calibration, actuator/drivetrain calibration, static and dynamic impedance characterization, and coupled and uncoupled stability characterization. This could potentially involve a multi degree-of-freedom machine of known characteristics to automatically perform the identification. Even the most general solution will likely require some device-specific attention to detail as in, for example, fixturing, but the concept could prove useful.

### Redesign Efforts

Chapter 3 and Appendix C go into some detail over the design issues that should be addressed in the next version of this robot. This redesign has been conducted concurrently with the deployment of the prototype. Beyond the basic reproduction/redesign project, there is the potential to augment the current system operation. Ultimately, it is desirable that the wrist device be integrated with MIT-MANUS to provide 5 to six degree-of-freedom therapy (if the vertical module were also included). This presents itself as a task that will require a significant design effort on the current hardware to account for issues such as the transmission of electrical power to the actuators and the complexity of the new dynamics.

There is also a great deal of potential improvement to be made with the current visual display. It will be interesting to see how patients respond to the current visual display, which is built on the graphics primitives available in QNX. The relevance paradigm employed ("pointing at a screen") is somewhat diminished by the physical placement of the monitor at the workstation[3]. One could envision both "high-tech" and "low-tech" solutions to the visual display problem. Virtual environments rendered in three dimensions may eventually become useful in conveying spatial rotations. At the other end of the spectrum, tasks could consist of the patient reaching

[3]The monitor is positioned in the patient's line of sight rather than directly in front of the robot.

for physical objects, doing away with the visual display altogether. Such tasks would likely require the object in question to be instrumented as well, but there is some value in eliminating the abstraction of the visual display. Recall that therapy with the device is meant to promote functional capability, which is generally thought to be influenced by practicing functional tasks.

### Alternate Applications

Even the most specialized hardware finds uses in other fields. Much of the technology enjoyed by today's society finds its roots in projects for the space program. One of the more obvious potential applications for the device beyond physical therapy is as a device for psychophysical experimentation. Data collected from MIT-MANUS [45] has been used to identify motor primitives; it is anticipated that data from the wrist robot will be analyzed in the same manner. Experimentation with normal subjects performing movement tasks while the robot is operating passively could provide data for this purpose. The evolution of these submovement patterns during motor recovery can also be investigated by analyzing the data collected from stroke patients. The value lies in the device's ability to measure the spatial orientation of the wrist and forearm. Any application requiring such measurements could benefit from the wrist robot.

The wrist robot could also find a niche in the entertainment industry as a three dimensional "force feedback" joystick. Utilization of the wrist robot as a haptic device, such as for a video game or a flight simulator, is fairly analogous to the therapeutic operation of the device. To be sure, the required force levels will likely not be as high and specific movement profiles may not be such an important part of the controller, but the basic idea of emulating some environmental behavior through the actuator commands is the same. Only a few ideas for alternate applications for the wrist robot are presented here, with a complete listing limited only by the reader's own imagination. For the immediate future, work with the device will focus on exploiting its ability to administer and evaluate therapy protocols.

# Appendix A

# Three Phase Current Sensing

## A.1 Architecture

The amplifier characterization carried out in Chapter 4 made use of a custom three-phase current sensor based on plans by Foster [19] and built in conjunction with Tang [52]. Each phase, identical in construction, consists of one Burr-Brown INA117 difference amplifier and two operational amplifiers, arranged as shown in Fig. A-1. The voltage difference between a motor phase and a servo-amplifier phase drives the current, so a $0.1\,\Omega$ power resistor is placed in that line. The voltage across this resistor, $V_{in}$, serves as the input to the difference amplifier stage so that, by Ohm's law,

$$V_{in} = V_{motor} - V_{servo} = IR_s \tag{A.1}$$

where $I$ is the current to be measured and $R_s$ is the power resistor[1].

The low pass filter stage is a unity gain, two-pole Butterworth filter implemented with the op-amp and network of resistors and capacitors. Its transfer function can be shown to be

$$\frac{V_{filt}}{V_{in}} = \frac{1}{R_1 R_2 C_1 C_2 s^2 + (R_1 + R_2) C_1 s + 1} \tag{A.2}$$

where $V_{filt}$ is the output of the filter stage, which is also the input to the gain stage.

[1] While this value is nominally $0.1\,\Omega$, the actual resistance across the terminals for each phase varies slightly.

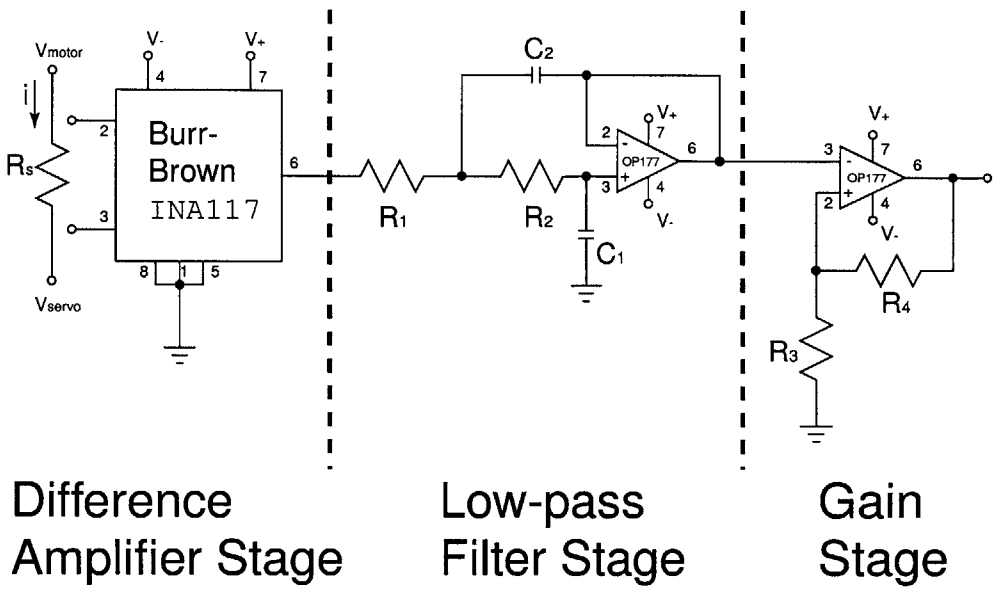


Figure A-1: Current sensor electrical schematic [52].

The gain stage transfer function is given simply by

$$\frac{V_{out}}{V_{filt}} = \left(1 + \frac{R_4}{R_3}\right) \tag{A.3}$$

with $V_{out}$ measured by the oscilloscope or A/D board, depending on the test. This gives the overall transfer function as

$$\frac{V_{out}}{I} = R_s \frac{\left(1 + \frac{R_4}{R_3}\right)}{R_1 R_2 C_1 C_2 s^2 + (R_1 + R_2) C_1 s + 1} \tag{A.4}$$

with cutoff frequency given by

$$\omega_c = \sqrt{\frac{1}{R_1 R_2 C_1 C_2}} \tag{A.5}$$

Table A.1 shows the values of the components used in the current sensor, which give it a nominal cutoff frequency of 928.2 Hz.

| Component | Value |
|---|---|
| $R_1$ | 19.6 kΩ |
| $R_2$ | 20.0 kΩ |
| $R_3$ | 4.99 kΩ |
| $R_4$ | 15.0 kΩ |
| $C_1$ | 5 nF |
| $C_2$ | 15 nF |

Table A.1: Values of current sensor components.

## A.2 Characterization

Experiments with the current sensor were conducted in discrete and continuous time to verify the model given above. The static response of each phase was determined by inputting a known current from a BK Precision power supply and measuring the output with a Fluke digital multi-meter. Nominally, the DC gain for each stage should be 0.4, seen by plugging the values from Table A.1 into the limit of Eq. A.4 as $s$ approaches 0. Differences between this value and the actual gains, listed in Table A.2, are due to component tolerances and increased resistance at the terminals.

| Phase | Sensor Gain $[\frac{V}{A}]$ |
|---|---|
| A | 0.461 |
| B | 0.438 |
| C | 0.433 |

Table A.2: Current sensor gains.

Frequency response testing was conducted using the oscilloscope and a Leader LG1031 function generator. Figures A-2, A-3, and A-4 show that the current sensor frequency response closely matches the theoretical. In these figures, the solid line is the model, while the circles represent the data points. The magnitude is a plot of the circuit output voltage divided by the DC circuit output voltage in decibels.

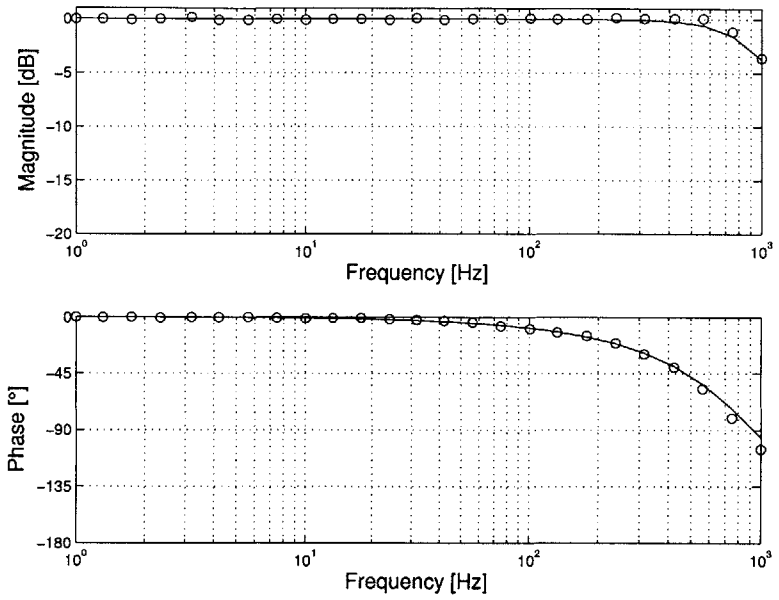


Figure A-2: Phase A current sensor frequency response in continuous time.

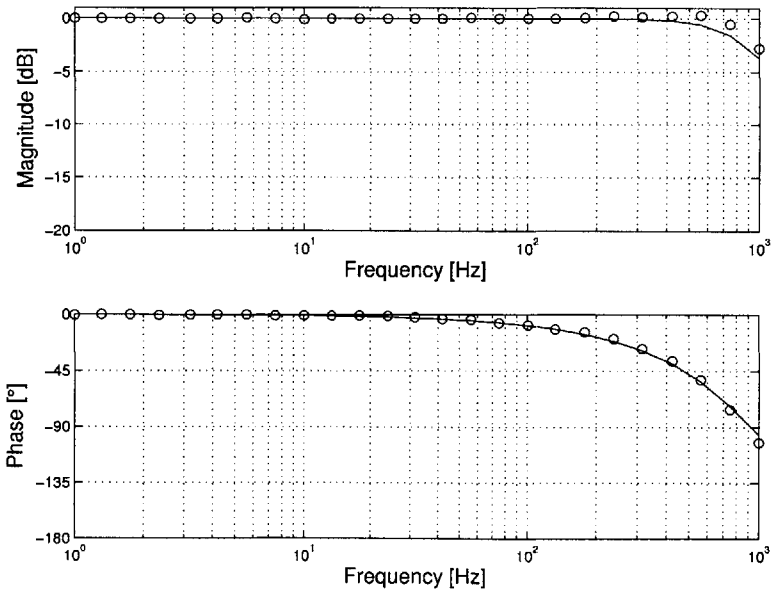


Figure A-3: Phase B current sensor frequency response in continuous time.

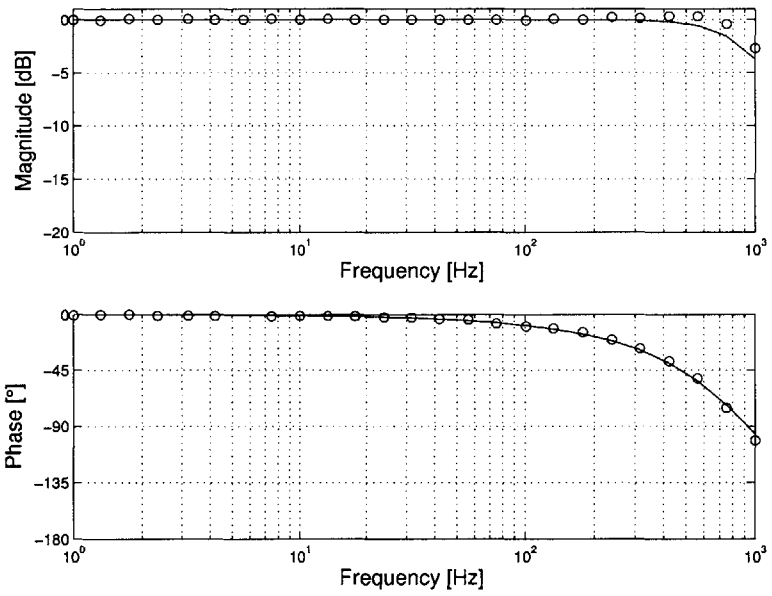


Figure A-4: Phase C current sensor frequency response in continuous time.

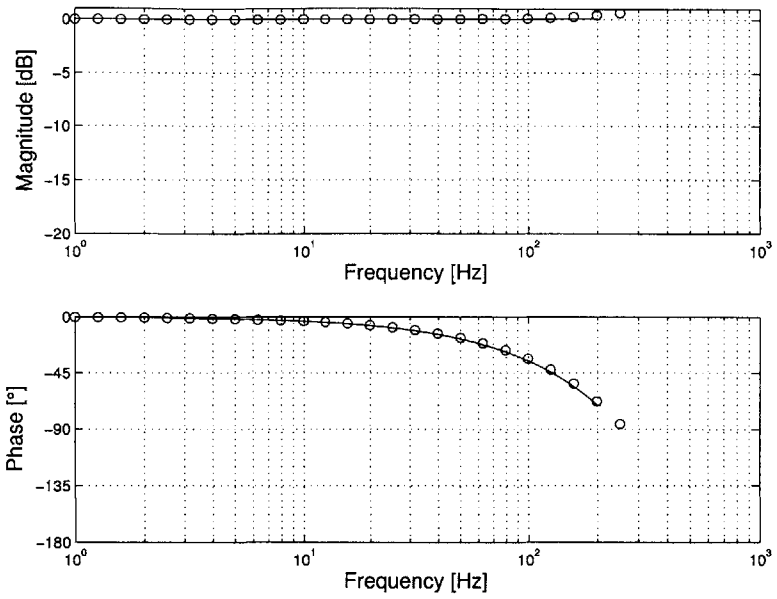


Figure A-5: Phase A current sensor frequency response in discrete time.

Frequency response testing was also conducted using the computer, sampling at 1 kHz. Both the Bode plots and linear phase versus frequency plots are included here. Figures A-5 through A-10 show these results, whose 1 ms delay is attributable to sampling, since the effects of the output are not recorded until the next time step.

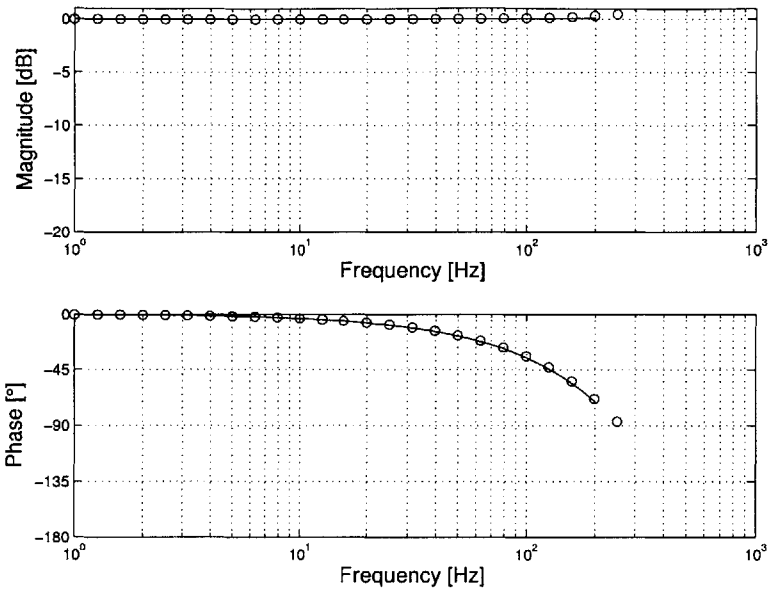


Figure A-6: Phase B current sensor frequency response in discrete time.

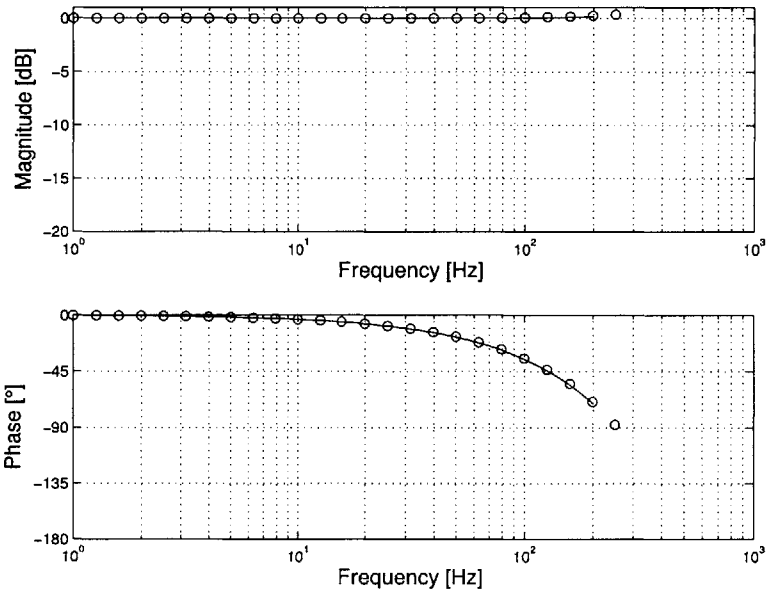


Figure A-7: Phase C current sensor frequency response in discrete time.

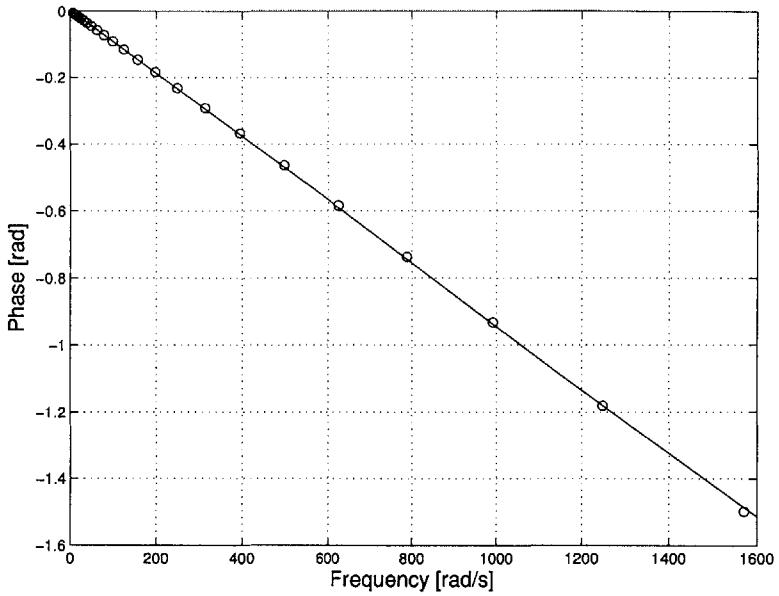


Figure A-8: Phase A current sensor linear phase versus frequency in discrete time, delay = 0.95 ms.

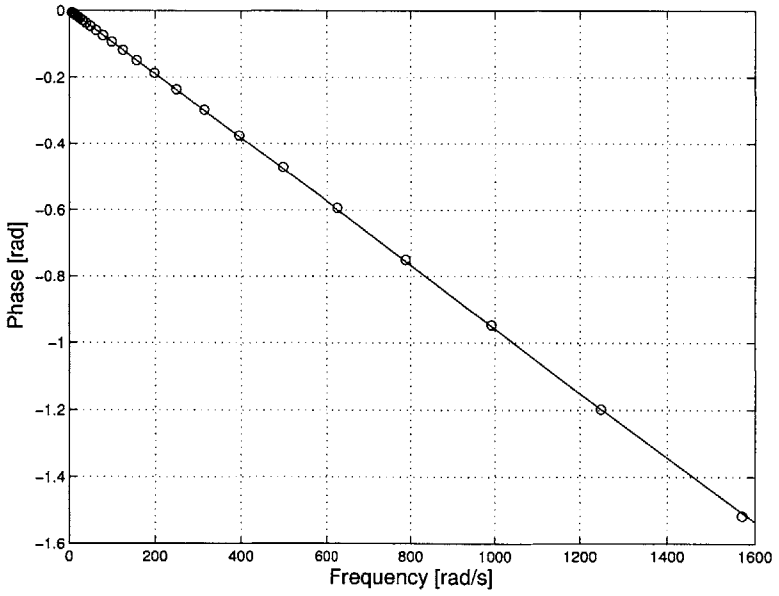


Figure A-9: Phase B current sensor linear phase versus frequency in discrete time, delay = 0.96 ms.

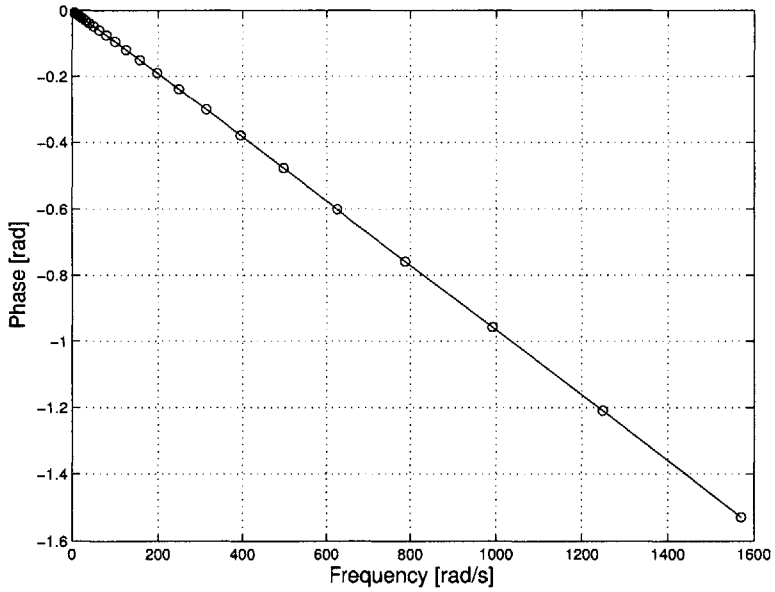


Figure A-10: Phase C current sensor linear phase versus frequency in discrete time, delay = 0.97 ms.

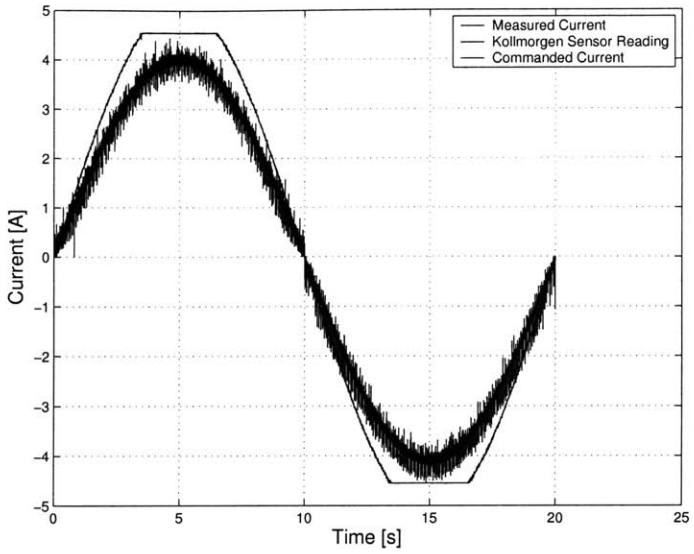


Figure A-11: The command current is obscured by the measured current, which is the noisier of the signals. The curve that saturates is the Kollmorgen current sensor data.

Kollmorgen servo-amplifiers come equipped with their own configurable-gain[2] current monitor. Kollmorgen literature advises against using this current monitor in a control loop. The current was recorded during servo-amp and motor testing to get an idea of what it was measuring. One of these tests is shown in Fig. A.2, during which the Kollomrgen reading saturates. Figure A.2 shows the current sensor gain as a function of the rotor position. One would expect the current sensor to accurately reflect the torque ripple encountered in Chapter 4, but this is not the case. Figure A.2 compares the Kollmorgen current sensor readings to the actual current readings from the current sensor discussed above. The position dependence, accurately reflected in the actual current, is not perceptible in the Kollmorgen readings. This figure also reflects the fact that the sensor is reading around 27% above its expected value. This monitor does not behave as expected: the apparent gain is not directly proportional to ISCALE, as Kollmorgen literature would suggest, but varies in an unknown manner with this parameter. Due to the apparent inaccuracy and unreliability of this measurement, it is not recorded or used in any way with normal robot operation.

[2]The current-to-voltage transfer function here is actually the same as introduced in Eq. 4.3 which depends upon the value of ISCALE.

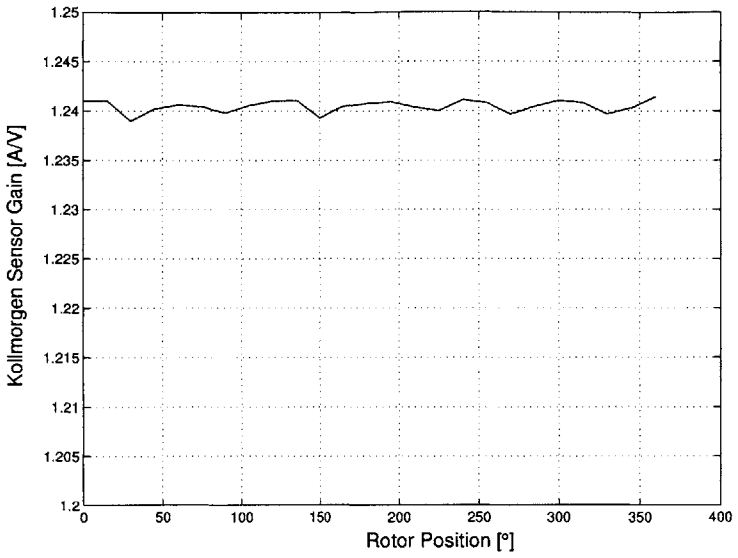


Figure A-12: Kollmorgen current sensor gain.

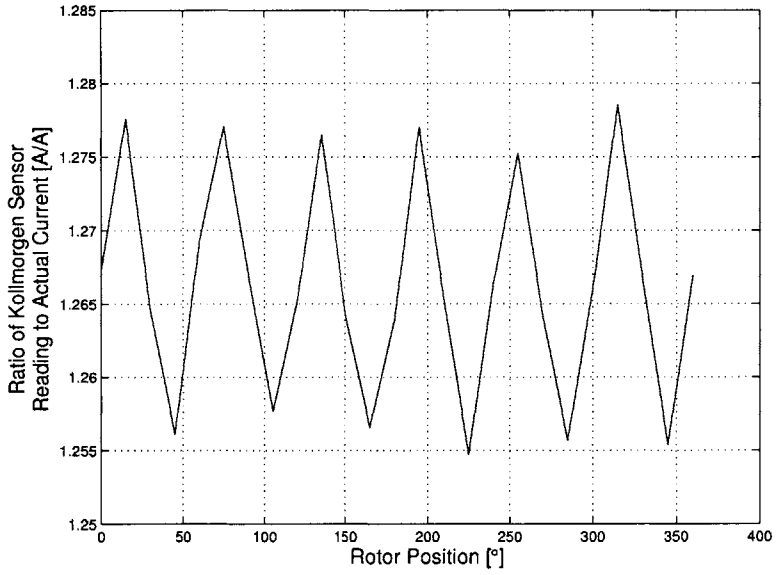


Figure A-13: Kollmorgen current sensor readings.

# Appendix B

# Derivations and Analysis

## B.1 Velocity Measurement

Velocity measurements used by the controller are computed online from position measurements. The program keeps track of values from the previous sample and implements a simple back-difference algorithm, so that

$$\omega = \frac{\Delta\theta}{T_s} \tag{B.1}$$

where $T_s$ is the sampling period and $\Delta\theta$ is the difference between the current position and the previous position. A first order Butterworth filter with a cutoff frequency of 30 Hz is also implemented to give the final velocity measurement as

$$\omega_f = 0.0864\,(\omega + \omega_p) + 0.8273\,\omega_{pf} \tag{B.2}$$

using the subscript $p$ to denote previous, $f$ to denote filtered, $pf$ to denote previous filtered, and the coefficients are for a 1 kHz sampling rate. This topic is relevant to discussion on the determination of the appropriate encoder resolution. The remainder of this section examines some of the limiting factors for the current implementation of Gurley encoders.

The first point to examine relates to the maximum resolvable speed. Let $r_{enc}$

be the encoder resolution in counts per cycle where $\Delta\theta_{min}$ is the smallest resolvable change in encoder reading, given by

$$\Delta\theta_{min} = \frac{1}{r_{enc}} \tag{B.3}$$

In this setup, $r_{enc} = 40960$, making $\Delta\theta_{min} = 0.0088\,^\circ$ of pinion rotation. The servo-amplifier has a maximum input frequency of 3 MHz, which could limit the maximum resolvable speed. Examining the other components, however, shows that the US-Digital counter card can read a maximum rate of 1.75 MHz. This card has its own on-board, configurable low-pass filter whose cutoff frequency can be set to an integer divider of the maximum rate. This divider is currently set to 3 giving a maximum input frequency of 583 kHz. This still does not represent a limiting factor for the system. The encoder itself is reported to have a maximum output frequency of 500 kHz. The maximum speed, therefore is 12.2 rps. Taking into account the gear ratios involved, this amounts to some $420\,\frac{^\circ}{s}$ in the PS axis and $540\,\frac{^\circ}{s}$ in the DIFF axes. It is expected that these speeds would not be approached during normal stroke therapy, during which slow motions are executed, often over the full ROM.

The other point of view for determining encoder resolution requirements is on the low-end. It is not very useful to determine the encoder resolution based on some endpoint position accuracy requirement. The backlash in the gears, on the order of a few degrees at the pinion, negates the advantage of being able to resolve thousandths of a degree. Even if there were no backlash, the JND for wrist and forearm motions is $2\,^\circ$ which, in terms of encoder resolution, is multiplied by the gear ratio, translating to an extra order of magnitude. Such requirements are not very stringent. Instead, it is instructive to examine the lowest resolvable velocity. By Eq. B.1, the lowest resolvable velocity is improved (lowered) by increasing the resolution and, somewhat counter-intuitively, lowering the sampling rate. The sampling rate should be kept high for the sake of the control algorithm. One way to define the encoder resolution requirement is to consider the damping gain involved. These servo-amplifiers have 14-bit resolution on their analog input, roughly 1 mV. Using this along with some desired

endpoint force resolution due to damping, it is fairly straightforward to calculate a minimum encoder resolution for this application.

## B.2 Minimum-Jerk Motion

Movement profiles for therapy in this thesis follow minimum-jerk trajectories. Such trajectories are smooth and exhibit bell-shaped velocity profiles. All minimum-jerk trajectories discussed here are of a single variable and have homogeneous endpoint conditions. The parameters of the move are $\Theta_m$, the move distance, and $t_m$, the move time. The minimum jerk trajectory is found by minimizing the cost function

$$C_J = \frac{1}{2}\int_0^{t_m} \left(\frac{d^3\theta(t)}{dt^3}\right)^2 dt \tag{B.4}$$

where $\theta(t)$ is the position as a function of time, $t$. Using the Euler-Poisson equation from variational calculus, the extrema on the interval $0 < t < t_m$ of such a functional are found to satisfy

$$\frac{\partial C_J}{\partial \theta} - \frac{d}{dt}\frac{\partial C_J}{\partial \dot{\theta}} + \frac{d^2}{dt^2}\frac{\partial C_J}{\partial \ddot{\theta}} + \ldots (-1)^n \frac{d^n}{dt^n}\frac{\partial C_J}{\partial \theta^{(n)}} = 0 \tag{B.5}$$

which reduces to

$$\frac{d^3}{dt^3}\left(\frac{d^3\theta}{dt^3}\right) = 0 \tag{B.6}$$

The solution to the optimization problem is a fifth order polynomial

$$\theta(t) = C_0 + C_1\, t + C_2\, t^2 + C_3\, t^4 + C_4\, t^5 \tag{B.7}$$

subjected to the boundary conditions

$$\begin{aligned} \theta(0) = 0 \quad &, \quad \dot{\theta}(0) = 0 \quad , \quad \ddot{\theta}(0) = 0 \\ \theta(t_m) = \Theta_m \quad &, \quad \dot{\theta}(t_m) = 0 \quad , \quad \ddot{\theta}(t_m) = 0 \end{aligned} \tag{B.8}$$

assuming the move is from position 0 to $\Theta_m$. Working out the solution provides the final result as a function of normalized time, $\tilde{t}$, for the movement profile.

$$\theta(\tilde{t}) = \Theta_m \left(10\,\tilde{t}^3 - 15\,\tilde{t}^4 + 6\,\tilde{t}^5\right) \tag{B.9a}$$

$$\dot{\theta}(\tilde{t}) = \frac{\Theta_m}{t_m} \left(30\,\tilde{t}^2 - 60\,\tilde{t}^3 + 30\,\tilde{t}^4\right) \tag{B.9b}$$

## B.3 Numerical Methods

The majority of computations and data analysis carried out within this thesis have been with MATLAB. MATLAB has become a standard tool in engineering and is especially notable for its ability to easily handle matrix operations. MATLAB also contains a number of functions that, when used properly, can assist the user in performing data analysis. The `ode`-family of solvers, for example, provide solutions to state-space representations of a system of differential equations. This section introduces the main functions used for curve fitting in this work.

### Least-Squares

Least squares curve fitting is simple yet powerful method for finding the best fit line to a given set of data. The data (or processed data) is assumed to have the form

$$y_i = mx_i + b \tag{B.10}$$

where $m$ is the slope and $b$ is the intercept of the best fit line for the data set, $x_i$ and independent variable set, and $y_i$ is the predicted value of each dependent variable. The goal of the method is to minimize the sum-of-squares of the error, $S$, with the individual errors $e_i$ given by

$$e_i = Y_i - y_i \tag{B.11}$$

where $Y_i$ is the measured data set.

$$S = \sum_{i=1}^{N} e_i^2 \tag{B.12}$$

is then minimized by setting the partial derivatives with respect to the slope and the intercept equal to zero.

$$\frac{\partial S}{\partial m} = 0 = \sum_{i=1}^{N} 2\left(Y_i - mx_i - b\right)\left(-x_i\right) \tag{B.13a}$$

$$\frac{\partial S}{\partial b} = 0 = \sum_{i=1}^{N} 2\left(Y_i - mx_i - b\right)(-1) \tag{B.13b}$$

which can be solved for the fit parameters as

$$b = \frac{\frac{\sum x_i Y_i \sum x_i}{\sum x_i^2} - \sum Y_i}{\left(\sum x_i\right)^2 - N} \tag{B.14a}$$

$$m = \frac{\sum Y_i - bN}{\sum x_i} \tag{B.14b}$$

### MATLAB's `fminsearch`

Much of the curve fitting presented in this thesis has utilized MATLAB's `fminsearch` function, an unconstrained nonlinear optimization solver. If the functional form of some data set is known, it can be used to define some error function of the parameters of interest which become the variables of the search. A simplex search method is employed to find the best-fit solution. This type of optimization routine can be thought of geometrically in $\mathbb{R}^{\mathbf{n}}$ space, where $\mathbf{n}$ is the number of dimensions and equal to the number of variables being optimized. The algorithm evaluates the function at $\mathbf{n} + 1$ points so that it is able to determine the direction of improvement for the variables [60]. Control variables are adjusted, searching the solution space for the optimum solution as the least favorable conditions are rejected. Since it only utilizes function evaluations as opposed to function derivatives, `fminsearch` can be

very robust. Simplex search techniques, however, are both inefficient and subject to finding local minima of the specified function, so care must be taken in choosing the initial conditions.

# Appendix C

# Version 0 Design Notes

With any alpha prototype some details are inevitably overlooked. Just as errors in the analyses presented in this thesis will be uncovered, there were a number of ideas presented in the design of the wrist robot that required more thought. It is instructive to review the cons as well as the pros of the design, both as an exercise of the design process and as a matter of engineering curiosity. This appendix, an extension of Chapter 3, attempts to enumerate the known design issues and comment on their tractability within the framework of the current design, largely serving as a guide for future redesign efforts[1]. Part naming conventions generally correspond to those given in Ref. [54] and there are numerous cross-references to the body of this thesis in an attempt to minimize redundant presentation of information.

## C.1 General Comments

An obvious thrust of this design has been economy of size. The compactness of the hardware, however, creates many difficult assembly problems. Difficulties in assembly directly translate into difficulties in maintenance. Since the machine components used will have varying lifetimes, it would be advantageous be able to service the device. If, for example, the interior (ADR or ADL) encoders on this device were to fail for any

[1]This information has already been presented to those in charge of the redesign effort, but is reproduced here for completeness.

reason, the device would be rendered effectively useless; replacing these components involves a complete disassembly of the device.

A major recommendation here is that a motor-encoder package be sought out for the redesign rather than separate pieces. Issues like encoder errors due to excess loading (section 3.3) were due to the fragility of the connection between motor and encoder and difficulties in mounting. In addition, the front-mounted encoders within the transmission housing are a major contributor to the difficulties encountered in assembly. Figure C-1 shows the location of the encoders. Access to these encoders is limited to the slots in the housing, making the assembly nearly blind. The set screws of the encoder must be tightened onto the flats of the motor shafts through this slot.

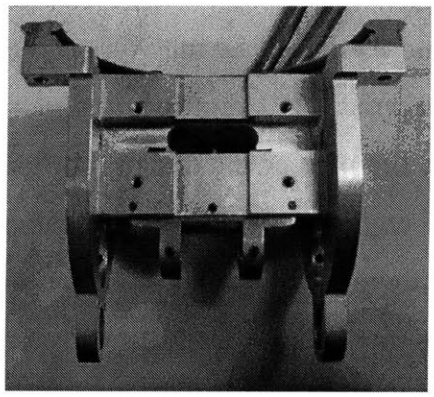

Figure C-1: Differential transmission housing with modified opening for encoders.

One recurring problem throughout the assembly of this device has been locating the motors with respect to the device. All of the motors are attached to their respective housings using four machine screws. Motors are located by the counterbores where the heads of these machine screws sit. Due to the inherent play in such a connection, it is difficult to say with any degree of accuracy the exact location of the motor axes. Along these lines, some of these thru-holes are partially obscured. Consider the DIFF assembly, where the compound gear blocks the holes. Low-profile bolts were used, inserted before the gears, to accommodate this situation. These motors must be drawn in a thread at a time so that the motor faces are flush against the transmission housing (ensuring proper axis orientation). This process is made more

difficult by the need to simultaneously attach the encoders, which are floating in the transmission housing.

In general, very little attention was given to cable routing in this design. Three cables come from each motor-encoder set to the electrical panel (Halls, motor power, and encoders) and they are all fairly heavy and stiff. The cables from the ADL and ADR motors adversely affect motion in the PS axis. Looping the cables toward the back of the mechanism, as discussed in section 3.5, has minimized this problem, though it remains aesthetically unpleasant, interferes with the workstation, and leaves the encoder wires prone to accident. The cables provided by Baker Electronics are of varying lengths and are exceedingly bulky, highlighting the issue. Cabling must be considered earlier in the design process, especially with the ADR and ADL motors, along with their associated wires, moving in space.

A final critical, yet overlooked, detail has been a method for mounting the robot to the workstation. The PS motor is currently located with respect to the roller bearing mount by four counter-bored bolt holes, allowing a substantial amount of play in its placement. This play is undesirable because the motor location determines the center-to-center distance of the PS pinion and ring gear. This, combined with the fact that the motor floats in the PS motor housing, caused problems during assembly. In order to make the gears mesh properly, the PS housing had to be shimmed up with respect to the roller bearing mount. This was accomplished by mounting both pieces to a stepped piece (the step was machined to be 0.037 in.) manufactured from a U-shaped piece of aluminum stock. This piece serves the additional purpose of raising the robot high enough so that it does not interfere with the table surface during normal operation. The roller bearing block was secured using bolts coming through the underside of the table mount. There was limited clearance for the front two thru-holes (due to the bearing set) and no access to the back two holes.

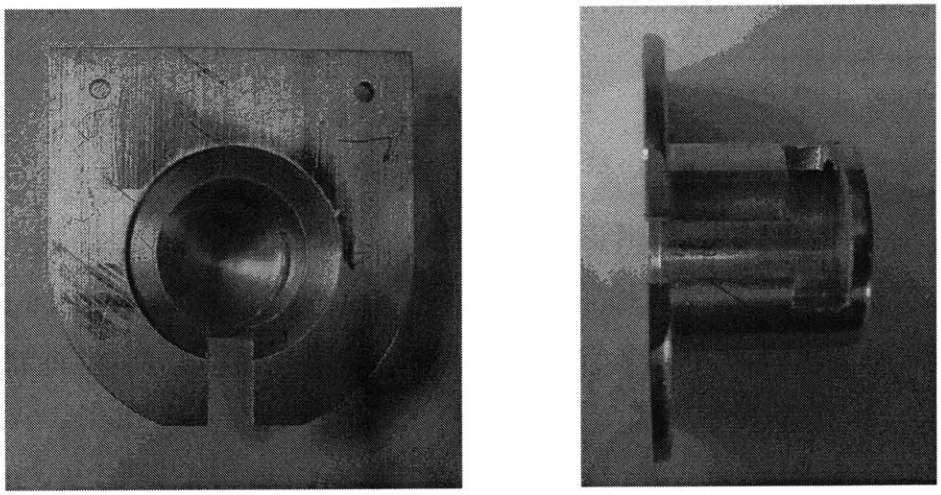

(a) Back view.

(b) Bottom view.

Figure C-2: PS encoder cover: These photos show views of the channel milled into the encoder cover to allow for cable routing.

## C.2 Dimensioning

The following lists cover inconsistencies between the listed dimensions in the final drawings from [54] and the modifications necessary for assembly and operation. These issues are grouped loosely by the portion of the robot they affect.

### Encoders

- The space for the encoders in the transmission housing was opened up to allow space for the cables without loading the encoders.

- The method for mounting the DIFF encoder was modified as described in section 3.3.

- Figures C-2 show the encoder cover for the PS axis, a CNC'd aluminum piece meant to protect the encoder. A channel was milled into this piece to accommodate the encoder cables.

### DIFF Transmission

- The transmission housing covering, a rapidly prototyped piece, was sized incorrectly so that the spider gear interfered with it during normal operation. This piece was machined in-house to allow clearance for both the spider gear and the encoder wires.

- The transmission housing was machined to allow extra support against bending as described in section 3.4.2.

- The center axis mount was machined to allow for pin removal. This involved the removal of material between the two blind holes where the mount lines up with the transmission housing.

- The compound gears are attached to their shaft with set screws instead of the prescribed pins. Pinning the gears in place could have caused damage to the robot while making disassembly problematic. The set screws should be sufficient (though they do introduce a (negligible) anisotropy in the inertia of the gear) since the gears do not encounter any axial load (they are spur gears) and rotation of the gear relative to the shaft is irrelevant (it is an intermediate gear).

- The heat sinks designed for the ADR and ADL motors were deemed unnecessary and are not presently being used. If they are included in the future, a method of attachment will need to be proposed.

### PS Axis

- Only one pinion/curved rack set is used on the PS axis; the reasoning has been covered in section 3.4.2.

- No access holes were provided for the bottom two thru-holes for the motor. These holes were drilled into the current prototype.

- The ring gears interfere with the patient's forearm, restricting movement. Rubber stops have been introduced to avoid injury, though this component must be resized to account for offset between the patient and robot axes and to consider the actual connection point[2].

- The distal forearm connection restricts patient movement. This component was replaced by a Velcro strap, discussed in section 3.5. If redesigned with regard to the relevant kinematics and sizing, it may prove useful in future designs.

- The forearm support is too small for the entire intended patient population. A support that flared out was introduced as a solution for the current hardware, though this new piece is constrained to fit in with the current ring gear setup.

**Handle**

- One of the handle degrees of freedom, as discussed in section 3.5, has been immobilized.

- The handle has been replaced by a non-handed model also covered in section 3.5.

- The press fit in one of the dowels of the slider yoke failed. The current version was repaired using adhesive, but for the future, the dimensions used for the press fit should be reviewed.

- The bevelled head of the dowel pin wedges into the slider connector. This head could be filed down to remove the interference and allow the designed stops to fulfill their purpose, though nothing has been done to the current robot.

## C.3 Performance

Some of the issues encountered with the robot bridged the gap between operation and performance. Evaluation of the torque and power producing capabilities will be

[2]The initial design was based on the wrist diameter rather than the forearm diameter.

deferred until more experience with the device in operation with subjects is obtained. Other issues relating to patient mobility have been covered in the body of this thesis. The remainder of this appendix covers some of the other issues that warrant a re-introduction.

The structural instabilities encountered were due to shaft deflection under loading from gear tooth interactions. Problems here were first noticed in the DIFF axis, as its shaft visibly moved during static endpoint force testing. Difficulties arose in the PS axis when the second pinion gear was introduced. These types of problems can be prevented in the future by including basic analysis of expected loading conditions and the how the loading affects the structure bearing the load.

The premise behind the introduction of the eccentric bearings is erroneous. The two major problems caused by their existence are with assembly (the high probability of ending up with skewed shafts) and their intended purpose (backlash adjustment). Adjustment of the center-to-center distance between the pinion and intermediate stage cannot be made without inadvertently adjusting the center-to-center distance between the intermediate stage and the differential gear stage (whose location is fixed). Future designs should not include this feature. The motor shaft, intermediate shaft, and differential shaft locations should all be determined using the pitch diameters of the gears in question. Even a best-case scenario assembly will result in unavoidable backlash in the DIFF gear train, adversely affecting the performance capabilities of the robot.

The gear quality of the ADL and ADR motor pinions is extremely poor; the teeth are warped in the regions where holes are drilled (for the set screws and pins). This adversely affects performance. Higher quality gears should be used. It may also be possible to use a different method of attachment (other than pins) to avoid the problems caused by the presence of the holes. Two possibilities include using hubbed gears where the thru-hole is on the hub and pinning the gear parallel to the shaft axis. In addition, no method of gear lubrication has been proposed. Since this is an open gearing system, options are limited to dry lubricants, like graphite, or applied coatings, like Teflon.

# Appendix D

# Guide to the Wrist Robot

This appendix contains a copy of the supplement provided to the therapist responsible for operating the wrist robot. The information is current as of the printing of this thesis and supersedes all previous editions.

## D.1 Getting Started

### D.1.1 Powering Up

- Turn on the computer. The computer will automatically boot into QNX.
- Supply power to the robot by turning the red knob located on the upper right-hand corner of the electrical panel to the `ON` position. The green light indicating `POWER ON` will light.
- Disable the dynamic braking by pressing the red `RESET` button on the front of the panel.
- Enable the robot by pressing the green `START` button on the front of the panel.

#### Shutting Down

Powering down is accomplished using the red `STOP` button on the front panel followed by turning the knob to the `OFF` position. Never shut down the computer before

powering the robot down.

### D.1.2 Navigating the Directories

All programs are run on the QNX operating system within the X11 XWindows environment.

⟨Details on logging in and directory structure omitted for security reasons.⟩

### D.1.3 Indexing the Robot

In order to respond to the control laws properly, the robot must be indexed. Indexing is accomplished by executing the `index_position` program. When run, this program asks that the index points be passed through in a prescribed manner[1]. The user should move the handle from a position corresponding to the NW (starting at the stops) target to the center for the differential and from the left of center to the center for PS (starting from a supine position with the right hand). After indexing, a key should be pressed and the handle should be placed in its cradle. The program will (after another keystroke) display the location of the cursor. The cursor should appear at the center target with the PS indicator line vertical. If this is not the case, the robot should be re-indexed. Also, if either the line or the cursor itself are red while in the cradle, the robot should be re-indexed. The robot should not need to be re-indexed after that unless there is a power interruption to either the electrical panel or computer.

### D.1.4 Patient Attachment

Proper patient positioning is critical to the operation of the robot. The wrist axis for flexion/extension should be collinear with the flexion/extension axis of the differential. The blue, neoprene marker serves as a reference point to line up with. The wrist is secured to the robot using a Velcro strap. The patient's grip must also be secured

[1]These instructions are also displayed on-screen by the the program.

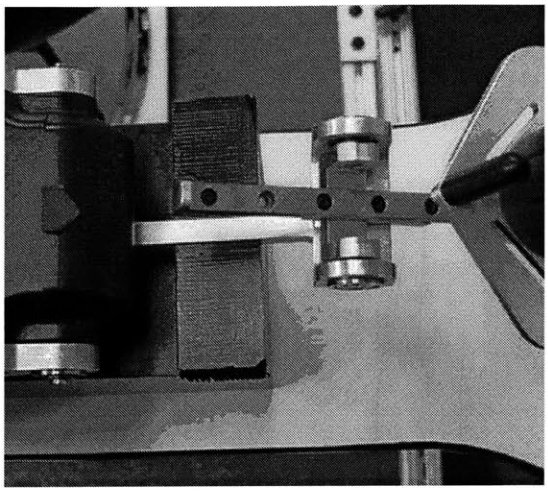

Figure D-1: Robot reference points.

to the handle; this attachment is critical for meaningful radial/ulnar deviation robot therapy. Loopholes for Velcro straps are provided for this purpose. The patient is also secured to the workstation via a bicep constraint. Therapists have recommended that the patient be situated at the robot so that the shoulder is extended forward 30° and abducted 20°. The chair and bicep support should be positioned to approach these rules of thumb, though patient comfort should always be the guiding factor. Note that the patient position defines the range of pronation and supination available.

Individual patient size could prove important in the eventual analysis of robot data. Figures D-2 and D-3 show some typical measurements that are taken of the wrist and forearm. It is recommended that, at the very least, measurements **H**, **B**, **C**, and **L** are recorded for each patient for future use. These measurements are described as follows:

**H:** distal wrist crease to handle center

**B:** wrist breadth

**C:** wrist thickness

**L:** forearm length

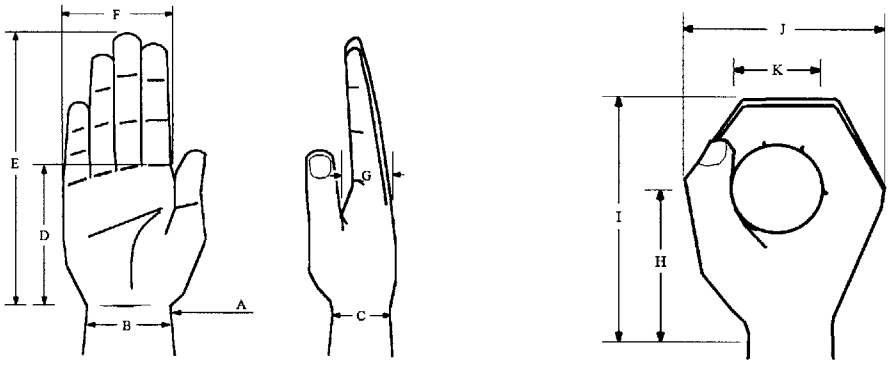


(a) Open palm.

(b) Closed palm.

Figure D-2: Typical anthropomorphic wrist measurements.

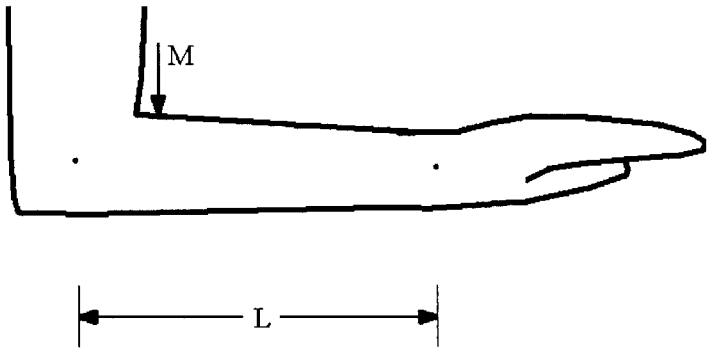


Figure D-3: Typical anthropomorphic forearm measurements.

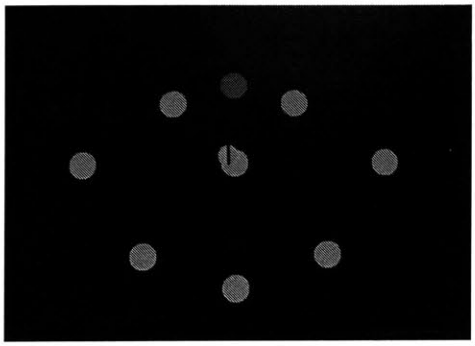

(a) Basic display in wrist joint coordinates.

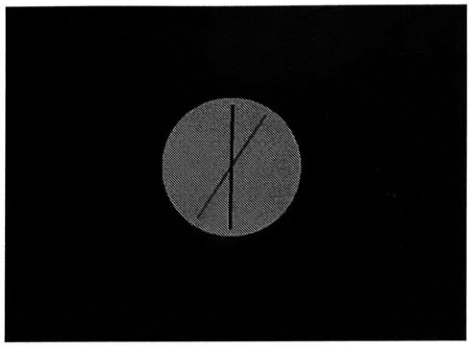

(b) Display for PS mode.

Figure D-4: Visual display types.

## D.2 Games

There are a number of games that are currently available for the wrist robot. A brief description of each of these follows. All programs[2] are executed by typing the program name along with a file prefix designating the `.dat` file(s) that will contain the results. The basic display, as alluded to in the indexing section, consists of a yellow cursor (a circle) with a black line on it. There is a one-to-one mapping between the position of the cursor on the screen and the orientation of the wrist. This representation is independent of forearm orientation, *i.e.*, radial and ulnar deviation are always displayed as up and down movements of the cursor and flexion and extension movements are always represented by side to side movements of the cursor on the screen. The line in the cursor is meant to indicate the orientation of the handle as affected by pronation and supination.

### D.2.1 Record and Playback

The executable `recording` will allow a trajectory to be recorded in the basic display. Executing `playback` after this will play this trajectory back on the robot. For safety's sake, playback should not be run if the user is unsure when the reference trajectory

[2]Not including `index_position`, `recording`, or `playback_rec`.

was recorded. `recording` stores the trajectory into a file named `ex_traj.dat`. During the recording, the robot provides assistance against gravity. `playback` can be run at any one of three preset stiffnesses and stores data into a file named `act_traj.dat`.

### D.2.2 Resistance Games

The programs `center` and `pscenter` each set up the robot as a spring with its equilibrium point at the origin. The changing targets will suggest a direction for the patient to move, as the patient will have to work against the robot to approach the targets.

### D.2.3 Star

The star game, implemented by typing `star` ⟨*file_prefix*⟩, takes the user through the eight targets of wrist rotation, making minimum-jerk movements between each target while holding the PS axis at some nominal stiffness. As in many of the games currently available, the user has the option of one of three preset "stiffness" values. Part of the development of therapy protocols will be the adjustment and specification of the best therapy environment. This game can also be used as a strength training exercise if the patient is asked to hold the handle at the center of the workspace.

### D.2.4 PS Sweep

The PS sweep game, implemented by typing `pssweep` ⟨*file_prefix*⟩, presents the patient with a line target that moves with a sinusoidal trajectory. The patient is asked to follow the trajectory. When the patient is close enough to the target, the background will change from yellow to green. Game parameters like the number of periods, the total angular excursion, and the frequency of the sweep, currently hard-coded into the program, can be adjusted as necessary in the future. This game can also be used as a strength training exercise.

### D.2.5 PS Target

The PS target games, implemented by typing `pstarget` ⟨*file_prefix*⟩, offers the same visual display as `pssweep`, only now the target stops at discrete angles and requires the patient to follow a minimum-jerk trajectory towards each one. Again, this program can also be used as a strength training game.

## D.3 Data Management

The output `.dat` file for each program consists of a table of nine variables. The recorded states correspond to the orientation of the robot handle, the velocities derived from those positions, and the torques commanded for each axis. The data that is recorded by the robot is listed and described below. Note that the data is sampled at 1 kHz.

**State 1: Flexion Angle** Robot arm flexion angle in [°], nominally equivalent to the patient flexion angle. Positive readings correspond to flexion for a right-handed patient and extension for a left-handed patient.

**State 2: Abduction Angle** Robot abduction angle in [°], distinct from patient abduction angle. The exact relationship between the degree of robot abduction and the degree of patient radial/ulnar deviation depends on the individual patient geometry. Positive values are always indicative of radial deviation, despite which hand is used.

**State 3: PS Angle** The PS orientation of the robot in [°]. While the amount of forearm rotation is roughly equivalent to the PS angle indicated by the robot, patient orientation with respect to the device must always be considered in interpreting the results. Supination is a positive reading for right-handed patients and negative for left handed patients.

**State 4: Flexion Velocity** Time rate of change of state 1 in $[\frac{°}{s}]$ computed using a filtered back-difference.

**State 5: Abduction Velocity** Time rate of change of state 2 in $[\frac{\circ}{s}]$ computed using a filtered back-difference.

**State 6: PS Velocity** Time rate of change of state 3 in $[\frac{\circ}{s}]$ computed using a filtered back-difference.

**State 7: Commanded Flexion Torque** The commanded torque about the flexion axis in [Nm] computed by scaling the voltage command according to known calibration factors. This value is nominally equal to the commanded torque about the patient flexion/extension axis.

**State 8: Commanded Abduction Torque** The commanded torque about the robot abduction/adduction axis in [Nm] computed by scaling the voltage command according to known calibration factors. This value, like state 2 is related to the corresponding patient variable through geometry.

**State 9: Commanded PS Torque** The commanded torque about the pronation/supination axis in [Nm], roughly equivalent to the commanded torque imparted to the patient in forearm rotation. It is computed by scaling the corresponding command voltage by known calibration factors.

Data files can be stored on the hard drive as necessary using standard UNIX file management commands. These files can be converted into ASCII format using the `toascii` command. The `mzip` utility on the computer allows access to the Zip 250 drive to back-up and transport data. The compression utility `tar` is also available on the system.

## D.4 Safety Features

The robot includes a number of safety features:

- Patient connection points have been outfitted with rubber and foam cushions for comfort and protection.

- A Programmable Logic Controller (PLC) monitors the health of each servo and disables all servos if any one fails.
- Mechanical limit stops prevent over-rotation by the patient in any degree of freedom and protect the robot against interference with its own structure.
- Software limits exist to cut off the commands to all actuators in the event of a detected over-rotation.
- Three emergency stop buttons are provided: one is located on the front of the electrical panel, the other two, attached to the panel by $\sim$ 10 ft cables, can be positioned where convenient.
- Any program may be cut short through a keystroke.
- All programs ramp up the command at the start of a game to prevent the robot from jerking the patient.

## D.5 Troubleshooting Guidelines

- In general, errors can be cleared by power cycling and subsequently re-indexing the robot.
- Documentation and reporting of any errors encountered during operation (along with the operating conditions during the failure) could prove useful and should be considered standard operating procedure.
- The slider rail should always be parallel to the handle arm; if this is not the case, it should be adjusted.
- Do not attempt to run the robot if it is not indexed properly. If, during operation, something adversely affects the encoders, the system will misbehave. This is fixed by re-indexing the encoders and, if necessary, power cycling the system.
- Premature termination of the `recording` and `playback_rec` games may require two keystrokes.

# Bibliography


[1] Abernathy, Bruce *et al.*, *The Biophysical Foundations of Human Movement*, Human Kinetics Publishers, Inc., Champaign, 1997.

[2] An, Kai-Nan *et al.*, *Biomechanics of the Wrist Joint*, Springer-Verlag, New York, 1991.

[3] Asada, H. and J.-J. E. Slotine, *Robot Analysis and Control*, John Wiley and Sons, New York, 1986.

[4] Atherton, D.P., *Nonlinear Control Engineering*, Van Nostrand Reinhold Company, New York, 1975.

[5] Berniker, Max, *A Biologically Motivated Paradigm for Heuristic Motor Control in Multiple Contexts*, MSME Thesis, Massachusetts Institute of Technology, September 2000.

[6] Breteler, Mary D. Klein *et al.*, *End-pont constraints in aiming movements: effects of approach angle and speed*, Biological Cybernetics, Vol. 85, 2001.

[7] Brown, Forbes T., *Engineering System Dynamics: A Unified Graph-Centered Approach*, Marcel Dekker, Inc., New York, 2001.

[8] Buerger, Stephen P., *Characterization and control of an interactive robot*, MSME Thesis, Massachusetts Institute of Technology, February 2001.

[9] Byrne, John H. and William O. Berry, *Neural Models of Plasticity: Experimental and Theoretical Approaches*, Academic Press, Inc., Boston, 1989.

[10] Carr, Janet and Roberta Shepherd, *Neurological Rehabilitation: Optimizing Motor Performance*, Butterworth-Heinemann, Boston, 1998.

[11] Cogdell, J.R., *Foundations of Electrical Engineering*, Prentice Hall, Upper Saddle River, 1990.

[12] DeLisa, Joel A. *et al.*, *Rehabilitation Medicine: Principles and Practice*, Lippincott Williams & Wilkins, New York, 1998.

[13] Dote, Yasuhiko and Sakan Kinoshita, *Brushless Servomotors: Fundamentals and Applications*, Clarendon Press, Oxford, 1990.

[14] Duncan, Pamela and Mary Beth Badke, *Stroke Rehabilitation: The Recovery of Motor Control*, Year Book Medical Publications, 1987.

[15] Dudley, Darle W., *Gear Handbook: The Design, Manufacture, and Application of Gears*, McGraw-Hill Book Company, Inc., New York, 1962.

[16] Fasse, Ernest D. and Jan F. Broenink, *A Spatial Impedance Controller for Robotic Manipulation*, IEEE Transactions on Robotics and Automation, Vol. 13, No. 4, August 1997.

[17] Feeny, B.F. and F.C. Moon, *Quenching Stick-Slip Chaos with Dither*, Journal of Sound and Vibration 237(1) 173-180, 2000.

[18] Flanagan, J. Randall and Ashwini K. Rao, *Trajectory Adaptation to a Nonlinear Visuomotor Transformation: Evidence of Motion Planning in Visually Perceived Space*, Journal of Neurophysiology, Vol. 74, No. 5, November, 1995.

[19] Foster, Craig, *A Performance Characterization of an Interactive Robot*, MSME Thesis, Massachusetts Institute of Technology, September 1999.

[20] Gelb, Arthur and Wallace E. Vander Velde, *Multiple-Input Describing Functions and Nonlinear System Design*, McGraw-Hill Book Company, New York, 1968.

[21] Granit, Ragnar, *The Basis of Motor Control: Integrating the Activity of Muscles, Alpha and Gamma Motoneurons and Their Leading Control Systems*, Academic Press, New York, 1970.

[22] Graham, Dunstan and Duane McRuer, *Analysis of Nonlinear Control Systems*, John Wiley & Sons, Inc., New York, 1971.

[23] Greshen, Glen E. *et al.*, *Post Stroke Rehabilitation Clinical Practice Guide Number 16*, U.S. Department of Health and Human Services, Maryland, May 1995.

[24] Harnefors, Lennart, *Torque-Maximizing Field Weakening-Control: Design, Analysis, and Parameter Selection*, IEEE Transactions on Industrial Electronics, Vol. 48, No. 1, February 2001.

[25] Hogan, Neville, *An Organizing Principle for a Class of Voluntary Movements*, The Journal of Neuroscience, Vol. 4 No. 11, November 1984.

[26] Hogan, Neville, *Impedance Control: An Approach to Manipulation: Part I - Theory*, Journal of Dynamic Systems, Measurement, and Control, Vol. 107, March 1985.

[27] Hogan, Neville, *Impedance Control: An Approach to Manipulation: Part II - Implementation*, Journal of Dynamic Systems, Measurement, and Control, Vol. 107, March 1985.

[28] Hogan, Neville, *Impedance Control: An Approach to Manipulation: Part III - Applications*, Journal of Dynamic Systems, Measurement, and Control, Vol. 107, March 1985.

[29] Kandel, Eric R. *et al.*, *Principles of Neural Science*, McGraw-Hill, New York, 1991.

[30] Kang, Min-Sig *et al.*, *Robuts Digital Friction Compensation*, Proc of the $36^{th}$ IEEE CDC San Diego, CA, 1997.

[31] Kapandji, I.A., *The Physiology of the Joints: Annotated diagrams of the mechanics of the human joints*, E & S Livingstone, London, 1970.

[32] Kakei, Shinji *et al.*, *Muscle and Movement Representations in the Primary Motor Cortex*, Science, Vol. 285, 1999.

[33] Karnopp, Dean C. *et al.*, *System Dynamics: A Unified Approach*, John Wiley & Sons, Inc., New York, 1990.

[34] Li, Yu-Feng, *Motion Control Subject to Nonlinearities and Flexibility: An Overview Based on Friction and Flexibility Compensation*, Technical Report, Royal Institute of Technology, KTH, Stockholm, 1999.

[35] Liang, J.W. and B.F. Feeny, *Identifying Coulomb and Viscous Friction from Free-Vibration Decrements*, Nonlinear Dynamics, Vol. 16, 1998.

[36] McMahon, Thomas A., *Muscles, Reflexes, and Locomotion*, Princeton University Press, Princeton, 1984.

[37] Michalec, George W., *Precision Gearing: Theory and Practice*, John Wiley & Sons, Inc., New York, 1966.

[38] Mossman, Philip L., *A Problem Oriented Approach to Stroke Rehabilitation*, Charles C. Thomas, Springfield, 1976.

[39] Nise, Norman S., *Control Systems Engineering*, John Wiley & Sons, New York, 1994.

[40] Norton, Robert L., *Design of Machinery: An Introduction to the Synthesis and Analysis of Mechanisms and Machines*, McGraw-Hill, New York, 1999.

[41] Novak, K.E. *et al.*, *Kinematic properties of rapid hand movements in a knob turning task*, Exp Brain Res, March 2000.

[42] Oppenheim, Alan V. *et al.*, *Discrete-Time Signal Processing*, Prentice Hall, Upper Saddle River, 1999.

[43] Popov, Egor P., *Engineering Mechanics of Solids*, Prentice Hall, Englewood Cliffs, 1990.

[44] Rao, Singiresu, *Mechanical Vibrations*, Addison-Wesley, New York, 1995.

[45] Rohrer, Brandon R., *Evolution of Movement Smoothness and Submovement Patterns in Persons with Stroke*, PhD Thesis, Massachusetts Institute of Technology, June 2002.

[46] Sawner, Kathryn and Jeanne LaVigne, *Brunnstrom's Movement Therapy in Hemiplegia: A Neurophysiological Approach*, J.B. Lippincott Company, Philadelphia, 1992.

[47] Schunid F. *et al.*, *Advances in the Biomechanics of the Hand and Wrist*, Plenum Press, New York, 1994.

[48] Scott, Stephen H., *Vision to action: new insights from a flip of the wrist*, Nature Neuroscience, Volume 4 No. 10, October 2001.

[49] Slotine, Jean-Jacques E. and Weiping Li, *Applied Nonlinear Control*, Prentice Hall, New Jersey, 1991.

[50] Southward, Steve C. *et al.*, *Robust Nonlinear Stick-Slip Friction Compensation*, Journal of Dynamic Systems, Measurement, and Control, Vol. 113, December 1991.

[51] Stanney, K., *Handbook of Virtual Environments*, Lawrence Earlbaum, Inc., Hillsdale, 2002.

[52] Tang, Philip, *Characterization of a Robot Designed for Hand Rehabilitation*, MS Thesis, Massachusetts Institute of Technology, September 2002.

[53] Tao, Gang and Frank L. Lewis, *Adaptive Control of Nonsmooth Dynamic Systems*, Springer, London, 2001.

[54] Williams, Dustin, *A Robot for Wrist Rehabilitation.* MSME Thesis, Massachusetts Institute of Technology, June 2001.

[55] Vander, Arthur J. *et al.*, *Human Physiology: The Mechanisms of Body Function*, McGraw-Hill, Inc., New York, 1994.

[56] Volpe, B. T. *et al.*, *A Novel Approach to Stroke Rehabilitation: Robot-aided Sensorimotor Stimulation*, Neurology 54:1938-1944, May 2000.

[57] Woodson, Herbert H. and James R. Melcher, *Electromechanical Dynamics*, John Wiley & Sons, New York, 1968.

[58] About Stroke — Internet Stroke Center: http://www.strokecenter.org/pat/about.htm.

[59] JAS: Products - JAS Devices: http://www.jointactivesystems.com/devices.html.

[60] Simplex Optimization Methods: http://www.grabitech.com/algorithm.htm.

[61] www.REHABEQUIPMENT.com - wrist rehabilitation equipment - multiwrist: http://www.rehabequipment.com/multiwrist.htm.



2506-50